Relativistic Electrons in Electric Discharges

Cinar, Deniz

Publication date:
2014

Document Version
Publisher's PDF, also known as Version of record

Relativistic Electrons in Electric Discharges

Ph.D. Thesis

DTU Space
National space Institute

2014

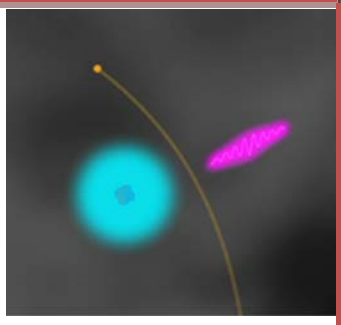

Authored by Deniz Cinar

March 2014

DTU Space
National Space Institute

Summary

Thunderstorms generate bursts of X- and Gamma radiation. When observed from spacecraft, the bursts are referred to as "Terrestrial Gamma-ray Flashes" (TGFs). They are bremsstrahlung from energetic electrons accelerated in thunderstorm electric fields. The TGFs were first observed in the 90ties at the time when also gigantic electric discharges were observed at 10-90 km altitude in the stratosphere and mesosphere, the so called "jets" and "sprites", commonly referred to as "Transient Luminous Events" (TLEs). TGFs were first thought connected to TLEs, but later research has pointed to lightning discharges as the source. The "Atmosphere-Space Interactions Monitor" (ASIM) for the International Space Station in 2016, led by DTU Space, and the French microsatellite TARANIS, also with launch in 2016, will identify with certainty the source of TGFs. In preparation for the missions, the Ph.D. project has developed a Monte Carlo module of a simulation code to model the formation of avalanches of electrons accelerated to relativistic energies, and the generation of bremsstrahlung through interactions with the neutral atmosphere. The code will be used in the analysis of data from the two space missions. We have studied the electron acceleration and photon generation in a constant electric field under a variety of conditions. These include the energy and number of seed electrons, electric field and altitude. We found that the distributions of avalanche electrons and photons are insensitive to these conditions, with exception of the electric field magnitude where the photon distribution becomes progressively more forward directed for increasing field magnitude. However, exploring photon transport to the top of the atmosphere, the angular beaming properties were found to wash out because of Compton scattering. However, we only explored the properties of the complete number of photons reaching space, not the distribution at specific locations as in the case of a satellite. With this reservation we conclude that

it is not possible to deduce much information from a satellite measurement of the photons alone on the conditions of the source region. With one exception: the spectral hardness increases with altitude of the source, again caused by reduced Compton scattering with altitude. Appling the code to a thunderstorm cloud we further found that an impulsive electric field of about 5 times the local breakdown field appears plausible for TGF generation, because it minimizes the electron avalanche time and length and the total electric potential required.

Dansk Resumé

Tordenvejr udsender pulser af X - og Gamma- stråling. Disse blev opdaget i midten af 90erne of satellitten the Compton Gamma-ray Observatory. De kaldes "Terrestrial Gamma -ray Flashes" (TGFs) og er bremsstråling fra energetiske elektroner, som accelereres i de elektriske felter skabt i tordenvejr. Omkring samtidigt opdagede man gigantiske elektriske udladninger i stratosfæren og mesosfæren i 10-90 km højde, de såkaldte "sprites" og "jets", som går under fællesbetegnelsen "Transient Luminous Events" (TLEs). TGFer blev i første omgang forbundet med TLEer, men efterfølgende forskning har peget på lynudladninger som kilde. Eksperimentet "The Atmosphere-Space Interactions Monitor" (ASIM) til Den Internationale Rumstation i 2016 , ledet af DTU Space, og den franske mikro- satellit TARANIS , også med opsendelse i 2016, vil med sikkerhed fastslå kilden til TGFer . Som forberedelse til disse missioner er der i ph.d. projektet udviklet et Monte Carlo modul til at modellere acceleration af elektroner til relativistiske energier og generering af bremsestråling gennem interaktioner med den neutrale atmosfære. Koden vil blive brugt i analysen af data fra de to rummissioner. Vi har undersøgt elektron acceleration og foton generation i et konstant elektrisk felt under en række betingelser. Disse omfatter bl.a. begyndelsesbetingelserne for elektron laviner og det elektriske felt, som driver dem. Vi fandt at energispektrene af elektroner og fotoner er ufølsomme over for begyndelsesbetingelserne, dvs. antal af kilde elektroner, deres energi og størrelsen på det elektriske felt, med undtagelse af vinkelfordelingen af fotoner, som bliver mere fremadrettede med større felt. Imidlertid, hvis man tager transport i atmosfæren med, vil fotoner, som når toppen af atmosfæren, miste deres fremadrettede karakter på grund af Compton spredning. Vi undersøgte kun vinkelfordelingen af de samlede fotoner, der når ud i rummet, ikke fordelingen i et enkelt punkt, som i tilfældet af en satellit. Med dette forbehold, konkluderer vi, at det ikke er muligt at udlede detaljeret information om kilde regionen fra

satellit målinger af foton spektret. Med én undtagelse: fotonernes energispektre bliver hårdhed for kilder højere i atmosfæren, igen som følge af reduceret Compton spredning. Koden blev anvendt på forhold i et tordenvejr, hvor vi fandt at et impulsivt elektrisk felt på omkring 5 gange det lokale elektriske "breakdown" felt forekommer plausibelt til at skabe TGFer, fordi det minimerer elektron lavine tiden og længden, og det samlede elektriske potentiale.

Preface

This thesis was prepared at DTU Space, National Space Institute at the Technical University of Denmark in fulfilment of the requirements for acquiring a PhD degree.

Supervisor : Torsten Neubert

Co – Supervisor : Olivier Chanrion

Location : DTU Space
National Space Institute
Technical University of Denmark
Elektrovej 327
DK-2800 Kgs. Lyngby
Tel: +45 45 25 97 17.
Fax: +45 45 25 95 75.

Acknowledgements

I wish to thank my supervisors, *Torsten Neubert* and *Olivier Chanrion*, for giving me this opportunity at this exciting project with nice working environment at DTU Space. I am grateful with their careful and patient guidance on my thesis, and showing the way to explore answers of new unknowns with a huge enthusiasm. I also wish to thank for their all efforts on giving a shape both in personally and my carrier.

I wish to express my gratitude to Nikolai Østgaard, Thomas Gjesteland, Ragnhild S. Hansen and Alexander B. Skeltved, who were always with me with their help and provide useful discussions on my project. I am very glad to meet and study with them. It was a big pleasure to collaborate with them through my abroad study. And, I had really enjoyable moments with them during my PhD study.

I would like to thank Brant Carlson for nice discussions on energetic electrons and bremsstrahlung process. I have gained many useful knowledge of that through my project.

I am thankful to Irfan Kuvvetli, who never hesitate to give his support that was a great motivation for me on my thesis. I also glad to have nice discussions on laboratory sparks, which extended my knowledge of it.

I am indebted Rene Forsberg, for his helps at official issues on my thesis. I very glad to know such a kind and positive person. He always managed to keep me calm on them, which I always was curious on.

Of course, some special thanks to:

Kristian Pedersen, giving his effort and support not only for me and my study but, also for all PhD candidates at the institute through their projects.

Niels Andersen, with his positive behaviour and motivation, which were really good sources of my strength at difficult moments.

Riccardo Biondi, Yongcun Cheng, Olivier Chanrion, Stavros Kotsiaros, Joanna Fredenslund Levinsen, Tina Ibsen, Ioana Stefania Muresan and Matija Herzeg; they were always with me with their nice friendship and behaviours, which were the biggest support for me through my study. And, I am very glad that I have a lot of good pictures and memories in my mind with them.

My dear '*Space*' friends at the institute Livia Kotler, Maulik Jain, Peter Limkilde Svendsen, Jens Emil Nielsen, Johan Nilsson and Eric Jürgen Haase with whom I spend very nice time through my PhD.

And, Birte E. Hede, Lene Bettenhaus and Simon Ekholm; without their curial helps my PhD study would be difficult for me.

Finally, my dear mom, dad and sister, who always accept me with their nice and patient manners.

Contents

List of Figures

Chapter 1

Introduction

1.1 Motivation

The troposphere is the region of the atmosphere where thunderstorms are formed with powerful lightning discharges at a global rate of ∼40 flashes pr. second (Christian et al., 2003). Above the troposphere is the stratosphere, extending to ∼50 km altitude, and the mesosphere reaching from the stratosphere to the bottom ionosphere at ∼80 km altitude. The mesosphere is one of the least explored regions around the Earth because it is too high to be reached by balloons and too low to be explored by in-situ observations from satellites. However, in this layer, processes originating in outer space interplay with processes from the troposphere below.

The Nobel Laureate C.R.T. Wilson suggested in the 1920'ies that thunderstorms could discharge to the ionosphere and that so-called "runaway" electrons, with energies of several MeV, could be generated by the electric fields in thunderstorms (Wilson, 1925). The energetic electrons would radiate bremsstrahlung from interactions with the neutral atmosphere, which, if the theory was correct, could be observed on the ground. For many years following, scientists attempted to measure the radiation, with little or marginal success (McCarty and Parks, 1985). However, in 1990 events took a dramatic turn with the discovery of electric discharges in the mesosphere above thunderstorms, later named "sprites"

(Franz et al., 1990), which seemed to support Wilson's earlier prediction. Since then, several other discoveries followed, including the "blue jet" in 1994 which is lightning propagating upward to the stratopause at 50 km altitude (Wescott et al., 1995) and the "gigantic jet" in 2002 of lightning from clouds to the ionosphere at 80 km altitude (Pasko et al., 2002; Su et al., 2003). These optical emissions are often referred to as "Transient Luminous Emissions" (TLEs).

A further important discovery was made in 1993 of ms-duration pulses of X- and gamma-radiation by the Compton Gamma-ray Observatory (Fishman et al., 1994). While first discarded as detector noise, it was realized that emissions where always observed when the satellite was above thunderstorms. Such emissions are now named "Terrestrial Gamma-ray Flashes" (TGFs). Today we also know X-and Gamma-radiation from laboratory discharges (Dwyer et al., 2005; Nguyen et al., 2009) and from lightning stepped leader propagation (Dwyer et al., 2005; Moss et al., 2006). It is understood that the radiation comes from bremsstrahlung from high-energy electrons accelerated in the electric field of discharges or fields inside a storm cloud as predicted by Wilson, although the precise acceleration process is not fully understood.

1.2 Scientific goals

This dissertation presents a model for electrons accelerated in a thunderstorm electric field and radiating bremsstrahlung from interactions with the atmosphere. The study is related to a mission planned for the International Space Station in 2016: "The Atmosphere-Space Interactions Monitor" (ASIM) for observations of extreme thunderstorms and their influence on the atmosphere. The mission will be the first that is directly dedicated to investigate TGFs and their relation to lightning and TLEs. The code developed in this Ph.D. study and the scientific insights gained will be relevant for the analysis of data from ASIM.

The specific goals of the project are:

1. To develop a model for electron acceleration in an electric field in the atmosphere, including such processes as collisional scattering, ionization and bremsstrahlung emissions.

2. With the model to investigate the bremsstrahlung source and its dependence with thunderstorm characteristics.

3. To estimate the properties of radiation at satellite altitude after photons have traversed the atmosphere.

4. To understand what can be deduced from satellite observations of the source characteristics.

1.3 Structure of thesis

In Chapter 2, we introduce the basic concepts of atmospheric electricity with focus on thunderstorm properties and the electric fields that power TGFs. In Chapter 3, we introduce some of the theories for generation of Terrestrial gamma-ray flashes (TGFs). The simulation model is described in Chapter 4, and some results from the model of the radiation source are given in Chapter 5. In Chapter 6 we translate the photon source to satellite altitude using a method developed by others, which take into account the various absorption and scattering processes with the atmosphere. In Chapter 7, we present our conclusions relating the physics of the radiation mechanisms.

Chapter 2

Earth's atmosphere electricity

2.1 The electric gas discharge

A gas discharge develops when the electric field of the gas reaches a certain magnitude where free seed electrons are accelerated to energies where they cause additional ionization and start an electron avalanche. Free electrons of the atmosphere are continually created by such sources as ionization from cosmic rays and radioactivity in the Earth's crust, or, in the case of the ionosphere, by photo ionization by solar UV radiation. The free electrons are lost by attachment to neutral atoms and molecules forming negative ions, or by recombination with positive ions. When an electric field is present, an additional source of free electrons come from the impact ionization of neutral species. An electron avalanche forms when the source of fresh electrons exceeds the losses of free electrons. The threshold field, E_k, is ~ 3.2 MVm^{-1} at sea level pressures. The development of an electron avalanche is often called a Townsend discharge.

For an electron avalanche to form, the field must accelerate a sufficient amount of electrons to energies that exceed the ionization energy which is $\sim$15 eV in air. The energy gained from the electric field is proportional to the distance over which an electron is accelerated and is therefore closely related to the mean free path of an electron. This means that the threshold field is proportionally smaller for smaller neutral densities. Therefore, one often refer to the "reduced" electric

field E/n_n, where n_n is the neutral gas density, because it is independent of the neutral density and therefore, in our case, (almost) independent on altitude. The reduced field is given in units of Td (Townsend) with 1 Td = 10^{-21} Vm^2. The threshold of the atmosphere is $\sim$120 Td.

When an electron avalanche grows it will reach a point where the space charge electric field of the plasma becomes comparable with the electric field driving the discharge. The electron ionization wave is called a streamer. Streamers can be of positive or negative polarity. A negative streamer propagates in the direction of the electron avalanche in the direction opposite to the electric field as from cathode to anode. A positive streamer propagates in the opposite direction, but is still an electron ionization wave. A positive streamer depends on photo-ionization which creates free electrons that are drawn towards the streamer. Once the ionization waves are formed, their own electric space charge fields will add to the background field, lowering the requirement on the magnitude of this field. For positive streamers, propagation is sustained for background field down to $\sim 0.1E_k$ and for negative streamers $\sim 0.4E_k$. This means that streamers, once formed, can propagate into regions of lower ambient electric fields as in the case of sprites, where positive streamers extend from the mesosphere into the stratosphere.

If the current source is sufficient, the neutrals are heated to several thousand degrees where they ionize, dramatically increasing the electron density and the electric conductivity, allowing a substantial fraction of the potential of the source to extend to the tip of the leader channel. This is a distinct mode of discharge as seen in lightning. Lightning propagates by a multitude of filamentary streamers feeding the leader.

The discharge process described above is the conventional one which is driven by supra-thermal electrons of a distribution that in general has temperatures below 1 eV. The runaway discharge, on the other hand, is driven by high-energy electrons and their high-energy secondary electrons. To understand the runaway discharge, it is useful to consider the plot shown in Figure 2.1. It shows the average frictional force on an electron as a function of the electron energy. The force is the result of all the scattering processes (see later sections) experienced by an electron. The cross sections of these depend on the energy of the electron and peak around 100 eV. Also shown on the figure are the electric fields that balance the frictional force. At the conventional breakdown field at sea level, 32 kV/cm, an electron that propagates anti-parallel to the electric field will on average be able to reach as much as $\sim$30 eV (if not absorbed before) but will very unlikely be accelerated to energies beyond 100 eV of the maximum frictional force. On the other hand, if a seed electron has an energy beyond $\sim$10 keV, it will encounter a *decreasing* frictional force if accelerated further, which leads to increased acceleration. This regime is the "runaway" regime.

The runaway discharge has a threshold field $\sim 0.1E_k$.

The electric gas discharge has been described in numerous books and articles. The conventional discharge is treated in e.g. Raizer (1991) and the runaway discharge in Babich (1995).

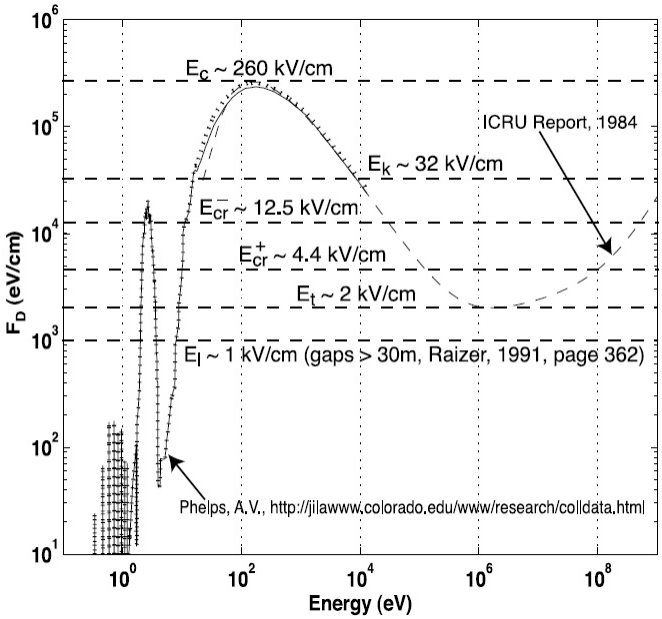

Figure 2.1: The frictional force, F_D on electrons in air at ground pressure as a function of electron energy (Moss et al., 2006). Electric fields balance F_D (see text).

2.2 Thundercloud electrification

Clouds may charge electrically through a variety of mechanisms. The most important for thunderstorm clouds is the collision between ice crystals whereby charge is exchanged. The lighter crystals are carried to high altitudes by vertical convection and collide with larger crystals that descend by gravity. When they collide, the heavier crystals receive electrons from the lighter ones resulting in an overall surplus of positive charge at the top of the clouds and a negative one at the bottom. The electrification is driven by solar energy that power the vertical convection via heating of the land. Thunderstorms are therefore most common

over land at mid- and low latitudes and tend to peak in intensity during the afternoon. Figure 2.2 shows the global average occurrence of lightning flashes detected from spacecraft carrying the Lightning Imaging Sensor (LIS) and the Optical Transient Detector (OTD) (Betz et al., 2009).

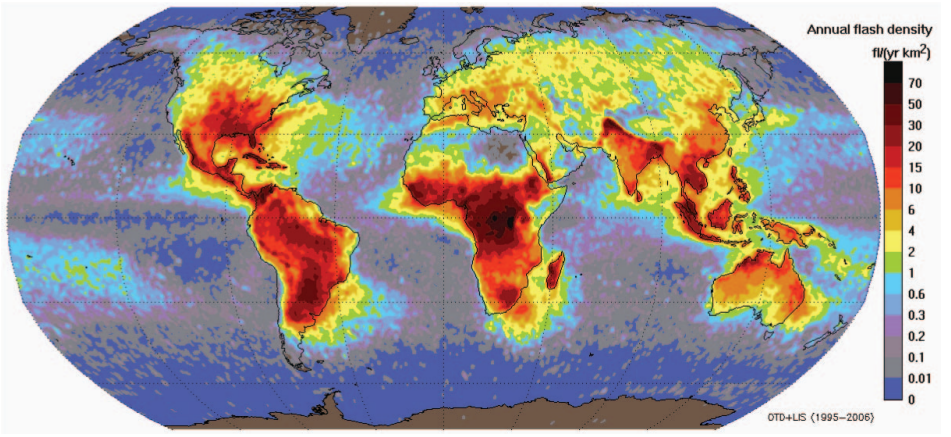

Figure 2.2: Global distribution of annual lightning flash density (flashes($km^{-2}yr^{-1}$)) from 11 years of space observations (OTD, LIS 1995 - 2005) (Betz et al., 2009).

There are three distinct regions of high activity: Africa, Americas and Asia. A combined global effect of thunderstorms is the global electric current of the atmosphere which flows from the (largely) positive polarity thunderstorm tops to the ionosphere, returning to the Earth in the fair weather regions. The fair weather current is $\sim$1 pAm^{-2} and the fair weather electric field at sea level $\sim$150 Vm^{-1}.

However, the charging process and the charge distribution are more complex than outlined above. The polarity of the charge exchange is associated with the properties of particles and drops and their temperature. Charge transfer occurs in collisions between ice crystals (moving upwards) and graupel (falling down), but not for wet hailstones (Saunders and Brooks, 1992). It has been showed that the graupel charge negatively at $< -10^o$ (Jungwirth et al., 2005; Betz et al., 2009) with a peak charging rate at $\sim -16^o$ (Berdeklis and List, 2001). Conversely, thunderclouds are generally charged positively for temperatures at $> -10^o$ (Jungwirth et al., 2005).

The charging process further depends on the relative humidity, which also determines the diffusional growth rate of the ice surfaces and the structure of the

ice crystals. For instance, the negative charging rate increases with increasing relative humidity. Conversely, positive charge can be transported by highly supercooled cloud water droplets even at temperatures down to $\sim -20^o$, which is consistent with polarity reversal of severe thunderstorms with wide and intense updrafts (Lang and Rutledge, 2002).

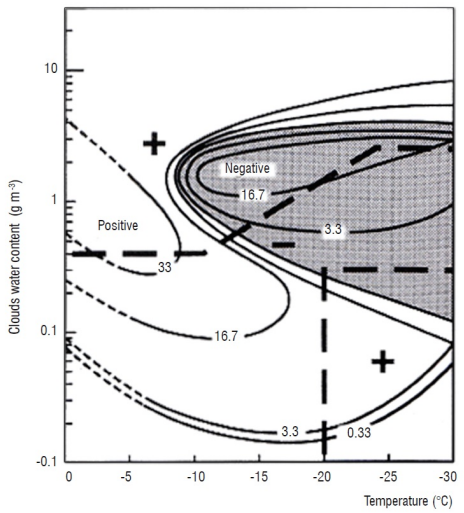

Figure 2.3: Polarity of charge gained by rimed graupel after a collision with an ice crystal, as a function of ambient temperature and liquid water content for the Takahashi (1978) experiment (curves) and for the Saunders et al. (1991) experiment (lines). The dashed bold lines outline the temperature and liquid water content values at which the charge of the graupel changes its polarity (Soula, 2012).

Figure 2.3 shows the polarity of charge gained by rimed graupel after a collision with an ice crystal, as a function of ambient temperature and liquid water content for the Takahashi (1978) experiment (curves) and for the Saunders et al. (1991) experiment (lines). The dashed bold lines outline the temperature and liquid water content values at which the charge of the graupel changes its polarity (MacGorman and Rust, 1998).

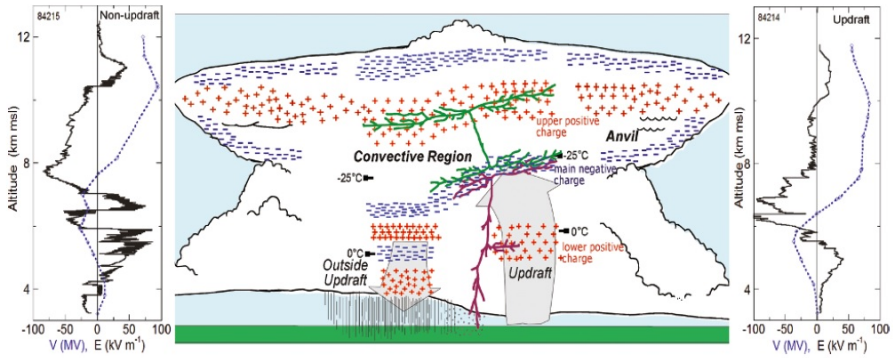

Figure 2.4: Electric fields in thunderclouds (Betz et al., 2009).

The charge structure, electric field and electric potential of thunderstorm clouds can therefore be significantly more complex that the simple bipolar structure. A conceptual model is shown in Figure 2.4 (Stolzenburg and Marshall, 2009), where positive regions are red and negative regions blue. The figure shows the main regions of a typical cumulus nimbus cloud with a core of vertical updraft, a region of downdraft or no draft and a stratiform region at the top extending horizontally from the core. The electric field and the potential V are shown of the non-updraft region (left) and the updraft region (right).

There are relatively few electric field observations in thunderstorm clouds because of the complexity of launching balloons directly into clouds and the fragility of the instruments. A summary of 50 balloon experiments is shown on Figure 2.5. The largest values of the electric fields observed are shown inside the updraft region (full markers) and outside (open markers). The markers also indicate the different storm types. Circled and boxed values are extreme cases where lightning occurred close to the balloon. The theoretical fields for different discharge conditions are shown for comparison. As mentioned earlier, the fields scale with the density and therefore are decreasing with altitude.

Note that Figure 2.5 introduces the concept of a threshold field for "Hydrometeor-enhanced conventional breakdown". Breakdown is is thought initiated from a crystal carrying electric charge through the enhanced field at the crystal tip structures, similar to the case of the enhanced field in a streamer. This field is about $0.1 * E_k$ and is lower than E_k. It brings up a point that will be important for our discussions in the following chapters, namely the distinction between large-scale and small-scale fields. The large scale fields are those given by the large scale charge distributions shown on Figure 2.5 and extend over regions

>10 m. The small scale fields are those around lightning leader tips, streamer tips and hydrometeors and extend over regions <10 m.

A final comment on the accuracy of the quoted threshold fields. The magnitudes are determined from a mixture of theoretical considerations and laboratory experiments. However, the actual values can vary by tens of % because the microphysics of discharges still cannot capture the complete physics including the boundary conditions. In laboratory experiments, for instance, the electrode material, geometry or surface finish may influence the field value at which a discharge is initiated and theories may be oversimplified because of the complexities of the physics. The fields shown on Figure 2.5 should be understood in these terms. In practice it is then difficult to distinguish between the conventional hydrometeor-enhanced discharge and the more exotic runaway discharge. Both are candidates for initiating lightning.

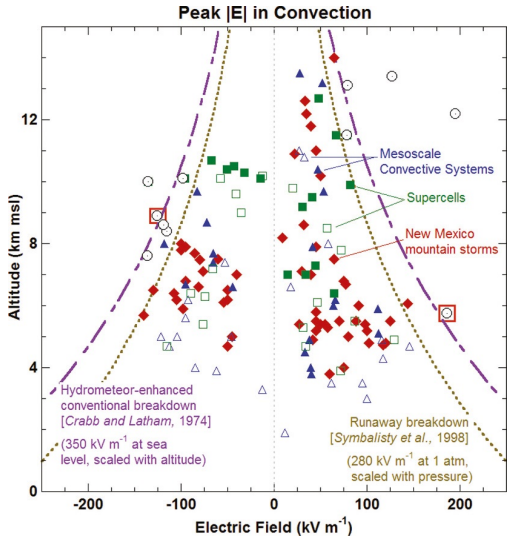

Figure 2.5: Observed electric field at altitudes of relative maxima and minima in more than 50 balloon soundings through convection, compared to theoretical initiation thresholds as a function of altitude. Typical values within updrafts (filled marks) and outside updrafts (open marks) of three storm types are shown. Circled values are extremes associated with close lightning; two values enclosed by red boxes are at known distances of 1100-2100 m from a subsequent lightning initiation location based on lightning mapping data (Marshall et al., 2005; Stolzenburg et al., 2007, in Betz et al., 2009).

2.3 Lightning

The lightning flash is electric breakdown between opposite charge regions whereby charge is transported between the regions, reducing their potential difference. The most common forms of lightning are intra-cloud lightning (IC), followed by negative cloud-to-ground lightning (-CG), lowering negative charge to the ground (∼10% of lightning strikes) and positive cloud-to-ground lightning (+CG) lowering positive charge to the ground to cloud (∼GC) (about 1%). Lightning is covered in a number of textbooks. A few are Uman (2001), Rakov and Uman (2003), Betz (2004) and Coorey (2004). Below we give just the main characteristics of lightning relevant for our studies.

Negative cloud-to-ground lightning typically begins with preliminary breakdown in the lower negative polarity regions of a cloud that develops into a leader channel that propagates downwards in steps of 10-100 m. As the channel approaches the ground, an opposite polarity channel reaching upwards may be stimulated from a structure like a tree where the electric field concentrates. When the two meet (the attachment process) good electric connection is created between the cloud and the ground. At this point, a highly luminous return current stroke is generated, lowering large amounts of charge. The peak current can reach typically 30 kA lasting 1-20 ms. Because the charge region in the cloud now is partially neutralized, a new field structure is established that may stimulate further discharges in the cloud, eventually leading to a dart leader propagating at a high velocity downwards in the already established channel, leading to further return strokes. The processes may repeat causing a flickering of the lightning channel observable by the eye.

Positive cloud-to-ground lightning occurs less frequently, but are generally more powerful. Their peak currents can reach 300 kA, lowering several hundred coulomb. They cause therefore significantly more damage to the structures they strike. Because they are less frequent, less is known about them. However, it is thought that the first positive leader may propagate continuously or in a stepped fashion. The return current can last several hundred ms and the +CG channel may develop backwards from its origin in the cloud, extending several tens of km in the stratiform region of a cloud. This is so-called spider lightning. Positive flashes are usually single stroked.

Both positive and negative polarity lightning propagates by means of a multitude of streamers injected from its tip.

However, the lightning initiation process is debated and at least two mechanisms are debated as mentioned earlier: hydrometeor seeds (Bazelyan and Raizer, 1998) or high-energy electrons generated by cosmic rays (Gurevich et

al., 1992). See discussions in (Gurevich et al., 2003; 2004; 2009) and (Gurevich and Karashtin, 2013).

The necessary background field for leader propagation is about 60 - 100 kV/m in the bulk of the cloud (Rakov and Uman, 2003; Cooray, 2004). This background electric field is also sufficient lightning initiation.

Of particular relevance to the present study are those lightning processes that are associated with TGFs. Around the time of the discovery of TGFs, observations were made of X-ray radiation from a lightning striking a lightning rod (Moore et al., 2001). So clearly, the tip of the leader channel can be a source of radiation. Further investigations suggested that the stepping of the leader create impulsive high electric fields that generate radiation. The conclusions were reached in rocket triggered lightning and in the laboratory (Dwyer et al., 2012).

2.4 Transient Luminous Emissions (TLEs)

In 1990, a paper was published that reported large brief flashes in the mesosphere (50-80 km) above a distant thunderstorm. The observation was made in Minnesota, USA, with a low-light, TV-frame rate camera (Franz et al., 1990). It was the first (scientific) observation of an electric discharge above thunderclouds. Later named the "sprite", the discovery attracted much attention and many experimental observational campaigns were conducted to observe this phenomenon, first in the US, and later in many other countries including Europe (Haldoupis et al., 2004). The activity led to many new discoveries including the "elve" (Fukunishi et al., 1996), the blue jet (Wescott et al., 1995) and the "gigantic jet" (Pasko et al., 2002) followed. The common name for these emission sometimes used is Transient Luminous Emissions (TLEs). The discharges are illustrated in Figure 2.6.

By now, the sprite is fairly well understood. It is made of streamers, ranging from single elements to a collection of streamer elements extending over a volume that can be tens of km wide (Sentman et al., 1995). The streamer elements reaching down-wards in the atmosphere are of positive polarity while negative recoil streamers may shoot upwards towards the ionosphere (e.g. McHarg et al., 2007). The streamers are generated by the quasi-electrostatic field from (usually) a positive cloud to ground lightning discharge in a thunderstorm below and may last up to several tens of ms. The elve is concentric rings of illumination expanding horizontally at the bottom ionosphere above a lightning discharge. It lasts < 1 ms and is ionization and heating of the lower ionosphere powered by the electromagnetic pulse from a lightning strike. The blue jet is lightning

expanding upwards to the stratopause at 40-50 km altitude, and the gigantic jet is lightning propagating from the clouds to the ionosphere boundary at 80 km altitude. The blue jet is thought to be a leader assisted by streamers at the tip, just like regular lightning, and the gigantic jet to be a blue jet that has sufficient potential to reach altitudes where the streamers can flash to the ionosphere (e.g. Neubert et al., 2013).

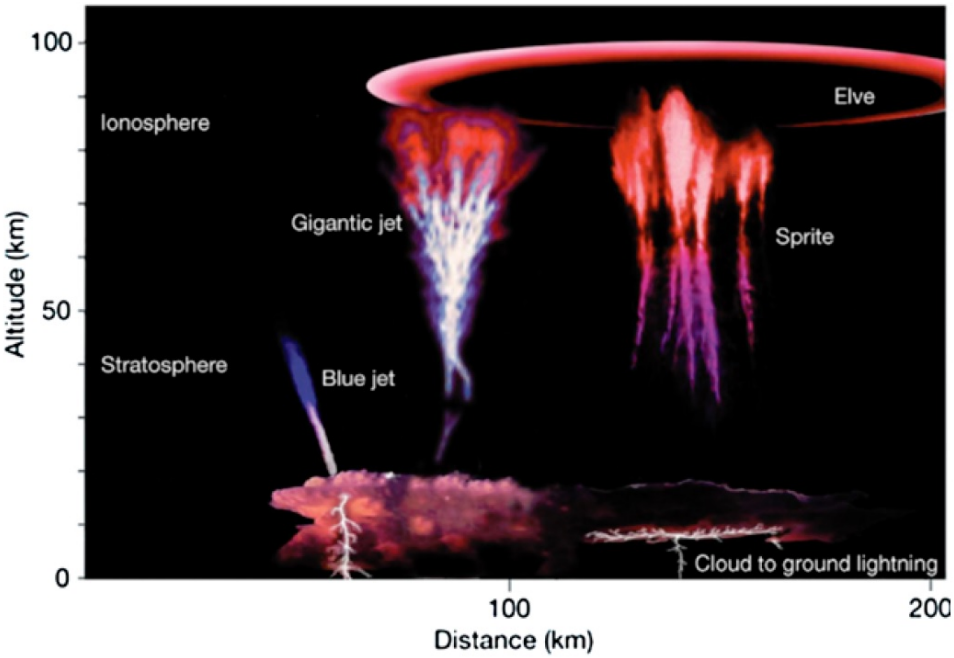

Figure 2.6: Transient Luminous Emissions (TLEs) in the upper atmosphere (Roussel-Dupre et al., 2008).

Simulations have shown that negative streamers may generate runaway electrons (Chanrion et al., 2008, 2010; Dujko et al., 2013) and therefore sprites, jets and gigantic jets could potentially be sources of TGF radiation. However, as we shall see in the following, the TGF source appears to be at lower altitude and close to, or inside, the clouds.

2.5 Terrestrial Gamma-ray Flashes (TGFs)

In 1994, brief emissions of X- and Gamma-ray photons from the Earth's atmosphere were discovered by the Burst and Transient Source Experiment (BATSE) instrument on the Compton Gamma-Ray Observatory satellite (CGRO) (Fishman et al., 1994). These "Terrestrial Gamma-ray Flashes" (TGFs) appeared to last a few ms and were detected in four energy bands: 25-50, 50-100, 100-300 and >300 keV. The CGRO satellite took observations from 1991-2000 and recorded somewhat less than 1 TGF per month. The low number was in part caused by the threshold criterion adopted for burst detection, which was designed for cosmic flashes (Nemiroff et al., 1997).

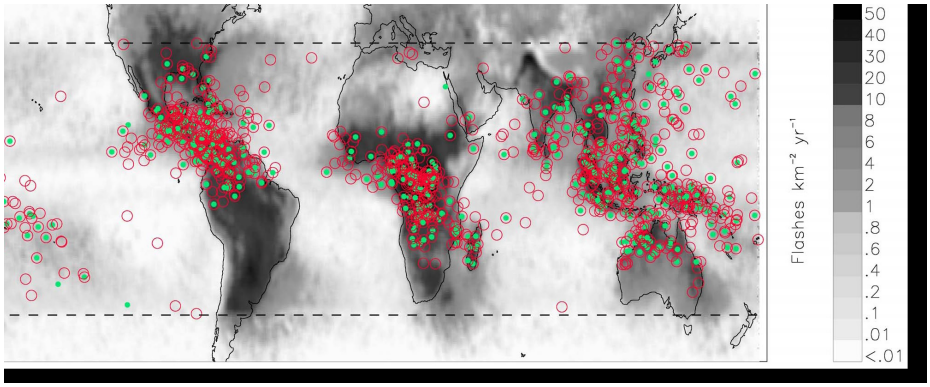

Figure 2.7: RHESSI TGFs for the years 2004, 2005 and 2006. The red circles are TGFs found with the new search algorithm (1012 TGFs) and green dots are TGFs from the RHESSI TGF catalog (474 TGFs). There are no TGFs in most of South America since RHESSI does not provide data for this region (SAMA). The grey scale indicates lightning activity measured by LIS/OTD. The dashed lines are the limits of the RHESSI 38^o inclination orbit. (Gjesteland et al., 2012).

The number greatly increased with the launch in 2002 of the Reuven Ramaty High Energy Solar Spectroscopic Imager (RHESSI) satellite. The detector has better energy resolution and all data are transmitted to the ground. The RHESSI TGF data search algorithm found 10-20 TGFs per month (Smith et al., 2005). Later refinement of the algorithm yielded more than twice this amount. Applying the detector to data from 2004-2006, 1012 event were found compared to the original RHESSI cataloge of 474 events (Gjesteland et al., 2012). Figure 2.7 shows the geographical distribution of the events identified. Green dots are the original events and the open circles the fainter events detected by

the improved algorithm. (The RHESSI detector does not allow identification if the photon arrival direction, thus the points on the figure are the geographical location of the satellite ground point at the time of the events.)

Because of the geographical distribution of TGFs and their coincidence with thunderstorm activity, it was proposed early that they were associated with thunderstorm electric fields and bremsstrahlung from energetic electrons accelerated in the electric fields of the storm clouds, as proposed by Wilson (Fishman et al., 1994). It was further suggested that sprites are the source of TGFs because sprites occur high in the atmosphere where photon absorption is small and because the temporal characteristics resembles those of sprites (Nemiroff et al., 1997). The spectrum of photons observed on satellite is affected by Compton scattering in the atmosphere, and may, therefore, contain information on the altitude of the source of the emissions. From the spectrum it was suggested that the source altitude is above ∼25 km, depending on the hardness of the source spectrum (Smith et al., 2005), and in another study, that more than half of the events came from below 20 km, with an significant amount from 30-40 km (Østgaard et al., 2008). Further studies of the BATSE spectra, compensating for loss of photons from dead-time problems of the detectors, reduced the estimated altitudes to below ∼30 km (Gjesteland et al., 2010), and the thoughts are now that the source altitudes may be below, or close to, the tropopause. This now suggests that the lightning processes in the clouds are the source of TGFs (Østgaard et al., 2013).

The observations from RHESSI was followed by the Italian Space Agency mission Astrorivelatore Gamma a Immagini Leggero (AGILE) launched in 2007. AGILE carries detectors for photons up to 30 GeV (Marisaldi et al., 2010). The first AGILE observations extended TGFs emission energies to up to 40 MeV lasting several milliseconds (Marisaldi et al., 2010). The AGILE observations showed a typical exponential cutoff energy around 10 MeV (Marisaldi et al., 2010), which agreed with the average energy of 7.2 MeV proposed by Dwyer (2003). However, model results were challenged by the recent AGILE TGF detection of photons with energies up to 100 MeV (Tavani et al., 2011).

Most recently, the Gamma-ray Burst Monitor (GBM) on the Fermi Gamma-ray Space Telescope have reported TGF observations (Briggs et al., 2010). The maximum emission spectra appear to be around 30 MeV, and they were shown to be directly associated with lightning events.

The source region of the TGFs were first thought to be high altitude optical emissions, i.e. sprites, although this was disproved later by Gerken et al. (2000). Inan et al. (1996) were studied TGFs associated with thunderstorm using radio signals. The analysis of lower frequency radio emissions brought TGFs source within thunderclouds (Cummer et al., 2005; Dwyer et al., 2012).

Chapter 3

Theories for Terrestrial Gamma-ray Flashes (TGFs)

When Wilson first considered thunderstorm electric fields and their effects on the environment, he hypothesized that runaway electrons should be generated in thunderstorms, perhaps reaching the ionosphere. It was clear that the electrons would interact with the atmosphere and create bremsstrahlung, which in the following years led to several fruitless attempt to measure the radiation. It was not until the aircraft experiments in thunderstorms in the 1980ies (Parks et al., 1981; McCarthy and Parks, 1985) and the balloon experiments in the 90ies (Eack et al., 1996a,b, 2000) that the radiation was observed. It was found to be several orders of magnitude above the background level on second to minute duration time scales, disappearing when the electric field was reduced, for instance by a lightning discharge. The conclusions from these experiments were that radiation is common in thunderstorms, both in the core and in the anvil (Eack et al., 2000).

The radiation described above is different from the ms-duration bursts of TGFs observed from satellite, but constitutes the radiation environment of thunderstorm clouds. The impulsive nature of TGFs requires an impulsive electric field, typical of a lightning discharge or stepped leader propagation. In this regard, one must consider both the large- and small-scale electric fields as mentioned earlier.

Theories for TGF radiation naturally consider the generation of high-energy electrons which, referring to Figure 2.1, are in the runaway regime. However, they differ on the exact mechanism of seeding the runaway regime with sufficient number of high-energy electrons to achieve the measured flux levels. There are three main mechanisms that we will describe in the following: (1) the basic Relativistic Runaway Electron Avalanche (RREA) which may be seeded in different ways, but originally thought seeded with runaway electrons created by cosmic rays, (2) Thermal Runaway Electron Seeding (TRES) where a streamer discharge under certain conditions may accelerate electrons into the runaway regime, and (3) the Relativistic Feed-Back Model (RFBM) where the number of avalanches are multiplied by positron and backscattered photon feed-back. The following gives a short introduction, further discussion are found in Dwyer et al., (2012).

3.1 The Relativistic Runaway Electron Avalanche (RREA)

Wilson's discussion in 1925 discussed runaway electrons born in the runaway energy regime and further accelerated to higher energies, but it did not directly mention the a runaway electron avalanche, but rather a the less definite "snowball" effect. The aircraft and balloon experiments, however, suggested that cosmic ray secondary electrons were insufficient to explain the radiation levels and that an amplification mechanism was needed.

In 1992, Gurevich et al. suggested a theoretical mechanism for energetic avalanches in the upper atmosphere assuming a few seed electrons by cosmic rays. If the electric field is above the runaway threshold field, E_t, (Figure 2.1) a seed electron in the runaway regime will create many secondary electrons through impact ionization of atmospheric constituents and a few of these will have energies above the runaway threshold for corresponding to the electric field, thereby increasing the number of electrons in the runaway regime or, in other words, creating an avalanche, thereby increasing the bremsstrahlung radiation level. This is the Relativistic Runaway Electron Avalanche. It was further suggested that the RREA could cause electric breakdown and could be important for the initiation of lightning.

The theory gained much interests with the discovery of TGFs and a multitude of studies followed, refining the model. Roussel - Dupre et al. (1994; 2008) presented a kinetic expression using the Boltzmann equation and several others adopted a Monte Carlo approach. The codes differ in how and which the cross-sections are included, but appear now to converge towards consistent results

(Dwyer et al., 2012). Some of the important groups and codes are represented by Lehtinen et al. (1999) which includes the influence of the Earth's magnetic field, Babich et al. (2001; 2004), Dwyer et al., (2003) and Carlson et al. (2007).

The codes give by and large, the same avalanche lengths and same average energy (Dwyer et al., 2012). However, it has been suggested that the RREB itself will not change the atmospheric conductivity sufficiently to power electric breakdown and therefore remains an avalanche (Dwyer and Babich, 2011).

3.2 Thermal Runaway Electron Seeding (TRES)

In the RREA theory, the runaway seed electrons are generated by cosmic ray showers. An alternative to this external seed electron source are the high fields in streamer heads or leader tips which in principle should be able to provide sufficient energy to accelerate electrons from thermal energies and into runaway energies. Moss et al. (2006) showed that if the streamer tip field is $E \sim 7.5E_k \sim E_c$ (Figure 2.1) the electrons would be accelerated into the runaway region. However, such high fields are rare, even in streamer tips and this mechanism alone cannot explain TGFs because the total energy gained by an electron is limited to a few keV (Moss et al., 2006). The scenario now considered is that a multitude of streamers feeding a lightning leader accelerate electrons into the runaway regime and that the field of the lightning leader further accelerates the electrons to the MeV energies required for TGFs (Celestin and Pasko 2010).

Other studies of of TRES (which is an acronym we have adopted in this thesis for convenience) include Chanrion and Neubert (2008; 2010) who present a full Particle-In-Cell (PIC) code for the electrons of a streamer and couple it with a Monte Carlo approach for descriptions of the interactions with the atmosphere. In these papers it was pointed out that the acceleration process is stochastic and gives a finite probability for electrons to be accelerated into the runaway regime for any field value (although with very low probabilities for low fields) and that the first runaway electrons in a streamer simulation appeared at $E \sim 5E_k$. This field value is within range of realistic streamer head field magnitudes.

The observations of high-energy radiation in the laboratory (Nguyon et al., 2009) and from lightning (e.g. Moore et al., 2001; Dwyer et al., 2003) suggest a very localized source region around the tip of the discharges. This seems to preclude the RREA because it has longer avalanche lengths (see later). The TRES mechanism, coupled with a leader field, is therefore an attractive for the explanation of high-energy radiation from lightning.

As evidence is mounting for lightning to be the source of TGFs (Østgaard et al., 2013), it could also be a serious candidate for TGFs, although it is debated if the flux levels at satellite altitudes will be sufficient (Dwyer et al., 2012).

3.3 The Relativistic Feed-Back Model (RFBM)

Dwyer (2003) introduced a very interesting theory for energetic photon emissions in the atmosphere. According this theory, one RREA may create several other RREAs on time-scales of a few micro-seconds, thereby enhancing the fluxes of energetic photons.

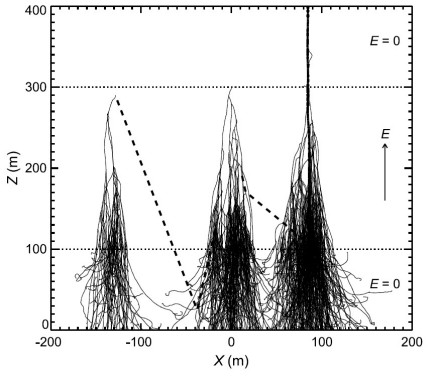

Figure 3.1: The runaway feedback mechanism (Dwyer 2003).

The model includes energetic photon emissions from bremsstrahlung which may be back-scattered (against the direction of the avalanche) causing ionization which may start a new avalanche. Or, energetic photons may create positrons by air production which will be accelerated in the opposite direction of the electrons and at some point start a new avalanche.

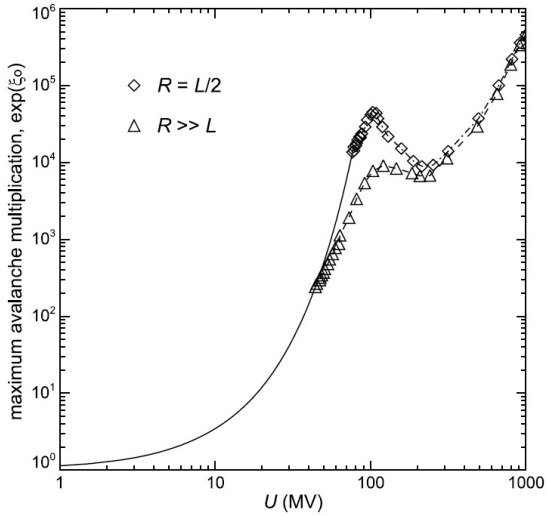

Figure 3.2: The maximum sustainable relativistic runaway electron avalanche multiplication factor, $\exp(\xi_o)$, versus total potential difference within the avalanche region. The data points (and the dashed and dashed-dotted lines) are the result of Monte Carlo simulations and show the threshold at which the discharge becomes self-sustaining ($\gamma = 1$). The data are calculated for the condition that the lateral radius, R, is much larger than the length of the avalanche region, L, and when it is one half the length (Dwyer et al., 2012).

If there for each runaway electron is created one new runaway electron, the discharge can continue indefinitely and it is called self-sustaining. Since the electric field will be modified, this condition can only be achieved for short periods of time. The runaway electron multiplication factor of a RREA, for the case where the feed-back model is self-sustaining, is shown in Figure 3.2. A multitude of avalanches can be generated in a very short time and the mechanism has been suggested to explain the flux levels of TGFs observed from satellite (Dwyer et al., 2008).

3.4 Summary of models

In summary we have discussed the models shown in Figure 3.3 (Dwyer et al., 2012). In addition we have discussed the seeding mechanism, which can be external to the discharge as for cosmic rays or internal as for the TRES mechanism.

In the following chapters we focus on the RREA and do not discuss the TRES or the FRBM any further as the focus of our work has been to develop a model for the RREA with careful consideration of the cross-sections formulations to be adopted.

The feedback mechanism is interesting mechanism and has an importance in the observed TGFs, as it could provide sufficient amount electrons to the avalanche independent of electric field and cosmic seed electrons. In our study, we also support this theory likely source of observed TGFs (see following text).

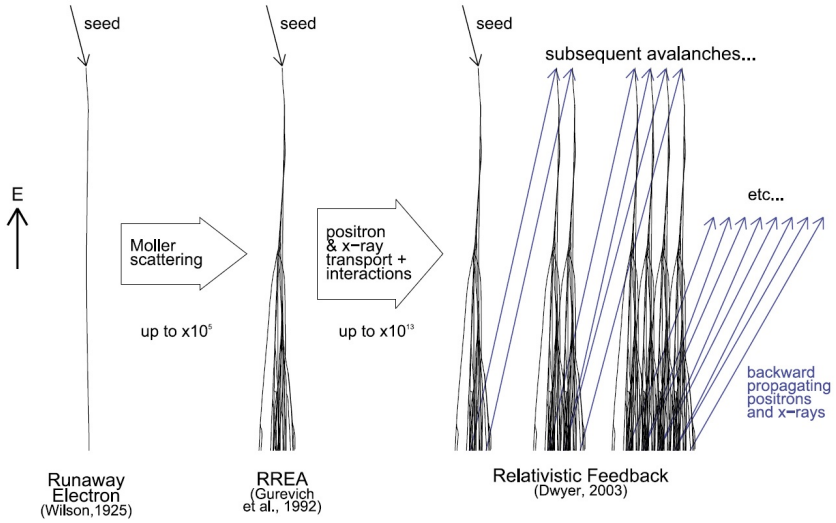

Figure 3.3: Comparison of different TGFs theories (Dwyer et al., 2012).

Chapter 4

Our simulation model of TGF generation

4.1 Introduction

There are several methods one can consider when simulating electric gas discharges. One can, for instance, solve the drift diffusion equation for electrons with analytical representation of electron-gas interactions, as has been common in the past (REFs). This approach will, however, miss the acceleration of electrons to high energies in discharges. To model this effect a kinetic formulation is needed like the Boltzmann equation, which describes the development in time of the electron distribution function, $f(\mathbf{r}, \mathbf{p}, t)$, where $\mathbf{r}$ is the position vector, $\mathbf{p}$ the momentum vector of electrons and t the time:

$$\frac{\partial f}{\partial t} - \{\frac{1-\mu^2}{p}\frac{\partial f}{\partial \mu} + \mu\frac{\partial f}{\partial p}\}eE = \frac{\partial_c f}{\partial t} \tag{4.1}$$

Here μ is the cosine angle between the electric field, $\mathbf{E}$, and $\mathbf{p}$, and $\partial_c f/\partial t$ is the Boltzmann collision integral for electron interactions with the species of the gas. This approach was used by Gurevich et al. (1992) and Roussel-Dupre et al. (1994; 2008) as mentioned earlier. While the formulation appears simple, it is

a challenge to solve the equation with sufficient accuracy on available computer platforms.

Instead we adopt the approach of Chanrion and Neubert (2008; 2010) where a Particle-in-Cell (PIC) model of gas discharges is presented. The code describes the acceleration and movement of electrons in an electric field and update the electric field according to electron and ion concentrations. The electron-gas interactions are described by the Monte-Carlo (MC) technique.

The MC module of Chanrion and Neubert includes the following processes:

- Elastic-, excitation- and ionization cross sections of electrons interacting with N_2 and O_2, extending to 10 keV electron energy
- attachment of electrons to neutral molecules
- Photo-ionization
- Emission rates of excited species

The model of Chanrion and Neubert was developed to study streamer propagation. It was discovered that some electrons were accelerated to high energies moving ahead of the streamer tip into the ambient gas. It was one of the first simulations of thermal electron acceleration of electrons into the runaway regime. To properly model the production of runaway electrons, however, the model is expanded in the following way:

- The cross sections for electron-gas interactions are extended from 10 keV to above 100 MeV
- Bremsstrahlung radiation is included

4.2 Implementation of the Monte Carlo scheme

The Monte Carlo (MC) method was developed in the 1940s to use numerical methods based on the random numbers. It is used to model complex physical and mathematical problems where the numerical solution to the analytical equations is difficult. The MC method is built on probabilities, for instance the probability that an electron in a time-step Δt undergoes an interaction with a

gas molecule. The probability is described with a random generator of the computer, weighted with the probability. In the case of electron gas interactions, probabilities are described by the cross-sections for the various interactions.

Monte Carlo simulation codes are generally based on two different schemes; one is the so-called Null collision (Skullerud, 1968; Lin and Bardsley, 1977; Reid, 1979) and the other is from Nanbu (1994).

The Null collision scheme was developed by Reid (1979) as an alternative to the direct method (McIntosh, 1974) with the purpose of reducing the computational load. The principle is to add a fake (null) cross-section to the real elastic and inelastic collisions in order to make the total collision frequency independent of the electron energy (Reid, 1979; Ramos, 1990). First, all the cross-sections for the collision processes considered are added to give one combined, total cross-section for interaction with the neutral gas, $\sigma_t(\varepsilon)$. This cross-section is dependent on the energy, ε, of the electron considered. The maximum cross section, σ_t^{max}, found for $\varepsilon \sim$100 eV, is then used to select electrons for possible collisions, and the time step of the Null scheme is chosen as:

$$\Delta t = \frac{\delta}{\nu_t^{max}} \tag{4.2}$$

where ν_t^{max} is the maximum collision frequency and δ is is an arbitrary number much less than 1 that is assumed to be 0.1 to fulfill the Vahedi condition that minimizes the effect of multiple collision in the time step (e.g. Moss et al., 2006, figure 6).

Electrons are first selected randomly for collision using the probability of $\simeq \delta$. When an electron is selected for collisions it will, in general, have an energy that is different from the energy that gives the maximum collisional cross-section and therefore have a smaller total cross-section. The *difference* between the maximum and the true, total cross section is added as an extra cross section with no collision associated with it. With this trick, a total of, say, 40 true cross sections to be handled by the code is increased to 41, where the last is an imaginary one with zero probability (e.g. Reid, 1979; Ramos, 1990; Moss et al., 2006). Finally, a random number determines the type of collision.

The other scheme is from Nanbu (1994) which is more efficient when a large number of collision processes are simulated. If we consider N_c different processes whereby and electron can interact with the gas, then the probability of a collision of type i, P_i, is:

$$P_i = n_n v \sigma_i(\varepsilon) \Delta t \tag{4.3}$$

where v is the electron velocity and $\sigma_i(\varepsilon)$ is the cross-section of the interaction. In the Nanbu scheme, an interval from 0 to 1 is divided into N_c segments of equal length, where each segment describes the probability of a particular type of interaction. Each segment is then divided into two, where the length of the first sub-interval represents the probability of the interaction and the second interval represents no interaction. The subdivisions depend, of course, of the time step adopted and of the electron energy, but for a given time step, one can from the start generate a table that covers all interactions and energies. At each time step, each electron then requires one call to a random number generator to determine its interaction, if any.

The time step chosen for the Nanbu scheme, however, is smaller than for the Null scheme, so more time steps are required. If the maximum cross section of the individual processes under consideration is σ_i^{max}, then the time step is given by the collision frequency associated with the largest of these, $\mathrm{Max}(\sigma_i^{max})$ and not the maximum of the total cross section as in the Null scheme:

$$\Delta t = \frac{1}{N_c \mathrm{Max}(\nu_{\mathrm{i}}^{\mathrm{max}})} \tag{4.4}$$

where N_c is the number of processes considered. In our model, $N_c = 41$ (nitrogen and oxygen, elastic, in-elastic (rotation, attachment, vibration, excitation, ionization)) and the time step of the Nanbu scheme is smaller by a factor ~ 0.57. However, the number of operations required at each time step are smaller, making the Nanbu scheme faster than the Null scheme. In the model the Nanbu scheme is therefore adopted.

4.3 Elastic collisions

As an electron moves through a gas, it collides with the gas atoms or molecules. These collisions are described as elastic when the total kinetic energy is conserved, that is, the sum of the kinetic energies of the colliding particles is the same before as it is after the collision.

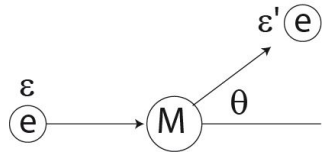

Figure 4.1: Elastic collision of an electron with a molecule. The vector describes the velocity of the electron before and after interaction with a molecule and ε, ε' are the electron energies before and after the collision.

In elastic collisions between electrons and molecules, the electron mass, m, is much smaller than the molecular mass, M, which implies that the energy loss by an electron is relatively small. However, the angular scattering can be large. It is usually described by the so-called "screened Coulomb potential" where the negatively charged, bound electrons are seen as a plasma cloud screening the positive nucleus. The probability of the scattering angle is almost isotropic over 4π at low energies and more forward-directed at high energies. Elastic scattering is described by a cross section that depends on the incident electron energy and the deviation angle, θ:

$$\sigma_e^i(\varepsilon, \theta) = \sigma_e^i(\varepsilon) I(\varepsilon, \theta) \tag{4.5}$$

where $\sigma_e^i(\varepsilon)$ is the elastic cross section with molecule species i and $I(\varepsilon, \theta)$ describes the angular probability after a collision. The formulation of the angular distribution is the same for both elastic and inelastic collisions and will be described later.

The elastic cross sections are taken from the BOLSIG+ package (Hagelaar and Pitchford, 2005). BOLSIG+ is an application for the numerical solution of the Boltzmann equation for electrons in weakly ionized gases in uniform electric fields. Under these conditions the electron distribution is determined by the balance between electric acceleration and momentum loss and energy loss in collisions with neutral gas particles. The elastic and inelastic cross sections of BOLSIG+ is based on Phelps (1985) and Phelps and Pitchford (1985) which are good up to 10 keV.

We have extended the cross sections to higher energies using a screened Rutherford cross section (Murphy, 1988)(in cm^2):

$$\sigma = \frac{2\pi z^2 e^4}{v^2 p^2 \eta(\eta+1)}$$
$$\eta = \frac{\chi_o^2}{2}[1 + 4\alpha z \chi_o(\frac{1-\beta^2}{\beta}\log\chi_o + \frac{0.231}{\beta} + 1.448\beta)] \quad (4.6)$$
$$\chi_o = \frac{\hbar\mu}{p}\frac{z^{1/3}}{0.885 a_o}$$

where z is the atomic number, e is the electron charge in esu, v is the electron velocity, p is the electron momentum, $\beta = v/c$, $\alpha = 1/137$ is the fine-structure constant, a_o is the Bohr radius of the electron, and μ is a parameter that adjust the formula to fit the cross section data. Data are used for 10 keV where μ is 0.635.

The elastic cross sections are shown in Figure 4.2 and 4.3.

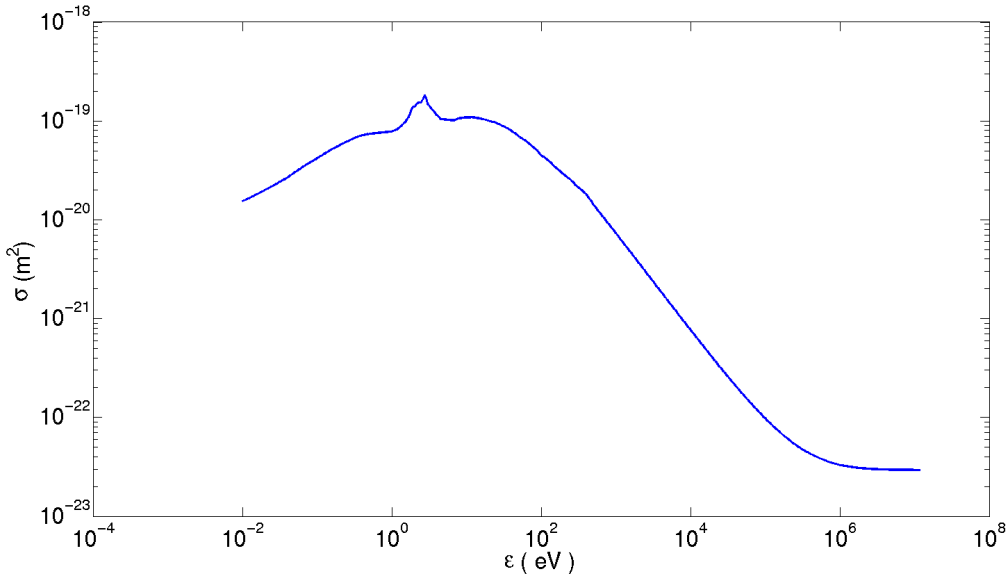

Figure 4.2: Elastic cross section for electron collision with N_2 from BOLSIG+, extended to high energies via Murphy (1988).

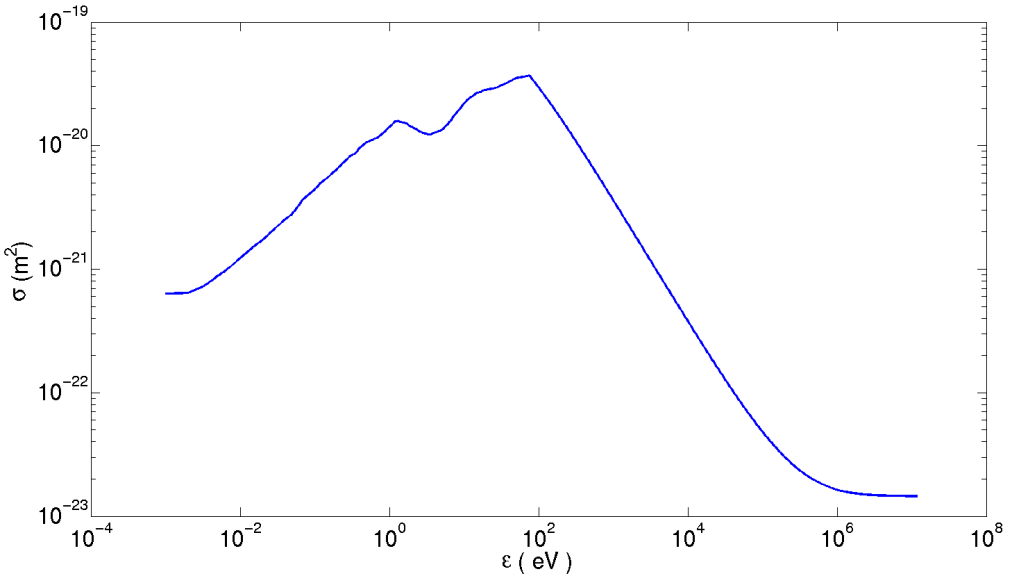

Figure 4.3: Elastic cross section for electron collision with O_2 from BOLSIG+,extended to high energies via Murphy (1988).

The energy loss during an elastic collision can be expressed by:

$$\varepsilon' = \varepsilon(1 - \frac{2m}{M}(1 - cos(\theta))) \tag{4.7}$$

where ε' is the kinetic energy of the electron after the collision. It is related to $I(\varepsilon, \theta)$ mentioned earlier and to the so-called momentum cross section that describes the average loss of momentum of a flux of particles through elastic collisions. We return to the scattering angle and a test case in a later subsection.

4.4 Inelastic collisions

A collision can be inelastic if the energy of the incident particle is above a value characteristic of the internal energy states of the target gas constituents. In this process the total energy of the colliding particle is conserved, but the

kinetic energy of the incident electron is not. In this section, we consider several type of inelastic collision: excitation, attachment and ionization. The angular scattering, and the angle of injection of a secondary electron in an ionization event, are treated as for elastic scattering and is described in a later section.

4.4.1 Excitation

Some of the kinetic energy of the particle may be absorbed in the target molecules in the form of excited orbital electron states, molecular vibration, or molecular rotation. The molecule may subsequently radiate this energy at specific wavelengths as it relaxes to a lower internal energy state. The radiation is emitted with a delay that depends on the lifetime of the excited state. The energy, ε', of an incident particle after an inelastic collision is:

$$\varepsilon' = \varepsilon - \varepsilon^* \tag{4.8}$$

where ε^* is the energy of the excitation process. Inelastic collision is shown schematically in Figure 4.4. The scattering angle is determined as for elastic scattering and will be treated in a later subsection.

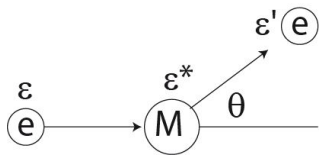

Figure 4.4: Inelastic collision of an electron with a molecule.

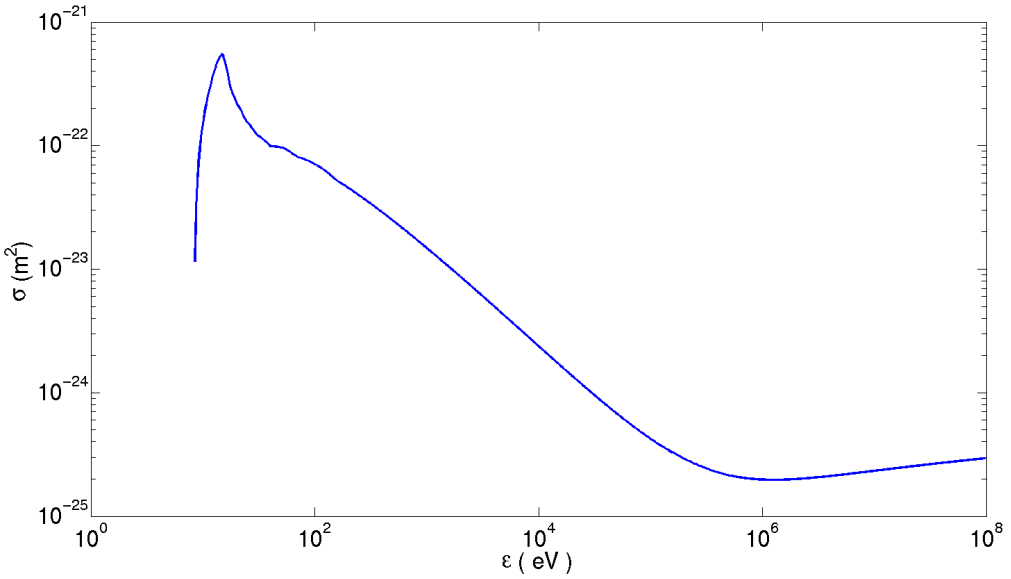

Figure 4.5: Electronic excitation cross section for electron collision with N_2 from BOLSIG+, extended to high energies using Murphy (1988).

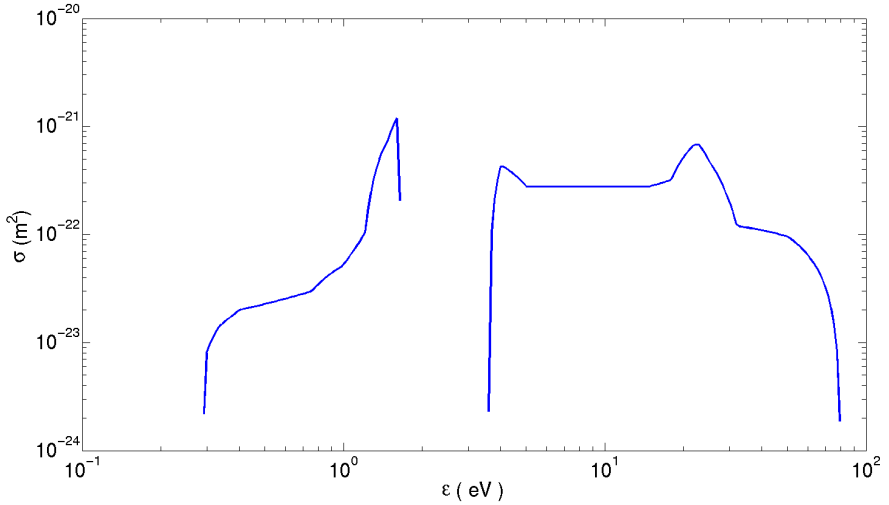

Figure 4.6: Vibrational excitation cross section for electron collision with N_2 (BOLSIG+).

The cross sections for electronic, vibrational and rotational excitation of N_2 are shown in Figures 4.5 - 4.7. For the high energies of our study, only the excitation cross section is of relevance. We only show it only for N_2 because it is very similar for O_2. The vibrational and rotational excitation cross sections are shown for completeness. They are included in the model and are useful for future studies of the secondary electron population.

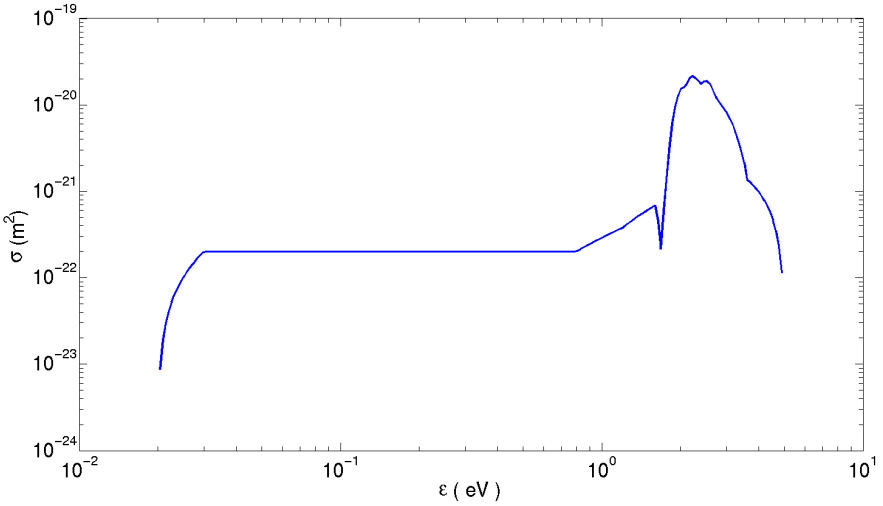

Figure 4.7: Rotational excitation cross section for electron collision with N_2 (BOLSIG+).

The excitation cross section is extended to high energies by, again, following Murphy (1988) who follows Banks and Kockharts (1973). They are (in cm^2):

$$\sigma(\varepsilon) = (q_o c_o f_o / W^2)[1 - (W/\varepsilon)^\gamma]^\nu (W/\varepsilon)^\Omega \tag{4.9}$$

where ε is the kinetic energy of the electron and $q_o = 6.51{*}10^{-14}\mathrm{eV}^2\mathrm{cm}^2$ and W is the threshold energy in eV. The coefficients $c_o, f_o, \nu, \gamma, \Omega$ are given in Table 6 in Murphy (1988).

4.4.2 Attachment

Attachment is a process in which an electron collision with an atom, molecule or molecules results in the formation of a negative ion.

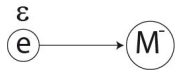

Figure 4.8: Attachment of an electron to a molecule.

In the model we consider two types of electron attachment to O_2, two-body dissociative attachment and three-body attachment:

$$e + O_2 \rightarrow O^- + O \tag{4.10}$$

$$e + O_2 + N_2 \rightarrow O_2^- + N_2 \tag{4.11}$$

When electron attachment occurs, the electron is simply removed from the simulation and further effects of negative ions on the electron population, i.e. owing to detachment or scattering, are not considered.

4.4.3 Ionization

An electron may ionize a molecule if its energy is is above the threshold for ionization, ε_{thr}, thereby creating a secondary electron and a positive molecular ion. The minimum energy required is $\varepsilon_{thr} \simeq 13.6$ eV for O_2 and $\simeq$14.5 eV for N_2. The cross section for ionization is again from the BOLSIG+ package, extended to high energies following Murphy (1988), where for incident electrons of energy above 15 keV a formula from Longmire and Longley (1973) is used, which is in turn is based on a calculation by Bethe (1930). The high-energy ionization cross section (in cm^2) is given by:

$$\sigma(\varepsilon) = 5.94 * 10^{-20} \frac{\gamma^2}{\gamma^2 - 1} [8.68 + log(\gamma^2 - 1) + \frac{1}{\gamma^2}] \tag{4.12}$$

where $\gamma = 1 + \varepsilon / mc^2$ is the usual relativistic factor. The ionization cross sections are shown in Figures 4.9 and 4.10.

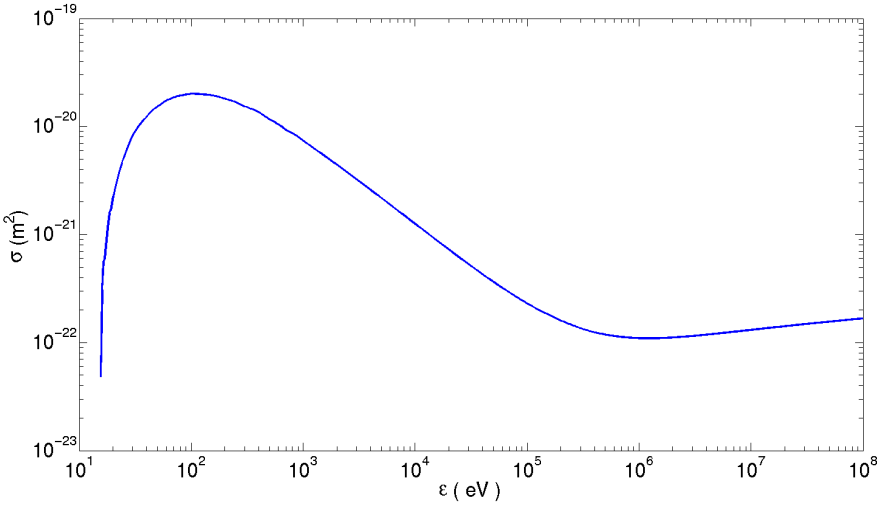

Figure 4.9: Ionization cross-sections for N_2 from BOLSIG+ package extended high energies using Murphy method.

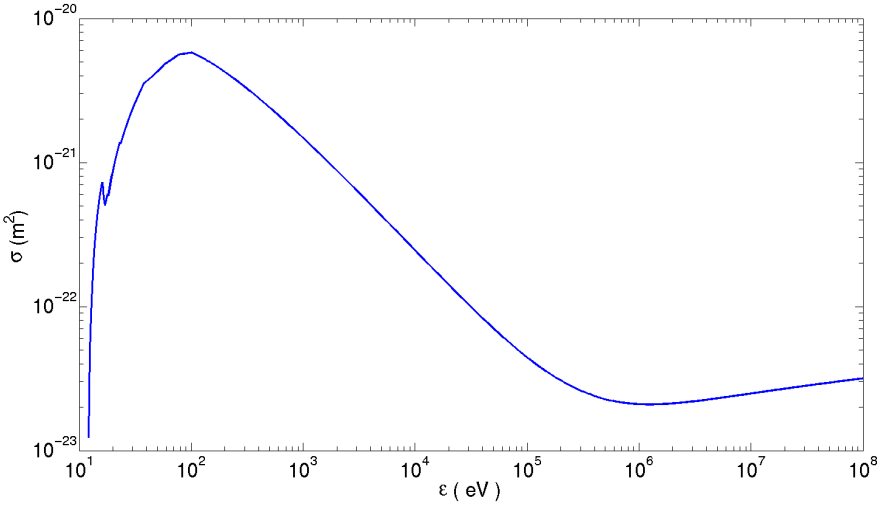

Figure 4.10: Ionization cross-sections for O_2 from BOLSIG+ package extended high energies using Murphy method.

During a ionization event, the energy of the incident electron is shared between

the ionization energy, ε^*, the extracted secondary electron, ε_s, and the remaining energy of the primary electron, ε':

$$\varepsilon' = \varepsilon - \varepsilon_s - \varepsilon^* \tag{4.13}$$

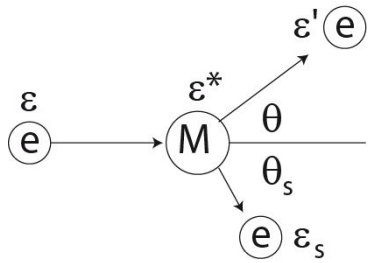

Figure 4.11: Ionization collision of an electron with a molecule.

The energy partitioning in ionization collisions has been described in various approximations, for instance that ε'=0, ε'=ε, or ε' is randomly distributed in the interval [0, $\varepsilon/2$] (Moss et al., 2006). In a physically more meaningful approach, experimental secondary electron energy distributions are fitted (Opal et al., 1971; Moss et al., 2006) as:

$$\frac{d\sigma(\varepsilon, \varepsilon_s)}{d\varepsilon_s} = \frac{\sigma_i(\varepsilon)}{\overline{\varepsilon}\ \mathrm{atan}[(\varepsilon - \varepsilon^*)/(2\overline{\varepsilon})]} \frac{1}{1 + (\varepsilon_s/\overline{\varepsilon})^2} \tag{4.14}$$

where $\overline{\varepsilon}$ is a shape parameter adjusted to fit the electron spectrum. The total ionization cross section is found by integrating over the secondary electron energy. The Opal cross section is used in the model of Chanrion and Neubert (2008; 2010).

Although the differential cross section from Opal et al. (1971) explains well the sharing energies in ionizing collisions, it is limited to incident electron energies <2 keV. Electrons with higher energies can penetrate the inner shells of the nucleus, requiring a different approach. In this high-energy range, Møller scattering is a better description (Berestetskii et al., 1982; Dwyer and Babich, 2011):

$$\frac{d\sigma_M(\varepsilon,\varepsilon_s)}{d\varepsilon_s} = \frac{2\pi r_e^2 mc^2}{\beta^2} \quad \left[\frac{(\gamma-1)^2 m^2 c^4}{\varepsilon_s^2(mc^2(\gamma-1)-\varepsilon_s)^2} - \frac{(2\gamma^2+2\gamma-1)}{\varepsilon_s(mc^2(\gamma-1)-\varepsilon_s)\gamma^2} + \frac{1}{m^2c^4\gamma^2}\right] \tag{4.15}$$

This formula for the cross section is adopted by several authors studying TGFs (Celestin and Pasko, 2010), (Dwyer and Babich, 2011). However, there is no simple consistent way to create a seamless overlap between the energy ranges described by the Opal and the Møller cross sections.

An alternative approach that covers both low and high electron energies is given in Kim et al. (2000), where the so-called relativistic binary-encounter-Bethe cross-section (RBEB) is introduced. The RBEB cross section is a combination of a non-relativistic Bethe cross section and the Møller cross section:

$$\sigma_R(\varepsilon) = \frac{4\pi a_o^2 \alpha^4 N}{(\beta_t^2+\beta_u^2+\beta_b^2)2b'}\left[\frac{1}{2}\left(\ln(\frac{\beta_t^2}{1-\beta_t^2}) - \beta_t^2 - \ln(2b^{'})\right)(1-\frac{1}{t^2}) + 1 - \frac{1}{t} - \frac{\ln t}{t+1}\frac{1+2t^{'}}{(1+t'/2)^2} + \frac{b^{'2}}{(1+t'/2)^2}\frac{t-1}{2}\right] \tag{4.16}$$

In this notation, N is the orbital electron occupation number, a_o is the Bohr radius, and α is the fine structure constant.

The energies are normalized by the binding energy, B, and the kinetic energy of the target electron,U, as:

$$\begin{aligned} t' &= \varepsilon/mc^2; t = \varepsilon/B \\ b' &= B/mc^2 \\ u' &= U/mc^2; u = U/B \end{aligned} \tag{4.17}$$

and the associated velocities:

$$
\begin{aligned}
v_t &= 2\sqrt{\varepsilon/m}; \beta_t = v_t/c; \beta_t^2 = 1 - \frac{1}{(1+t')^2} \\
v_b &= 2\sqrt{B/m}; \beta_b = v_b/c; \beta_b^2 = 1 - \frac{1}{(1+b')^2} \\
v_u &= 2\sqrt{U/m}; \beta_u = v_u/c; \beta_u^2 = 1 - \frac{1}{(1+u')^2}
\end{aligned}
\tag{4.18}
$$

The molecular orbital occupation number is:

N_2:

$$
\begin{aligned}
2\sigma_g &=> N = 2 \\
2\sigma_u &=> N = 2 \\
1\pi_u &=> N = 4 \\
3\sigma_g &=> N = 2
\end{aligned}
\tag{4.19}
$$

O_2 :

$$
\begin{aligned}
2\sigma_g &=> N = 2 \\
2\sigma_u &=> N = 2 \\
1\pi_u &=> N = 4 \\
3\sigma_g &=> N = 2 \\
1\pi_g &=> N = 2
\end{aligned}
\tag{4.20}
$$

Values of N, B, U are given in

(http://physics.nist.gov/PhysRefData/Ionization/molTable.html).

The RBEB cross sections were used by Celestin and Pasko (2010) for simulation of runaway electron avalanches and are also the chosen formulation in our model. More precisely, we use the energy sharing of the differential cross section but normalize it to the total cross section described earlier.

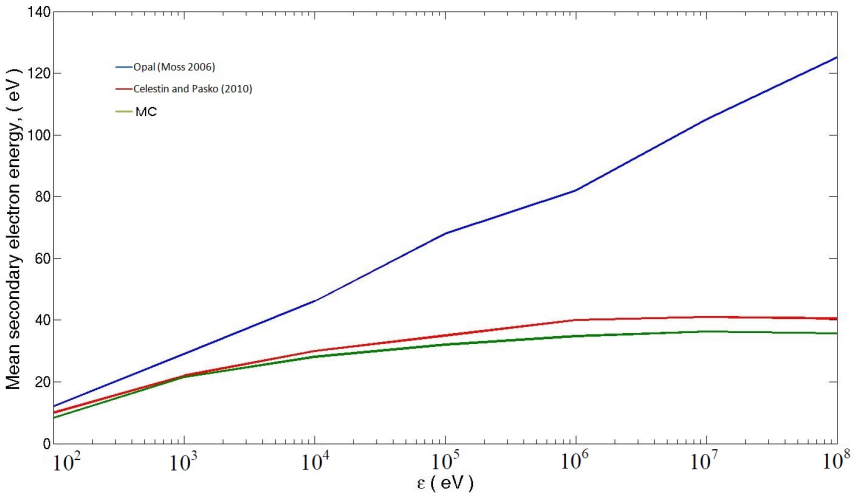

Figure 4.12: Mean secondary electron energy as a function of incident electron energy from the methods of Opal and RBEB.

The different formulations of the cross sections are exemplified in Figures 4.12 - 4.13. Figure 4.12 shows the mean energy of the secondary electrons as a function of the energy of the incident electron. It is clear that the Opal formulation overestimates the secondary electron energy and that the RBEB formulations give similar results. It is expected that the Opal cross section is not accurate above 2 keV, however, in the past it has often been used in codes where the upper energy limit has been stretched to well above this energy (Moss et al., 2006; Chanrion and Neubert, 2008; 2010). The implication is that the energy loss of an incident electron undergoing an ionizing collision is overestimated with Opal, and that the frictional force on the incident electron (Figure 2.1) therefore is increased. The problem increases with energy as the error increases with energy. The Figure 4.12 also shows that our implementation of the high-energy cross sections are consistent with the work of others (Celestin and Pasko, 2010)

A different view is shown in Figure 4.13 where we give the probability of ε' as a function of ε. We see that the Opal method overestimates the secondary electron energy. In addition, the Opal method overestimates the probability that an electron will be born in the runaway regime. We have tested the implementation of the improved cross sections carefully in this respect for the high-energy range of ε' in order to be sure that we are neither under- nor overestimating the probability of secondary electrons with high energies.

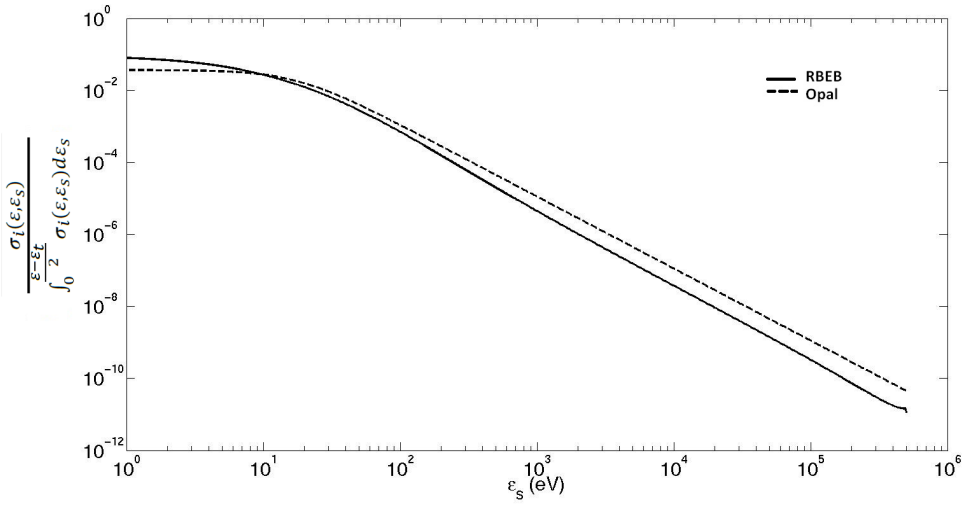

Figure 4.13: Probability distribution function of secondary electron energy as a function of the incident electron energy.

We conclude that Figures 4.12 - 4.13 underscore the importance not to rely on the Opal cross sections already in the code of Chanrion and Neubert (2008) when considering high-energy electrons, but to extend their code with proper consideration of the high-energy cross sections.

4.5 Bremsstrahlung

4.5.1 Introduction

Electrons continually undergo acceleration and deceleration in an electrified plasma. Electrons accelerated in Coulomb interactions with molecules emit bremsstrahlung, or literally "braking radiation", which results in a change in the direction of the electron and the emission of a photon. For electron energies below some hundreds of electron volts, bremsstrahlung is small and can neglected. At higher energies bremsstrahlung becomes significant and is the dominating interaction at energies $\sim>$ 1000 MeV. Being associated with high incident electron energies, bremsstrahlung is usually occurs in the X-ray (100 eV - 100 keV) and Gamma-ray ($>$ 100 keV) bands. The energies of the interaction are conserved as:

$$\varepsilon' = \varepsilon - \varepsilon_{ph} \tag{4.21}$$

where $\varepsilon_{ph} = h\nu$ is the energy of the photon.

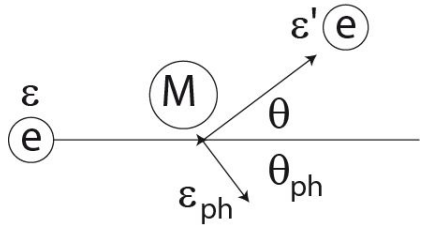

Figure 4.14: Bremsstrahlung emission and associated energies and angles.

Early studies of bremsstrahlung were concerned with the interaction of incident electrons with a target atomic nucleus. Bethe-Heitler (1934) introduced cross sections with arbitrary screening of the nucleus by the shell electrons, but their empirical expression is only valid when the kinetic energy of the incident electron before and after the photon emission is much larger than $m_o c^2$, where m_o is the electron rest mass (Salvat et al., 2006). Kirkpatrick and Wiedmann (1945) introduced a parametrization of non-relativistic bremsstrahlung cross sections in photon angle and energy based on the work on Coulomb fields by Sommerfeld (1931). Later, cross sections were obtained and tabulated from the Born approximation in the review of Koch and Motz (1959). The studies were continued with bremsstrahlung cross sections using relativistic, partial-wave methods by Tseng and Pratt (1971).

Haug (1975) was the first to study bremsstrahlung for incident electrons interacting with electrons, accounting for the recoil of the target electron and the exchange of energy. This interaction is relevant when one considers the effects not only of a partially screen nucleus, but also the electrons in the shells.

Pratt et al., (1977) gave numerical tables for bremsstrahlung cross sections for selected values of the atomic number Z and ε_{ph} for ε 1 keV - 2 MeV, based on the relativistic, partial-wave methods of Tseng and Pratt (1971). Kissel et al. (1983) extended their work with a tabular shape function that describes the probability of the photon emission angle, θ_{ph}, for 144 benchmark cases.

Seltzer and Berger (1985) gave a comprehensive set of bremsstrahlung cross sections that are differential in the emitted photon energy for electron energies

from 1 keV to 10 GeV and with atomic numbers of the target atoms $Z = 1$ - 100. These cross sections are a combination of the electron - nucleus and electron - electron fields. For energies below 2 MeV their electron-nucleus cross sections are based on Pratt et al., (1977) who used a numerical partial-wave method. For energies above 50 MeV, their electron - nucleus cross sections are based on the analytical theory of Davies et al. (1954). The transition energy range from 2 - 50 MeV, where there are no convenient studies, they used numerical interpolation between the low- and high energy cross sections. This approach brings uncertainties about 5-10 % in that energy region (Seltzer and Berger, 1986). For the electron - electron bremsstrahlung they used Haug (1975), mentioned above.

4.5.2 Implementation in the MC model

The bremsstrahlung process in our model is based on the work on Seltzer and Berger. We describe the emission energy of photons, ε_{ph}, and their emission angle relative to the incoming electron, θ_{ph}. The angle of the scattered electron, θ is treated the same way as for the other cross sections and is described later. It implies that momentum is conserved by assuming that the molecule changes momentum accordingly.

The differential cross section can be expressed as:

$$\frac{d\sigma_{br}(\varepsilon, \varepsilon_{ph})}{d\varepsilon_{ph}} = \frac{d\sigma_{nu}(\varepsilon, \varepsilon_{ph})}{d\varepsilon_{ph}} + Z\frac{d\sigma_{el}(\varepsilon, \varepsilon_{ph})}{d\varepsilon_{ph}} \tag{4.22}$$

where $d\sigma_{nu}/d\varepsilon_{ph}$ is the bremsstrahlung in the atomic nuclei and $Zd\sigma_{el}/d\varepsilon_{ph}$ is the bremsstrahlung in the Z atomic electrons. The scaled cross section in an energy-weighted form is tabulated by Seltzer and Berger as:

$$\chi(Z, \varepsilon, \kappa) = (\beta^2/Z^2)\varepsilon_{ph}\frac{d\sigma_{br}}{d\varepsilon_{ph}} = (\beta^2/Z^2)\kappa\frac{d\sigma_{br}}{d\kappa} \tag{4.23}$$

which depends on the energy of the incident electron, ε, and on the reduced photon energy $\kappa = \varepsilon_{ph}/\varepsilon$ for a given element of atomic number Z. β is the velocity of the projectile in units of the speed of light c. It can be expressed directly by the energy of the electron:

$$\beta = \left(\frac{\varepsilon(\varepsilon + 2mc^2)}{(\varepsilon + mc^2)^2} \right)^{1/2} \tag{4.24}$$

In the model, we have extended the MC code to include the bremsstrahlung process using the scaled differential cross sections (DCS) from Seltzer and Berger (1986) in order to derive total cross section giving the probability for an electron to collide and the differential one giving the distribution in photon energy. The distribution in photon scattering angle come from the work of Acosta et al. (2002). The implementation will be described in the following sections.

4.5.3 The total cross sections

We use the differential cross sections of energy transfer (DCS) from Seltzer and Berger (1986) which are given on tabular form as $(\kappa\sigma)_{br}(\varepsilon_j, \kappa_i)$ for j=57 incident electron energies, each with i=30 reduced photon energies. The implementation in the MC code requires cross section data for intermediate energies as well as the total cross sections, e.g. the DCS integrated in photon energy. We consider two approaches. In the first, the mid-point approach, we assume that $\sigma_{br}(\varepsilon, \kappa)$ is constant in a photon energy interval, $d\kappa$, and is defined by the average over the interval of the DCS, $\overline{\kappa\sigma_{br}}$ divided by average energy, $\overline{\kappa}$. In this approach, the energy intervals and DCS values corresponding to the DCS tables are determined as:

$$\begin{aligned} \overline{\kappa}^{i+1/2} &= (\kappa^i + \kappa^{i+1})/2 \\ \overline{\kappa\sigma}_{br}^{i+1/2} &= ((\kappa\sigma)_{br}^{i} + (\kappa\sigma)_{br}^{i+1})/2 \\ d\kappa^{1+1/2} &= \kappa^{i+1} - \kappa^i \end{aligned} \tag{4.25}$$

In the other approach, we interpolate linearly between the values $(\kappa\sigma)_{br}(\varepsilon_j, \kappa_i)$ given in the tables, and divide by κ.

The results of the two methods are shown on Figure 4.15 for ε=1 keV. The mid-point method is the staircase curve and the interpolation method is the smooth curve. In both cases, the total cross section is then found by integrating over the photon energy.

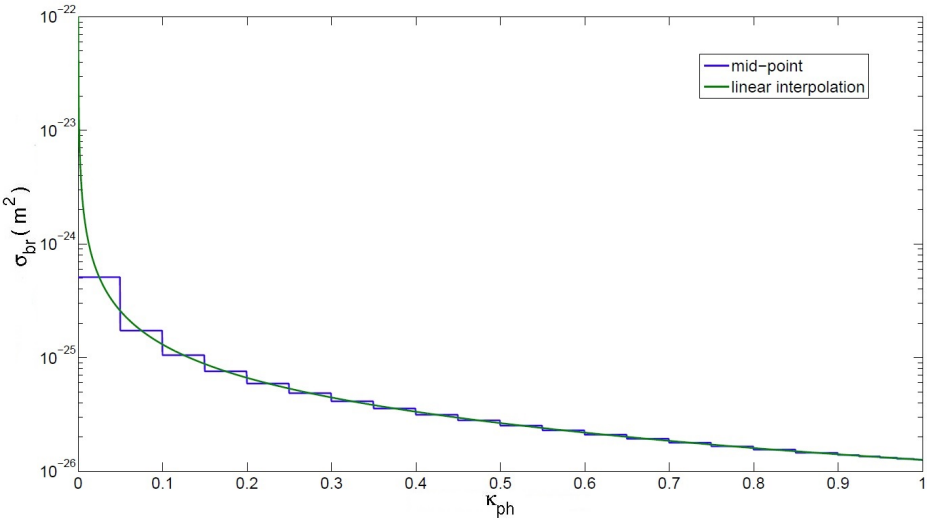

Figure 4.15: Comparison of the bremsstrahlung differential cross section, $\sigma_{br}(\varepsilon, \kappa_{ph})$ for the mid-point and the interpolation methods, for electrons with ε=1 keV targeting N_2.

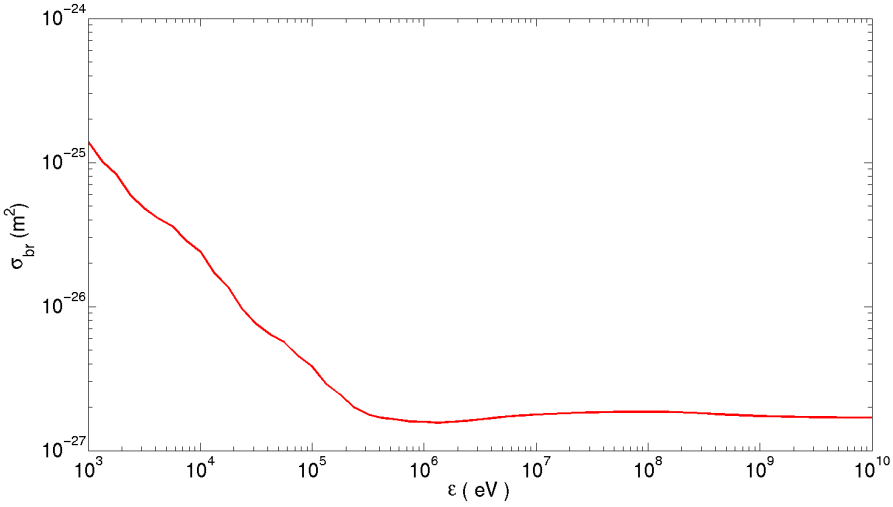

Figure 4.16: Total bremsstrahlung cross sections for N_2 as a function of incident electron energy, constructed from (Seltzer and Berger, 1986).

From the figure 4.15 we see that the problem with the mid-point method is that, in the lower energy range, photon emissions are underestimated more in the first half of an interval than they are overestimated in the last half of the interval. The interpolation method is therefore chosen in our model.

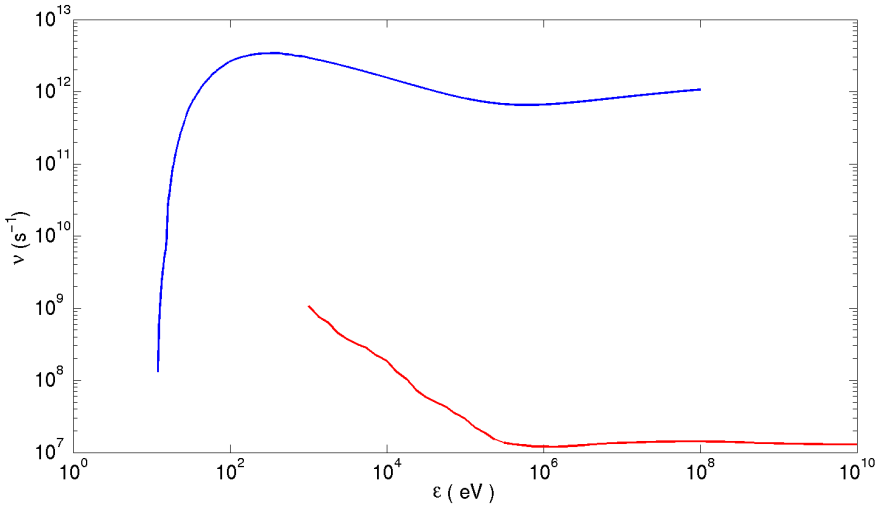

Figure 4.17: Comparison of collision frequencies related to bremsstrahlung emission (red) and ionization (blue) in air.

Since the interpolation method includes a division with κ it goes to infinity as κ approaches 0. To avoid this non-physical divergence we have applied a lower cut-off energy for the reduced photon energy at 10^{-4}. As an example, the total bremsstrahlung cross section estimated with this method for N_2 is shown in Fig. 4.16.

Cross sections can be related to collision frequencies through $\nu = n_n v \sigma$ where ν is the collision frequency, v is the electron velocity and σ a cross section for interaction. In Figure 4.17 we compare the collision frequencies relating to bremsstrahlung and ionization in air. We see that the bremsstrahlung interactions more infrequent than ionization interactions by several orders of magnitude. However, the energy exchange per interaction is much larger for bremsstrahlung. This can be seen from a reconstruction of the frictional force shown in Figure 4.18.

We further compared our cross sections with those given in Carlson (2009). They are taken from the International Commission on Radiation Unit and Measure-

ments (1984). The dashed line is from a formula of Bethe-Bloch. There are not many details so we have limited our comparison to a visual one where we plot our cross sections on the same scale Carlson. The result is shown in Figure 4.19. We conclude from the figure that the two approaches give similar results which gives us confidence in our implementation.

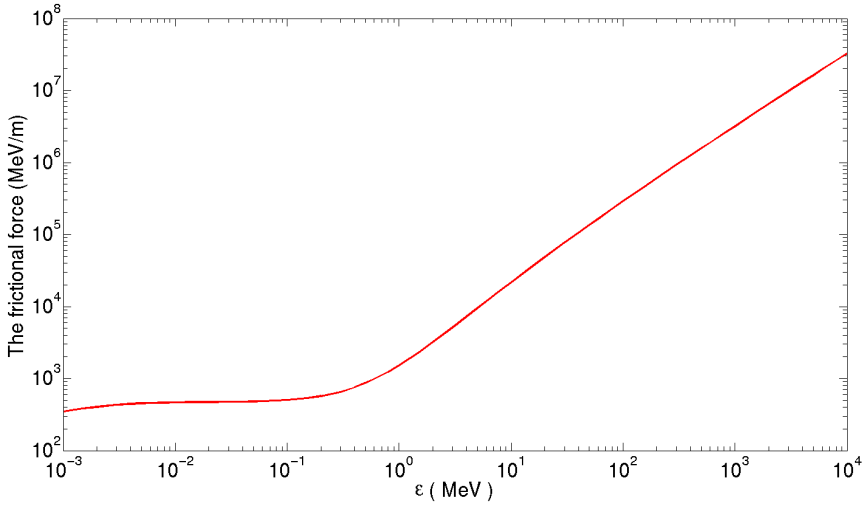

Figure 4.18: The frictional force in air from the bremsstrahlung process.

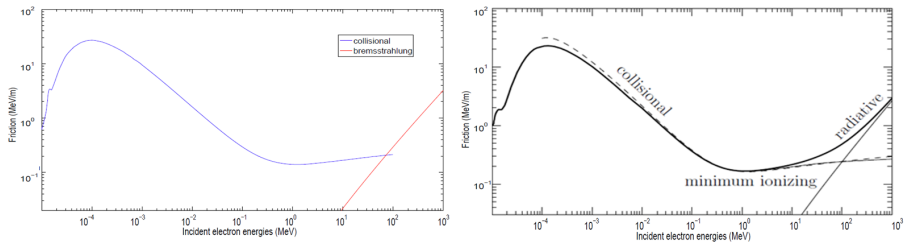

Figure 4.19: Comparison our frictional force in our code (left) with Carlson (2009) (right).

4.5.4 The differential cross sections

We now return to the differential cross sections which are also needed in our model. They are obtained by the interpolation method described in the previous

subsection. Figure 4.20 shows $\sigma_{br}(\varepsilon, \kappa)$ in air for 4 values of ε.

4.5.5 Emission angle of photons

The angle the photons are emitted, θ_{ph}, is expressed by double differential cross section (in angle and photon energy):

$$\begin{aligned} \frac{d^2\sigma_{br}}{d\varepsilon_{ph} d(cos\theta_{ph})} &= \frac{d\sigma_{br}}{d\varepsilon_{ph}} p(Z, \varepsilon, \varepsilon_{ph}, cos\theta_{ph}) \\ &= \frac{Z^2}{\varepsilon_{ph}\beta^2} \chi(Z, \varepsilon, \varepsilon_{ph}) p(Z, \varepsilon, \varepsilon_{ph}, cos\theta_{ph}) \end{aligned} \tag{4.26}$$

where $p(Z, \varepsilon, \varepsilon_{ph}, cos\theta_{ph})$ is the probability distribution function of $cos\theta_{ph}$.

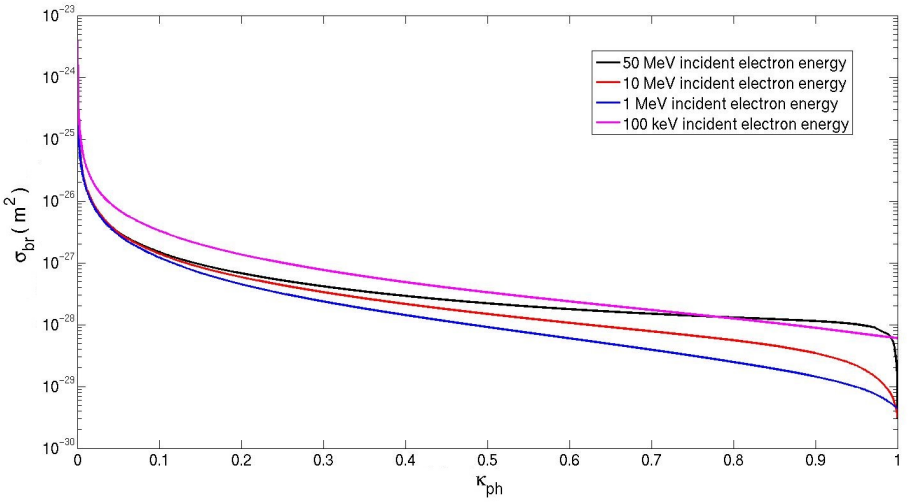

Figure 4.20: The bremsstrahlung differential cross section in air for different incident electron energies.

One way of estimating the probability of a photon emission angle is to integrate triple bremsstrahlung cross-sections given in literature (Koch and Motz, 1959). However, this is difficult to implement and test. The path we have chosen is instead to use a probability function of the emission angle. It is more convenient

and allow to use the single differential cross sections of Seltzer and Berger which cover the complete energy range. The probability function is:

$$p(Z, \varepsilon, \kappa, cos\theta_{br}) \tag{4.27}$$

Kissel et al. (1983) tabulated probability functions for ε= 1 - 500 keV with atomic number between 1 - 92 in terms of Legendre polynomials. Although the Kissel tables have a good accuracy, we need energies above 500 keV. Furthermore, they are hard to implement in a MC code.

Instead we follow Acosta et al., (2002) who considers a reference frame, K, at rest with respect to the laboratory, and a coaxial reference frame, K', that moves with the electron. In K', the angular distribution of the emitted photons in a dipole approximation is:

$$p(cos\theta'_{br}) = A * \frac{3}{8}(1 + cos^2\theta'_{br}) + (1 - A) * \frac{4}{3}(1 - cos^2\theta'_{br}) \tag{4.28}$$

where A ($0 \leq A \leq 1$) and B are adjustable parameters obtained by least square fitting (Acosta 2002). The direction of emission angle in the frame K is obtained by means of the Lorentz transformation

$$cos\theta_{br} = \frac{cos\theta'_{br} + \beta}{1 + \beta cos\theta'_{br}} \tag{4.29}$$

Thus, the angular distribution in K is given by:

$$\begin{aligned} p(cos\theta_{br}) \quad &= \frac{3A}{8}\left[1 + (\frac{cos\theta_{br} - \beta'}{1 - \beta' cos\theta_{br}})^2\right] \frac{1 - \beta'^2}{(1 - \beta' cos\theta_{br})^2} \\ &+ (1 - A)\frac{4}{3}\left[1 - (\frac{cos\theta_{br} - \beta'}{1 - \beta' cos\theta_{br}})^2\right] \frac{1 - \beta'^2}{(1 - \beta' cos\theta_{br})^2} \end{aligned} \tag{4.30}$$

where $\beta' = \beta(1 + B)$. This analytical expression is parallel to the approach by Jackson (1975) and is straightforward to implement into our MC model. This expression also agrees well with the shape functions of Kissel et al. (1983) and

the angular distributions obtained from high-energy theory (Heitler, 1954; Koch and Motz, 1959; Salvat et al., 2006). We implemented the analytical expression from Acosta et al. (2002) and show it in a polar plot for N_2 for two incident electron energies in Figure 4.21. From the figure 4.21 we see that the radiation becomes more forward directed with increasing incident electron energy.

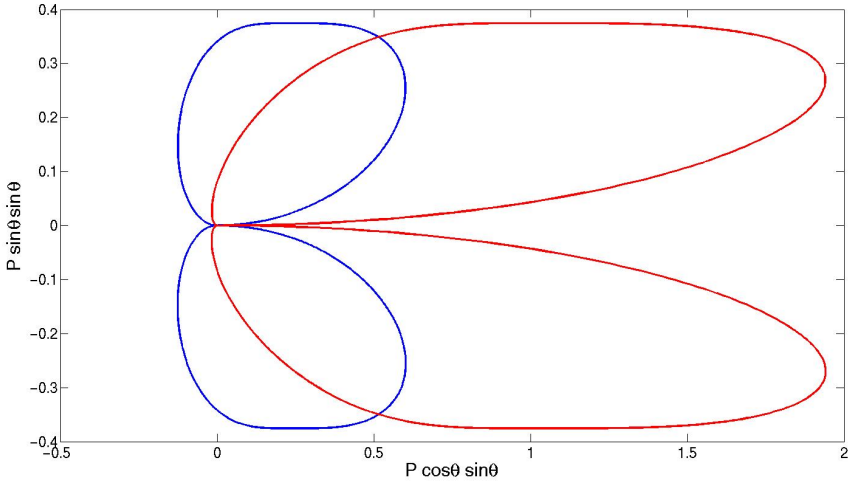

Figure 4.21: Probability function for bremsstrahlung emissions from electrons interacting with N_2 . The electron energies are 0.1 MeV (blue) and 1 MeV (red).

We have compared angular distribution of emitted photons from Acosta et al., (2002) with another analytical angular distributions used by (Rees, 1964), which base cross sections on Sauter.

$$f(\theta_{br}) = \frac{sin^2\theta_{br}}{(1-\beta cos\theta_{br})^4} \tag{4.31}$$

The function is not normalized. It is an approximation to the formulas that we have adopted (eq. 4.30) with appropiate A and B values omitting a factor $(1-\beta^2)^2$. The approximation is for the lower energy range of ε. In Figures 4.22 - 4.25 we compare the two methods for ε = 1, 10, 100, and 500 keV.

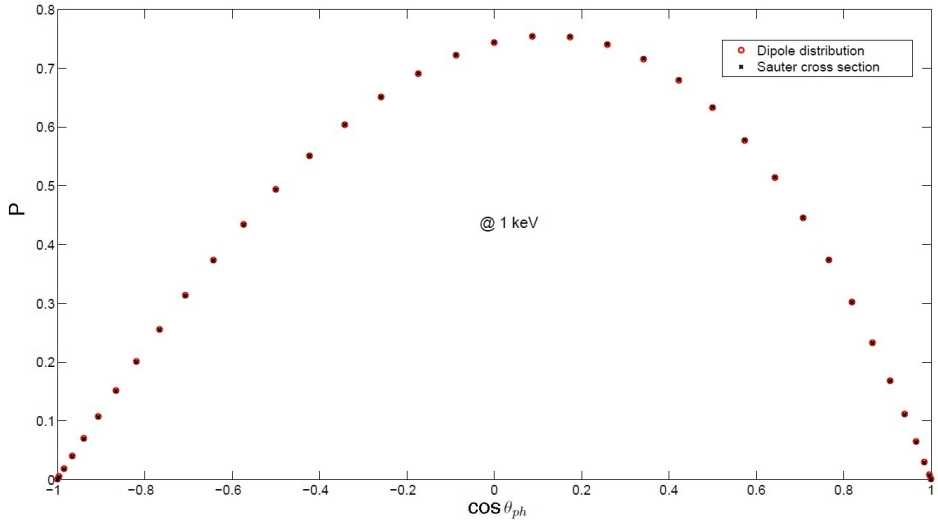

Figure 4.22: Distribution of bremsstrahlung emission angles, θ_{ph}, for $\varepsilon = 1$ keV. Two methods are compared: the dipole method of Acosta et al. (2002) and the Sauter method of Rees (1964).

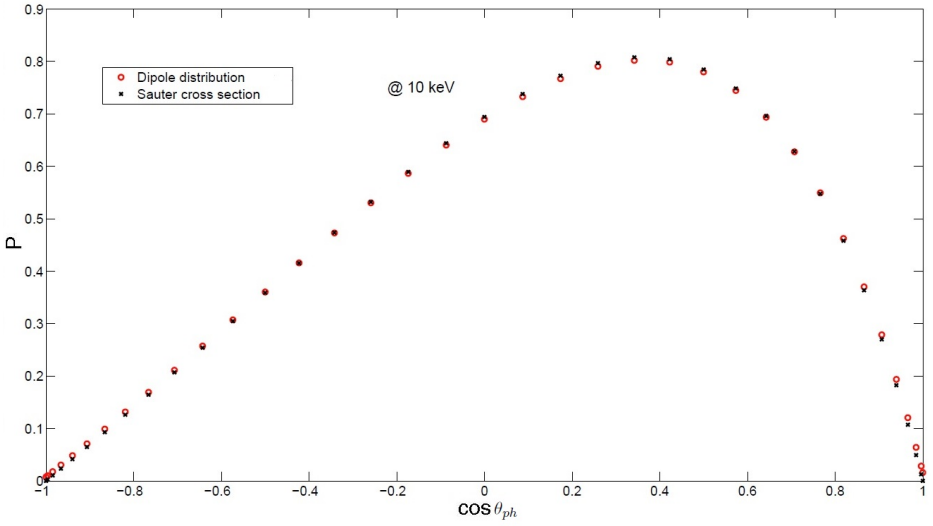

Figure 4.23: Distribution of bremsstrahlung emission angles, θ_{ph}, for $\varepsilon = 10$ keV. Two methods are compared: the dipole method of Acosta et al. (2002) and the Sauter method of Rees (1964).

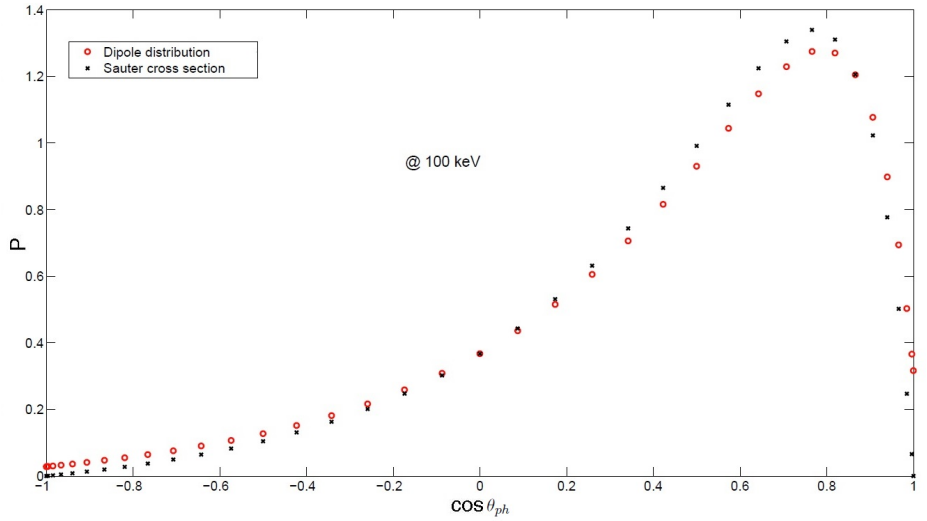

Figure 4.24: Distribution of bremsstrahlung emission angles, θ_{ph}, for $\varepsilon = 100$ keV. Two methods are compared: the dipole method of Acosta et al. (2002) and the Sauter method of Rees (1964).

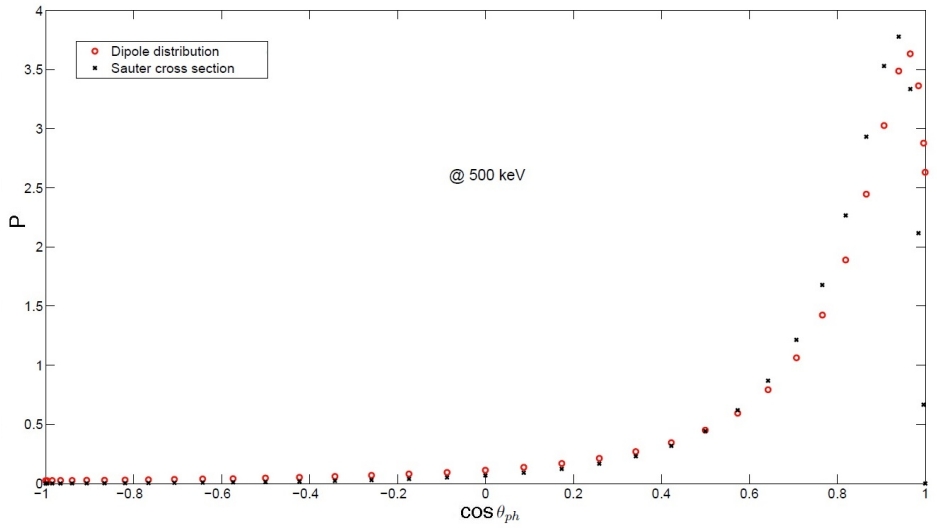

Figure 4.25: Distribution of bremsstrahlung emission angles, θ_{ph}, for $\varepsilon = 500$ keV. Two methods are compared: the dipole method of Acosta et al. (2002) and the Sauter method of Rees (1964).

We conclude that in the low-energy range, the angular probability function is implemented correctly. Likewise, the polar plots of the emission angles at 0.1 and 1 MeV, discussed earlier (Figure 4.21), appear reasonable getting in forward direction.

4.6 The electron scattering angle

In our code we have adopted the model of Okhrimovskyy et al., (2002) to describe the scattering angle, θ, of the incident electron after any type of collision, elastic or inelastic, and the secondary electron angle, θ_s, in the case of ionization. They are described by a common model that gives the probability I(ε, θ) for screened-Coulomb scattering of an electron by air molecules using a function, ξ, that fits to experimental data:

$$I(\varepsilon, \theta) = \frac{1}{4\pi} \frac{1 - \xi^2(\varepsilon)}{(1 - \xi(\varepsilon) cos\theta)^2} \tag{4.32}$$

where $\xi(\varepsilon)$ is:

$$\xi(\varepsilon) = \frac{0.065\varepsilon + 0.26\sqrt{\varepsilon}}{1 + 0.05\varepsilon + 0.2\sqrt{\varepsilon}} - \frac{12\sqrt{\varepsilon}}{1 + 40\sqrt{\varepsilon}} \tag{4.33}$$

where ε is in units of eV. The function $\xi(\varepsilon)$ is shown on Figure 4.26.

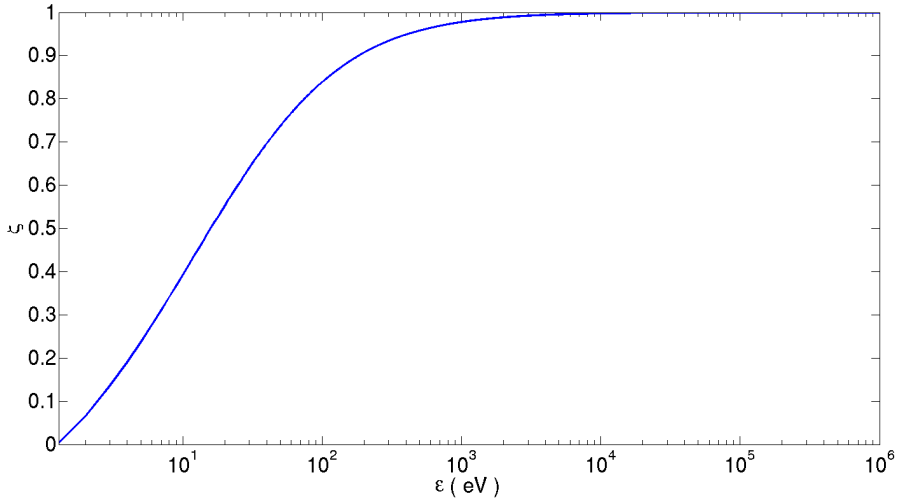

Figure 4.26: The function $\xi(\varepsilon)$.

4.7 Implementation of scattering probabilities in the MC code

In this section we briefly describe how the scattering processes are implemented via random number calls in the MC code.

4.7.1 The scattering angle

The probability of the scattering angle is found using a random number, R, uniformly distributed in the interval (0,1) (Okhrimovskyy et al., 2002):

$$cos\theta = 1 - \frac{2R(1-\xi)}{1+\xi(1-2R)} \tag{4.34}$$

The scattering becomes isotropic as $\xi \to 0$ for energies approaching 1 eV:

$$cos\theta \rightarrow 1 - 2R \tag{4.35}$$

Conversely, for high energies where $\xi \rightarrow 1$, the electron scatters in the forward direction:

$$cos\theta \rightarrow 1 \tag{4.36}$$

4.7.2 Ionization

The secondary electron energy, ε_s, is related to a uniform random number through the cumulative distribution function:

$$R = \frac{\int_0^{\varepsilon_s} \sigma(\varepsilon, \varepsilon_s) d\varepsilon_s}{\int_0^{(\varepsilon - \varepsilon_{thr})/2} \sigma(\varepsilon, \varepsilon_s) d\varepsilon_s} \tag{4.37}$$

where ε_s is limited in energy to half of the incoming electron energy - with the ionization threshold energy, ε_{thr}, subtracted (the electron with the lowest energy is always considered the secondary electron). A two-dimensional look-up table of the reverse function (R^{-1}), i.e. the function giving ε_s from random number between 0-1. This function depends on ε and is calculated once and for all to save computer time. The energy intervals of the table is smaller in the high-energy end in order to get better accuracy.

4.7.3 Bremsstrahlung

The bremsstrahlung energy and angle are determined using the same principle as described for the energy of a secondary electron, using the appropriate probability functions.

4.8 Some MC code validation cases

In the following we show a subset of the many validation runs that have been undertaken to test the implementation of the various cross sections in the MC code.

4.8.1 Test of angular scattering

We conducted a qualitative test of the angular scattering of electrons undergoing elastic collisions. At t=0, we ran simulations for 10.000 electrons in air at ground pressure, forcing each to scatter once. The initial electron energy was 5 eV in one case and 5 keV in the other, with the complete kinetic energy in the velocity component along the z-direction. The expectation was that the low-energy electrons scatter omni directionally and the higher energy electrons scatter predominantly in the forward direction. The results are shown in Figures 4.27 and 4.28.

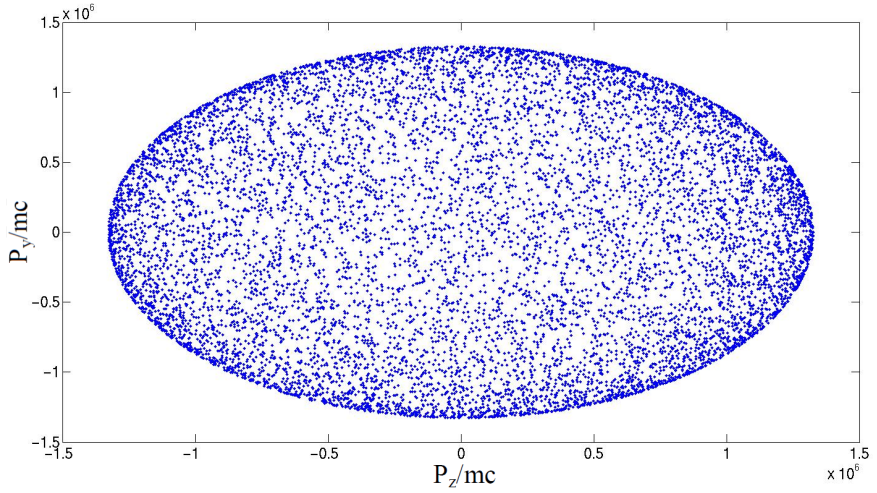

Figure 4.27: Momentum distribution for 10.000 electrons in air at ground pressure. The initial conditions are $(p_x, p_y, p_z) = (0, 0, p_z^o)$ and energy = 5 eV. Each electron has undergone one elastic scattering.

The plots show the distribution in momentum-space of the electrons after they have scattered. Initially they are all located at $(p_x, p_y, p_z) = (0, 0, p_z^o)$, where

p_z^o is the momentum vector corresponding to the initial energy. The figures show clearly minor scattering in energy from elastic scattering and the expected energy-dependent scattering of the electron velocity angles, giving confidence in the implementation of the scattering scheme.

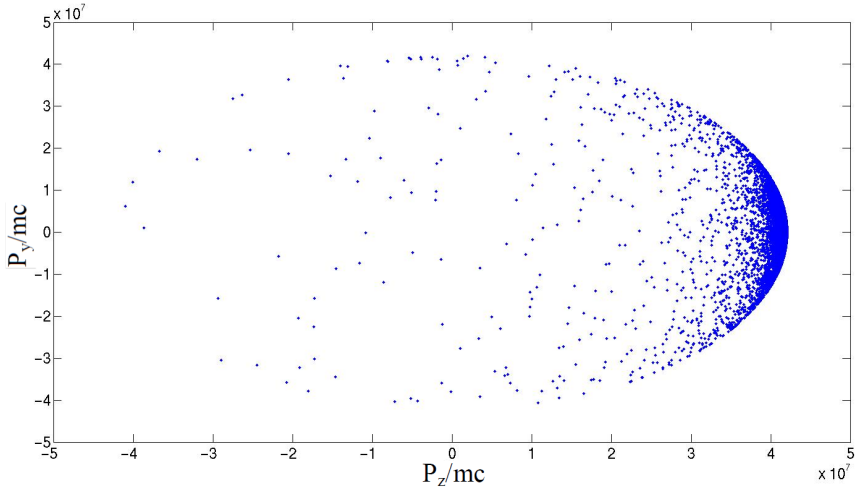

Figure 4.28: Momentum distribution for 10.000 electrons in air at ground pressure. The initial conditions are $(p_x, p_y, p_z) = (0, 0, p_z^o)$ and energy = 5 keV. Each electron has undergone one elastic scattering.

4.8.2 Test of inelastic collisions

Finally we show a test of inelastic collisions in air in Figure 4.29. 10000 electrons with 0 initial energy have been drifted for 100 time steps in a field of 2 E_k, enough for the distribution function in energy to approach a steady state.

The MC results are compared to BOLSIG+.

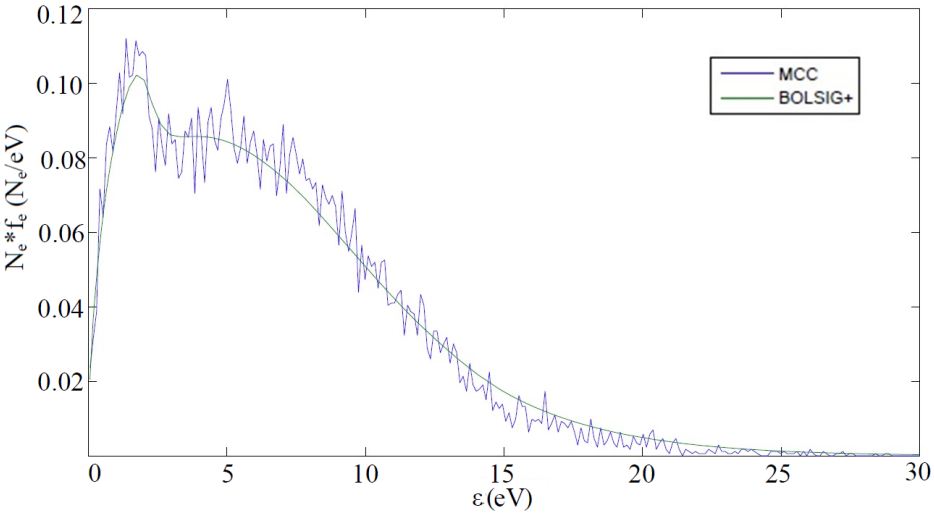

Figure 4.29: Electron energy distribution function ($N_e * f_e$) from simulations of electrons in air at ground pressure undergoing both elastic and inelastic collisions. MC-code (noisy) and numerical solution to analytical formulation (BOLSIG+).

The two shows a very nice agreement, again giving confidence in our implementation.

Chapter 5

Characterization of TGFs at their source

5.1 Introduction

In this chapter we explore how the initial conditions in a source region affect the properties of radiated bremsstrahlung. We consider a relativistic runaway discharge where seed electrons are accelerated in a constant electric field. We follow the acceleration of the electrons and the formation of secondary electrons arising from ionization of the neutral gas, and the emission of bremsstrahlung photons. In this chapter we discuss the electron and photon distributions in the source region, i.e. in the case of photons, before the influence of propagation effects such as scattering and absorption in the atmosphere. In the next chapter we estimate the bremsstrahlung properties at the top of the atmosphere at altitudes corresponding to the satellites that have observed TGFs.

5.2 The electron avalanche length and growth rate

A characteristic length is the so-called electron avalanche length, λ_r, which is the e-folding length describing the avalanche growth. The avalanche length has been estimated and formulated in different runaway breakdown studies. In 1992, Gurevich et al. considered the runaway electron mechanism of air breakdown and formulated the avalanche length as a function of electric field:

$$\lambda_r = \frac{10.8[\mathrm{MV}]}{E} \tag{5.1}$$

In the formula, E is inserted in MV/m. The formula is for ground level pressures.

Dwyer (2003; 2006) published results of Monte Carlo simulations of electrons initially with energies at 1 MeV in fields in between 0.3 - 2.5 MV/m and estimated another formula of the avalanche length:

$$\lambda_r = \frac{7200[\mathrm{kV}]}{E - 284[\mathrm{kV/m}]\mathrm{n}'_{\mathrm{n}}} \tag{5.2}$$

where n'_n is the density of air relative to STP. The electric field is in units of [kV/m]. The value, 284 kV/m is the threshold field at ground pressure estimated in the simulations. As the altitude increases, the threshold field decreases proportionally to n_n.

Celestin and Pasko (2010; 2012) also formulated the runaway avalanche length:

$$\lambda_r = 0.89c/(55E - 3 \times 10^7) \tag{5.3}$$

where E is in units of V/m. The factor $0.89c$ comes from a translation of their results from avalanche *time* rather than avalanche *length*. It was shown in (Coleman and Dwyer, 2006; Dwyer et al., 2012) that an avalanche develops with a velocity of $\sim 0.89c$.

These, and other studies, are shown in Figure 5.1 .

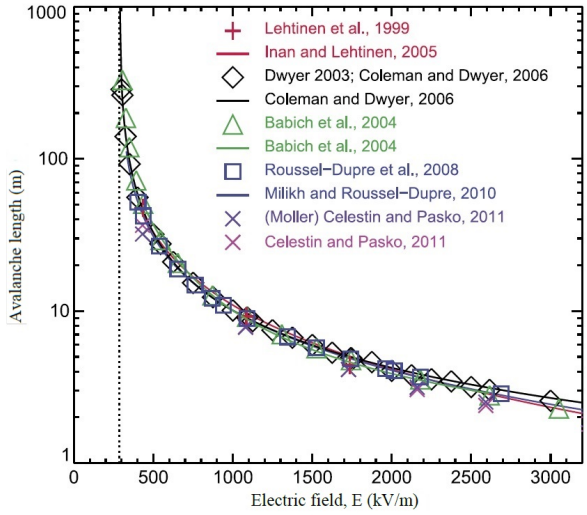

Figure 5.1: Comparison of avalanche lengths estimated from different approaches(Dwyer et al., 2012).

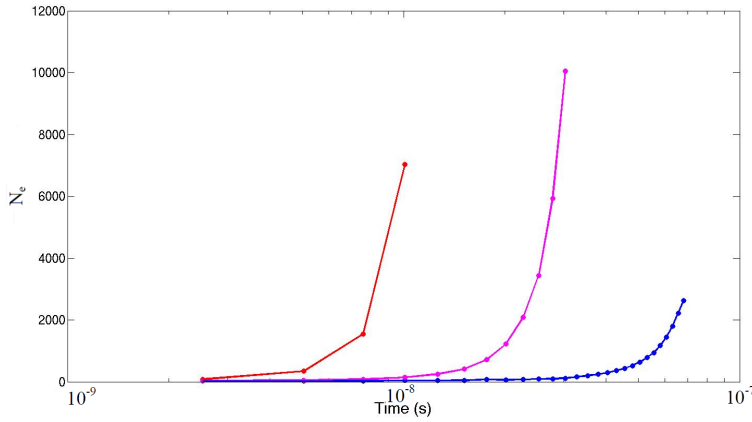

Figure 5.2: Number of electrons (N_e) as a function of time for E= 0.4 (blue), 0.8 (magenta), and 1.5 (red) E_k.

We conducted our own simulations of the avalanche properties by following initially 10 seed electrons at 1 MeV energy, in air at ground pressure and in fields between 0.4 and 10 E_k. The simulations were made keeping only the

electrons of energy above 1 keV. We conducted the runs for a time t sufficient for the normalized electron and photon energy distributions of the avalanche to reach steady state, except at the high-energy tail, where electrons and photons continue to reach higher energies with time. With normalized we mean division by the total number of electrons or photons.

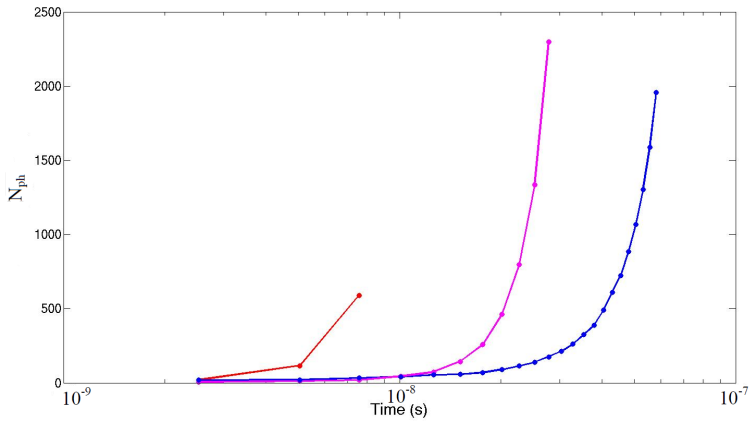

Figure 5.3: Number of photons (N_{ph}) as a function of time for E= 0.4 (blue), 0.8 (magenta), and 1.5 (red) E_k.

The number of electrons with energies in the runaway range N_e, and the number of emitted bremsstrahlung photons accumulated during the simulation, N_{ph}, are shown in Figures 5.2 and 5.3 as functions of time for E = 0.4 (blue), 0.8 (magenta), and 1.5 (red) E_k. The number of electrons or photons, N_r, can be fitted with an exponential function of the form:

$$N_r = N_o exp(-t/\tau_r) \tag{5.4}$$

For electrons we have:

$$\begin{aligned} &E = 0.4, 0.8, 1.5 E_k \\ &N_o = 10, 10, 10 \\ &\tau_r = 29, 10.8, 4.48 \times 10^{-9} [\mathrm{s}] \end{aligned} \tag{5.5}$$

For photons, best fit is:

$$\begin{aligned} E &= 0.4, 0.8, 1.5 E_k \\ N_o &= 13.45, 6.49, 0.37 \\ \tau_r &= 33.4, 11.7, 3.72 \times 10^{-9} [\mathrm{s}] \end{aligned} \tag{5.6}$$

We note that the growth rate of electrons and photons are of similar magnitude, for the different fields, as expected when the normalized electron distribution function has converged.

To compare with others, we estimate the runaway electron avalanche length (e-folding length), λ_r, via the equation (Dwyer, 2004):

$$N_r = N_o e^{\int_0^L \frac{dz}{\lambda_r(z)}} \tag{5.7}$$

where L is the total avalanche length. For uniform fields and neutral densities, the integral equals L/λ and the equation becomes:

$$N_r = N_o e^{L/\lambda_r} \tag{5.8}$$

We estimate avalanche lengths from our simulations using above equation (with an error +3 %). In Figure 5.4, we compare our avalanche lengths with those of other studies. We see that our results are in good agreement with past simulations studies, but less so with the theoretical formula of Gurevich et al., (1992). This figure is a good comparison to show how our implementation in line with other model simulations. The difference between our results and past simulation results comes from low energy electrons (below 1 keV electrons), which we do not simulate them in this project.

Having confidence in our estimates of the avalanche length, we extend the above results to the high-field limit which potentially could exist impulsively for very short times in a gas, as for instance in the tip of a leader channel as it jumps another step. We calculate the avalanche length up to 10 E_k which is where all electrons are in the runaway regime as defined from Figure 2.1. The results are shown in Figure 5.5. The data points are well fitted by an exponential:

$$\lambda_r = \lambda_o (E/E_k)^{-\alpha_\lambda} \tag{5.9}$$

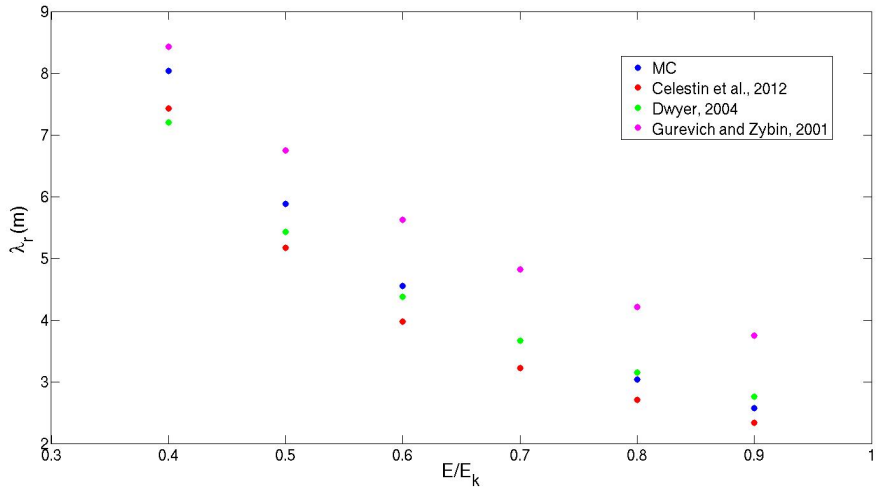

Figure 5.4: Comparison of λ_r with other studies.

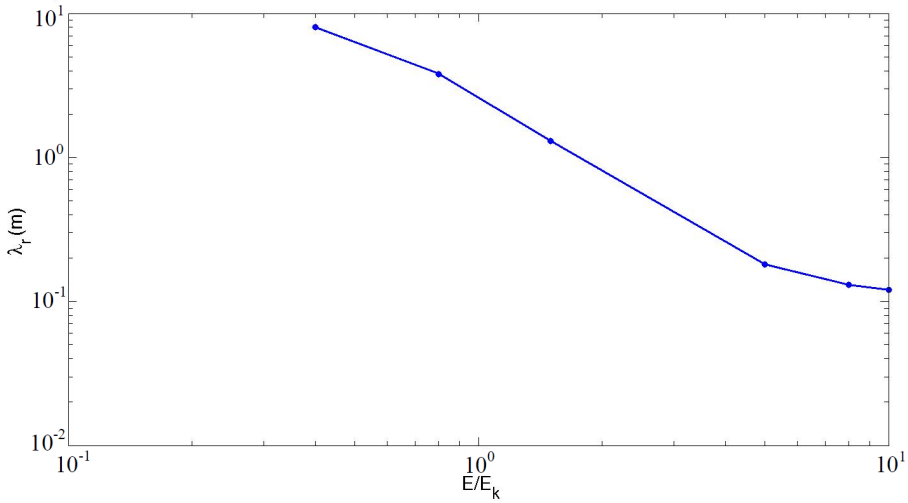

Figure 5.5: λ_r for strong fields.

The best fit is for:

$$\lambda_o = 2.22\text{m}; \alpha_\lambda = 1.40 \tag{5.10}$$

We see from the figure 5.5 that for strong fields, the avalanche length is down to a few tens of cm, approaching the scales of leader tip or may be even streamers. This is why they may play a role in the generation of TGFs or other X- and Gamma radiation observed in thunderstorms.

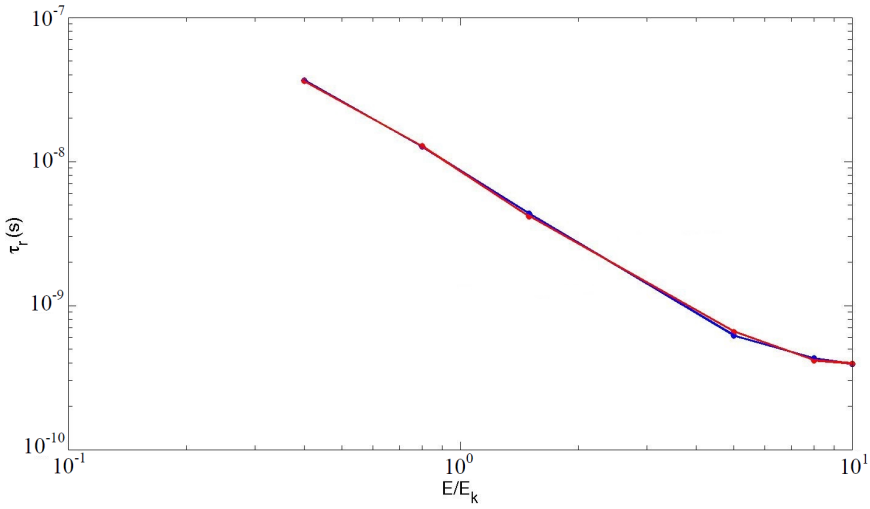

Figure 5.6: τ_r for electron and photons in strong fields.

The growth rate of runaway electrons and photons (τ_r) have also been estimated for the high field range. The results are shown in Figure 5.6. The data are fitted with:

$$\tau_r = \tau_o (E/E_k)^{\alpha_\tau} \tag{5.11}$$

The best fit for electrons is:

$$\tau_o = 8.81 \times 10^{-9}[\text{s}]; \alpha_\tau = -1.39 \tag{5.12}$$

The best fit for photons is:

$$\tau_o = 8.86 \times 10^{-9}[\mathrm{s}]; \alpha_\tau = -1.45 \tag{5.13}$$

As noted earlier, the relativistic electron- and photon growth rates are almost identical. However, in the case of electrons, only those with energies in the runaway regime are counted, whereas for photons, all photons are counted.

We next study how the ratio of photons to electrons depend on energy. This is done by binning both electrons and photons in energy and plotting their ratio (Alexander B. Skeltved, private communication). We use 10 seed electrons with 1 MeV initial energy and we run simulations for a time to reach 10000 - 12000 photon emissions. Simulations are done for different values of the electric field. The result is shown on Figure 5.7.

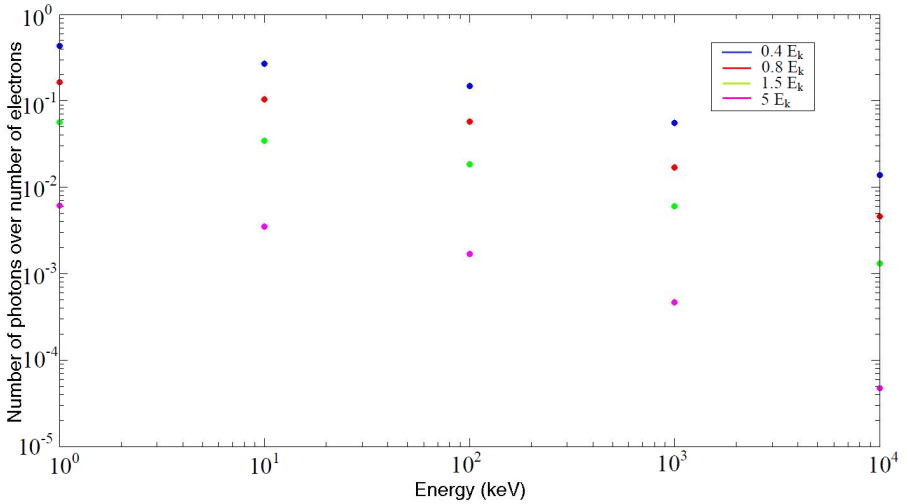

Figure 5.7: The ratio between number of photons over number of electrons for electric fields between 0.4 - 5.0 E_k.

We see that the efficiency of photon generation per runaway electron decreases with electron energy. This also influences the dependency on the electric field as the average runaway electron energy increases with electric field.

5.3 Energy spectra of electrons and of brems - strahlung photons in avalanches

The initial conditions of our simulations can, of course, be varied freely and independently on the actual physics of the runaway discharge. However, the exercise allows us, at least conceptually, to bracket the parameter range that characterize the TGF source when we in the next chapter compare simulated spectra at satellites with observed spectra.

The initial conditions of the electron avalanche that we vary are the number of seed electrons, their initial energy, the background electric field and the duration of the discharge.

A discharge will in general contain electrons of different energies, with the bulk of the electrons in the eV range and relatively few at keV-MeV energies. The high electric potential differences in streamers heads can boost the energetic electron population and these are thought to be accelerated further to several tens of MeV energies in the fields of lightning stepped leaders (Celestin and Pasko, 2011).

5.3.1 Avalanche electron spectrum for different energies of the seed electrons

We first consider the effect of the initial energy of the seed electrons. We assume that the discharge starts with 10 mono-energetic seed electrons at 0.1, 1, 10, 100 MeV, for instance produced by cosmic rays (Gurevich et al., 1992) or accelerated in a thermal discharge (Moss et al., 2006). The electrons are accelerated in an a constant electric field of 0.4 E_k, where E_k is the conventional breakdown field $\sim$ 3.2 MVm^{-1}. This is at the high end of observed large-scale thunderstorm fields, which are generally below 0.1 E_k as derived from balloon observations (Marshall et al., 2005), however, as an impulsive field, the magnitude is within range. The simulations are run for a time that allows the distribution functions to converge, except in the high energy tail which continues to grow with time.

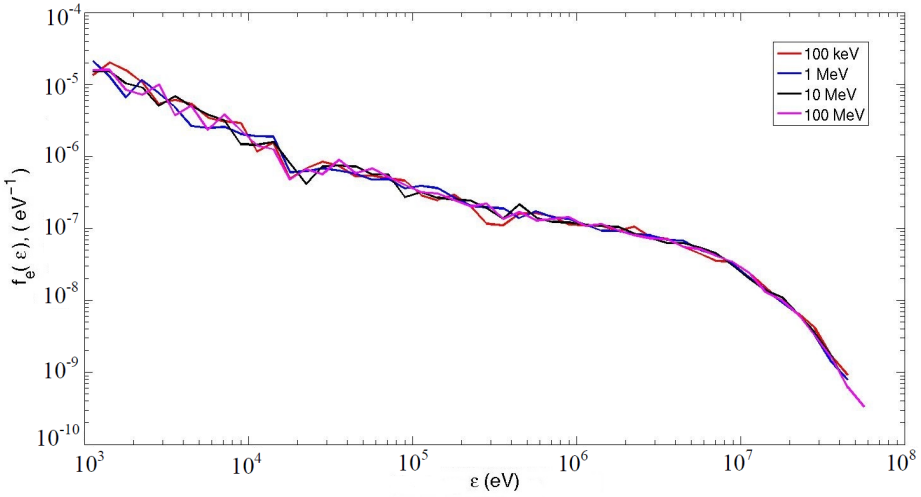

Figure 5.8: $f_e(\varepsilon)$ for different seed electron energies drifted at the electric field of 0.4 E_k for a time $t = 5.53\tau_r$ (203 ns).

The electron distribution as a function of electron energy, $f_e(\varepsilon)$, is shown on Figure 5.8 at $t = 203$ corresponding to 5.53 τ_r. Here, ε is the electron energy and f_e is the normalized distribution function. In the interval 1-10 MeV, $f_e(\varepsilon) \sim \varepsilon^{-1}$. Above $\sim$ 8 MeV, the spectrum falls off as few electrons are accelerated into this range. This will be discussed further later.

As expected, the normalized energy distribution function is insensitive to the initial seed electron energy because the secondary electrons in an avalanche, after a few e-folding times, will dominate the distribution.

5.3.2 Discussion of the electron spectrum

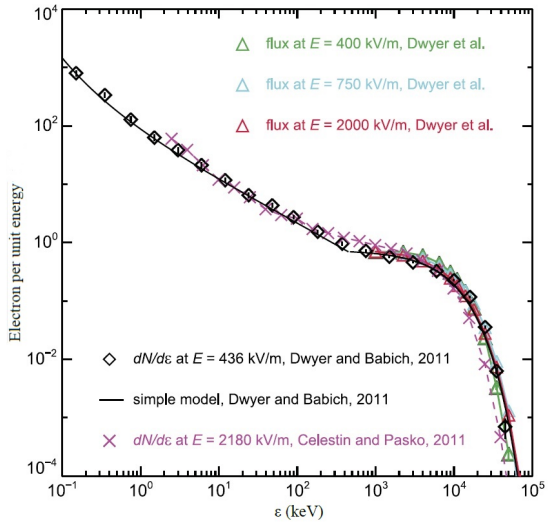

Figure 5.9: Electron energy spectrum produced by the RREAs. Both the number density per unit energy found at fixed time and the differential flux of runaway electrons passing through a fixed location are shown. The data points are all from Monte Carlo simulations. The solid curve is a simple analytical model. Above a few hundred keV, the solid curve is the exponential $e^{-\varepsilon/7.3MeV}$ spectrum for the runaway electrons (Dwyer and Babich 2011).

The spectral shape of our result is consistent with previous Monte Carlo simulations as seen in Figure 5.9. One can estimate the high-frequency cut-off from some simple arguments. The average kinetic energy, ε_{ave}, gained by a runaway electron that travels a distance z in a constant field is:

$$\varepsilon_{ave} = z(eE - F_D) \tag{5.14}$$

where F_D is the frictional force (Figure 2.1). The change in time of the electron energy is then:

$$\frac{\partial \varepsilon_{ave}}{\partial t} \sim \frac{\partial z}{\partial t}(eE - F_D) \sim v_e(eE - F_D) \tag{5.15}$$

Here, v_e is the electron velocity in the high-energy tail where $v_e \sim c$.

The energy where $f_e(\varepsilon)$ begins to fall off is now estimated by considering a "steady state" condition at high energies such that the production rate of new electrons equals the loss of electrons out of the energy bin (Celestin et al., 2012):

$$\nu_i N_e(\varepsilon) \sim -\frac{\partial N_e}{\partial \varepsilon}\frac{\partial \varepsilon}{\partial t} \tag{5.16}$$

where ν_i is the ionization frequency of runaway electrons production, or:

$$\nu_i N_e(\varepsilon) \sim -c(eE - F_D)\frac{\partial N_e}{\partial \varepsilon} \tag{5.17}$$

or:

$$\frac{\partial N_e}{\partial \varepsilon} \sim \frac{-\nu_i}{c(eE - F_D)} N_e(\varepsilon) \tag{5.18}$$

The solution is:

$$N_r(\varepsilon) \sim N_r^o e^{-\varepsilon/\varepsilon_c} \tag{5.19}$$

$$\varepsilon_c \sim \lambda_r(eE - F_D) \tag{5.20}$$

where we have approximated $\lambda_r \sim c/\nu_i$.

We can estimate the energy cut-off using this formula: The average F_D acting on a runaway avalanche has been estimated to $\sim$ 0.276 MeVm^{-1} at ground pressure (Moss et al., 2006). The electric field corresponding to 0.4 E_k is $\sim$ 1.28 MeVm^{-1}, giving a value of 1 MeVm^{-1} for the net force. At 0.4 E_k, $\lambda_r \sim 8$ m, giving $\varepsilon_c \sim 8$ MeV. This is in good agreement with the value of 7.3 MeV of Dwyer and Babich (2011) (Figure 5.9).

We can get an approximate analytical expression for the cut-off in $f_e(\varepsilon)$ following similar arguments as for the number of electrons (above) (Dwyer et al., 2012):

$$\frac{\partial f_e}{\partial \varepsilon} \sim -\frac{\partial f_e}{\partial z}\frac{\partial z}{\partial \varepsilon} \sim \frac{-1}{\lambda}\frac{1}{eE - F_D} f_e^o \tag{5.21}$$

The normalized energy distribution function can be written using the average kinetic energy and avalanche length formulas as

$$f_e(\varepsilon) \sim \exp(-\frac{\varepsilon}{\varepsilon_c}) \tag{5.22}$$

In Figure 5.10, we reconstructed Figure 5.8 with this analytical exponential function.

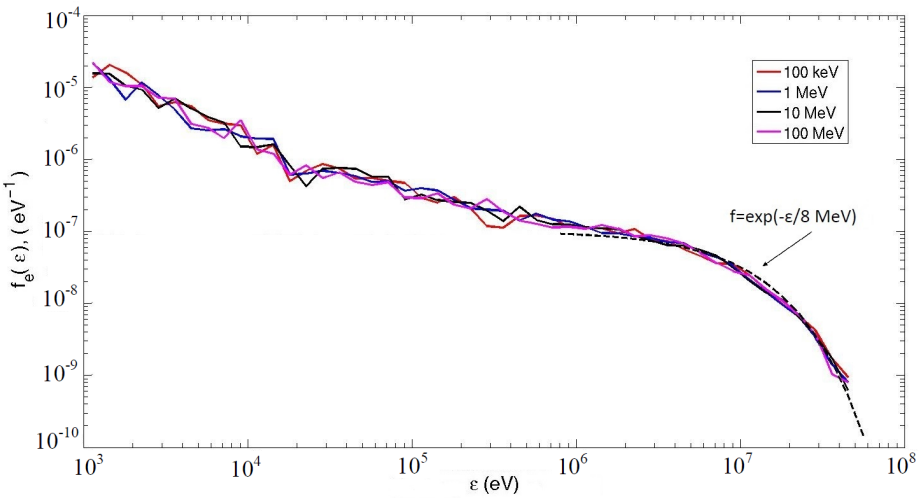

Figure 5.10: $f_e(\varepsilon)$ with the analytical approximation at the high-energy cut-off.

We conclude the the electron spectra are independent on the energy of the seed electrons and that they, overall are in very good agreement with spectra obtained by others.

5.3.3 Bremsstrahlung spectrum for different energies of the seed electron energies

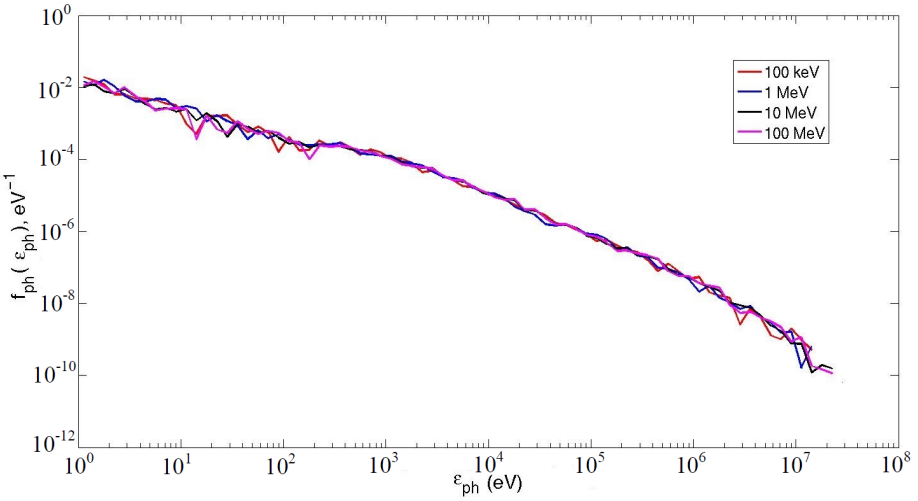

Figure 5.11: $f_{ph}(\varepsilon_{ph})$ for different seed electron energies drifted at the electric field of 0.4 E_k for a time $t = 5.53\tau_r$ (203 ns).

The normalized photon energy distribution, $f_{ph}(\varepsilon_{ph})$, is shown in Figure 5.11 corresponding to the conditions of Figure 5.8. As $f_e(\varepsilon)$ shows no dependency of the seed electron energies, it is no surprise that $f_{ph}(\varepsilon_{ph})$ is also independent, as long as the avalanche has run several τ_r.

The energy dependence agrees with the results of (Celestin and Pasko, 2012). The distribution will be modified when propagation effects are taken into account, as in the case of TGFs observed from satellites. For instance, we show in Figure 5.11 that photons are generated down to 1 eV. The low-energy photons will, of course, be absorbed by the neutral atmosphere. This will be discussed in the next chapter.

5.3.4 Discussion of the bremsstrahlung spectrum

The photon spectrum is approximately a power low; ε_{ph}^k, where k is estimated to -1 (Dwyer,2012) and -1.9 < k < -2.5 (Gjesteland et al., 2011). We can estimate

an improved function by using the same functional dependence for the cut-off as for f_e described earlier: $f_{ph}(\varepsilon_{ph})$ =exp$(-\varepsilon_{ph}/\varepsilon_c)$. The combined analytical approximation:

$$f_{ph}(\varepsilon_{ph}) \sim \varepsilon_{ph}^{-1}\exp(-\varepsilon_{ph}/\varepsilon_c) \tag{5.23}$$

The combined analytical approximation with ε_c = 8MeV and k = -1.2 is shown on Figure 5.12 together with the bremsstrahlung spectra.

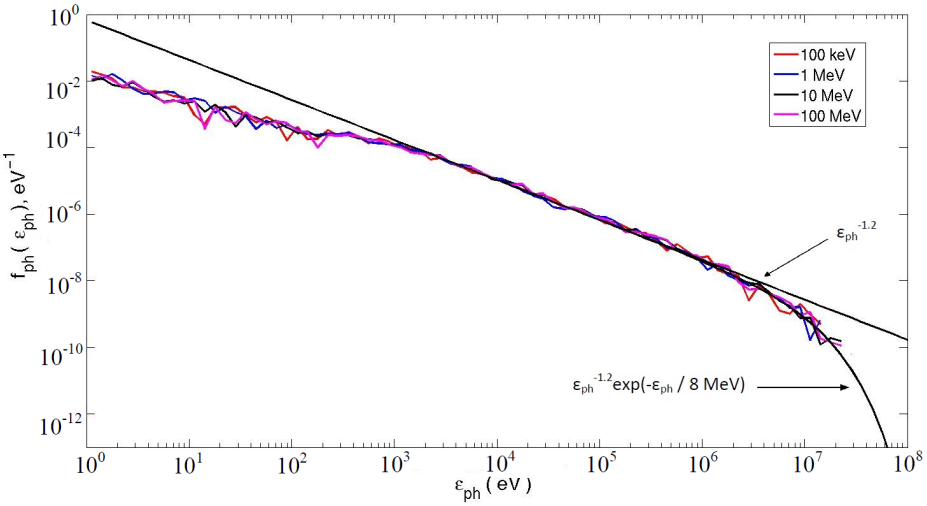

Figure 5.12: $f_{ph}(\varepsilon_{ph})$ for different seed electron energies in an electric field of 0.4 E_k for a time $t = 5.53\tau_r$ (203 ns). Also shown is the analytical approximation with ε_c = 8MeV.

5.3.5 The influence of the number of seed electrons

It has been discussed what really triggers a runaway avalanche. It is clear that seed runaway electrons must be present, but is it important how many there are? We do not expect any dependence of the number of seed electrons on f_e, f_{ph}, as long as the avalanche has run for a sufficient number of τ_r. However, this may not always be the case, and "sufficient number of τ_r" may depend on the number of seed electrons.

We tested the influence of the number of seed electrons in two limits: in one limit we assume a fixed time of 77 ns. This situation is further explored for two cases: a weak field with $E = 0.4\ E_k$ with a fixed time of 77 ns and the other case where the field is strong with $E = 1.5\ E_k$ with a fixed time of 14 ns. In the second limit, the same fields are applied but the avalanches run for a time where 5000 - 6000 photons are emitted. In the latter case, the statistic is the same for all simulations, but the time of the avalanches change.

In both limits we study a number of seed electrons (1 MeV) of 10, 1000, and 10.000. The first case explores the question of what happens if we do not have conditions for a converging spectrum. The other limit explores the question of the converged spectrum - which we think we know from the results discussed in the previous section.

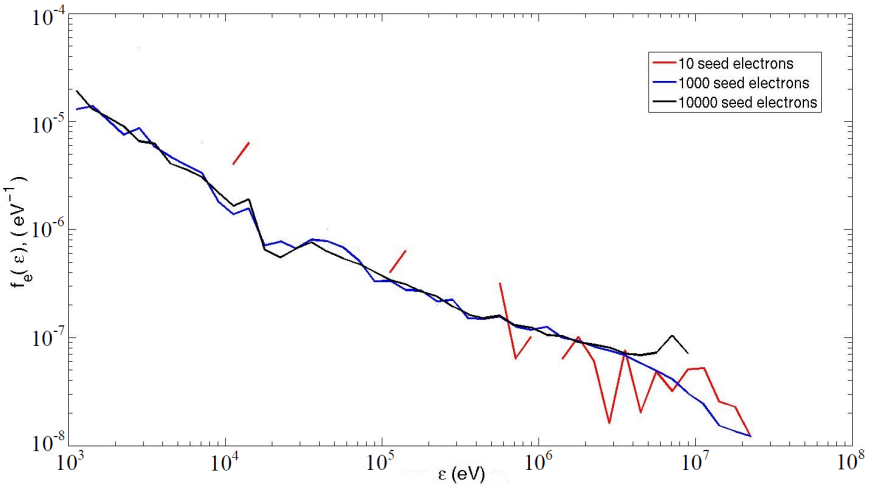

Figure 5.13: $f_e(\varepsilon)$ for different numbers of seed electrons. $E = 0.4\ E_k$ for a run time 77 ns.

The results of the first limit with 77 ns runs are shown in Figures 5.13 - 5.16. We find that the functional forms of the distribution functions are independent of the electric field magnitude and seed electron number, even for an avalanche times of only 2.44 τ_r (the weak field). The main change is the number of avalanche electrons at the end of the avalanche which increases both with electric field magnitude and number of seed electrons, as seen from the statistics of the distribution, e.g. for few avalanche electrons, the (normalized) functions are noisy.

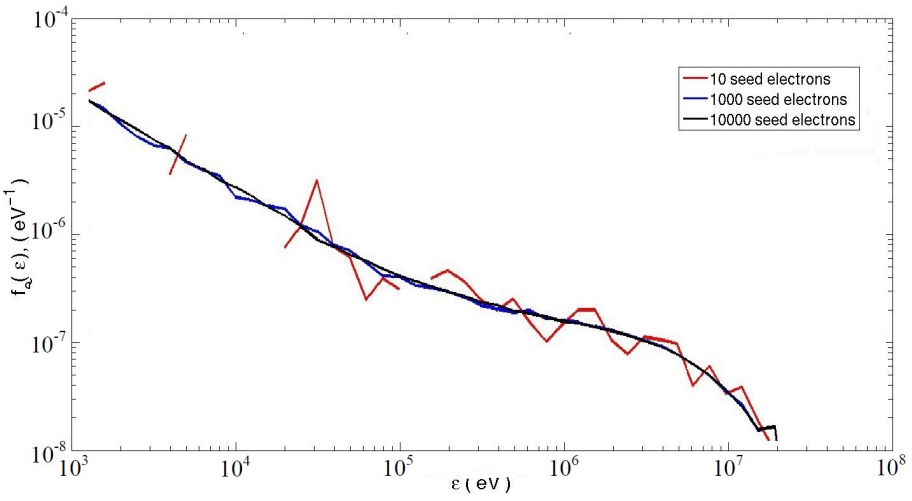

Figure 5.14: $f_e(\varepsilon)$ for different numbers of seed electrons. $E = 1.5\ E_k$ for a run time 14 ns.

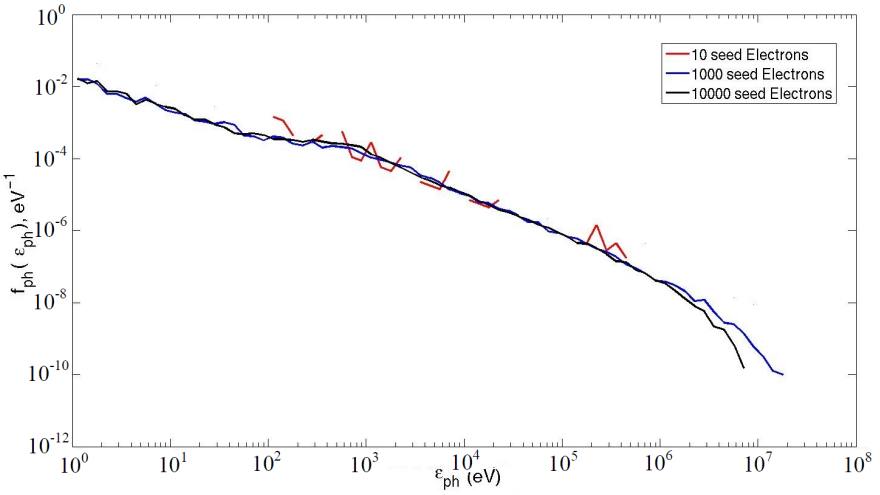

Figure 5.15: $f_{ph}(\varepsilon_{ph})$ for different numbers of seed electrons. $E = 0.4\ E_k$ for a run time 77 ns.

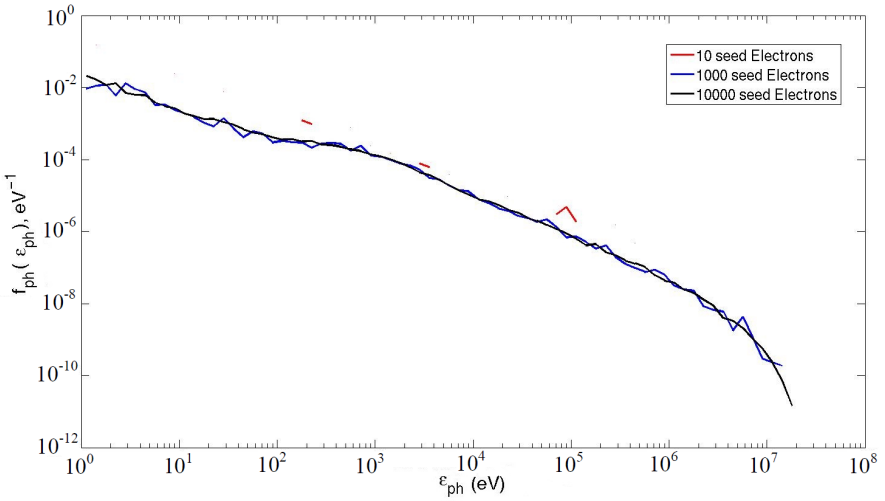

Figure 5.16: $f_{ph}(\varepsilon_{ph})$ for different numbers of seed electrons. $E = 1.5\ E_k$ for a run time 14 ns.

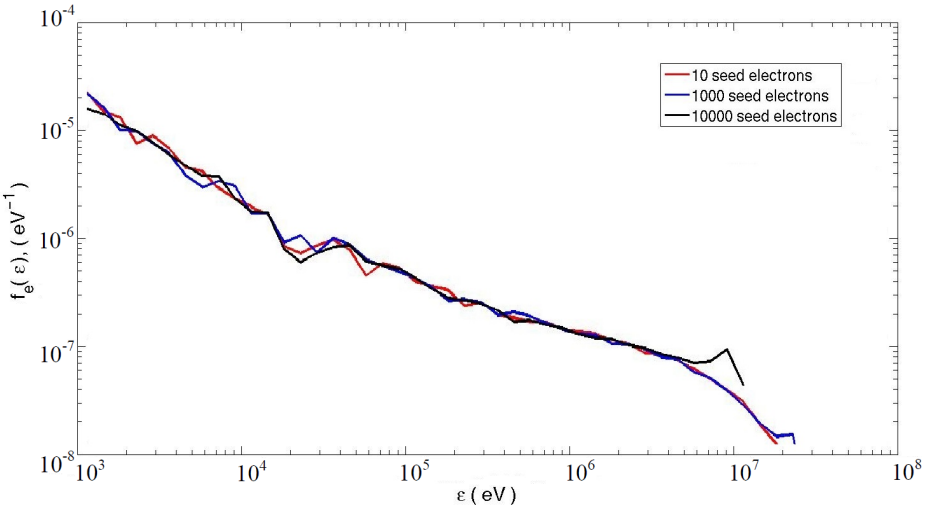

Figure 5.17: $f_e(\varepsilon)$ for different numbers of seed electrons. $E = 0.4\ E_k$ for a run time to emit 5000-6000 photons.

The result for the second limit where runs are continued to a large number of

photons are emitted (5000-6000) are shown in Figures 5.17 - 5.20. We conclude that when the statistics is good, then there are no effects of the number of initial seed electrons on the shape of the normalized electron and photon distributions - as expected.

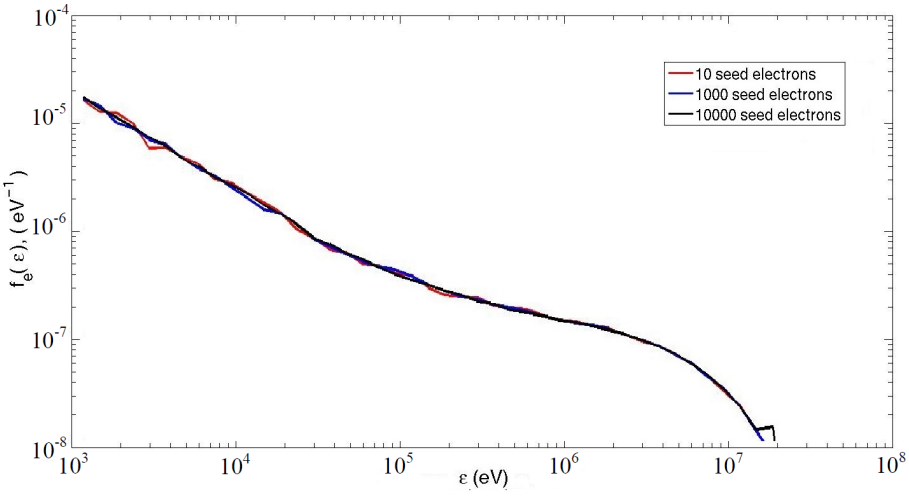

Figure 5.18: $f_e(\varepsilon)$ for different numbers of seed electrons. $E = 1.5\ E_k$ for a run time to emit 5000-6000 photons.

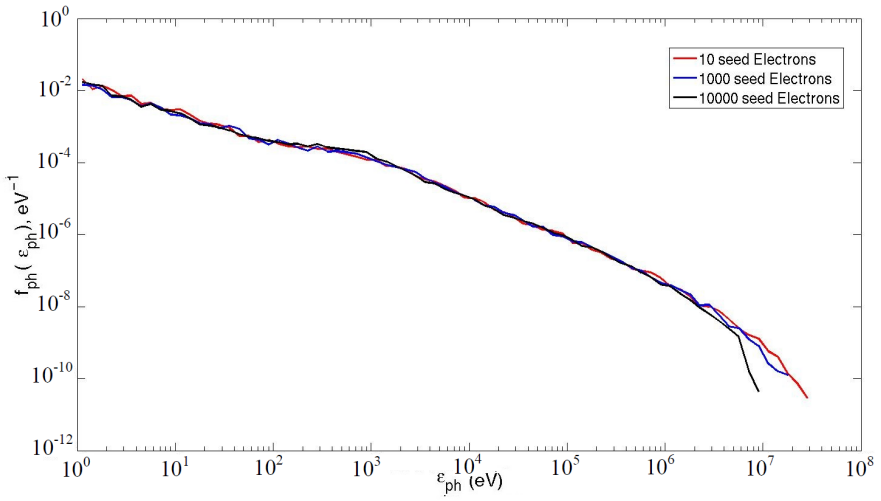

Figure 5.19: $f_{ph}(\varepsilon_{ph})$ for different numbers of seed electrons. $E = 0.4\ E_k$ for a run time to emit 5000-6000 photons.

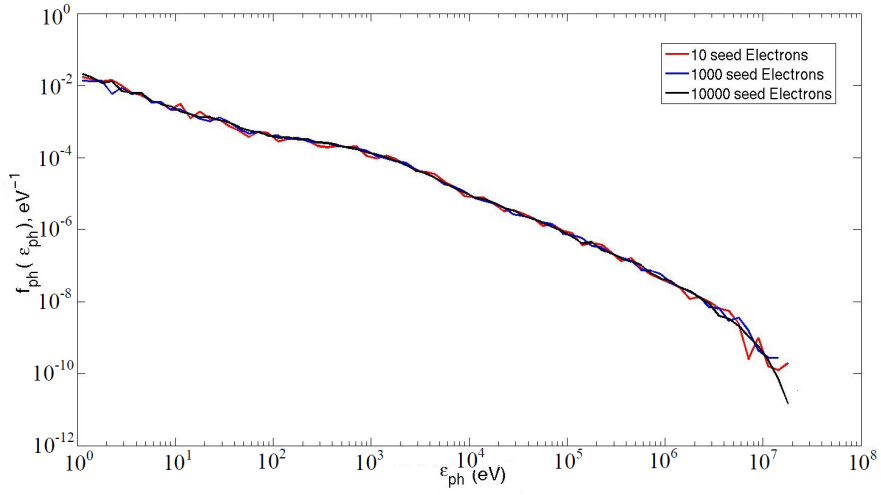

Figure 5.20: $f_{ph}(\varepsilon_{ph})$ for different numbers of seed electrons. $E = 1.5\ E_k$ for a run time to emit 5000-6000 photons.

5.3.6 The influence of the electric field magnitude

The electric field is important for electron acceleration, where electrons gain more energy from stronger fields. It would be interesting if one can, from observations of the photon spectrum, estimate the electric field strength. We therefore investigate the effect of the electric field magnitude on the photon spectrum.

We followed the same approach as for the study of the influence of the number of seed electrons, described in the previous sections, simulating two limits: constant time or high number of photon emissions.

We start with 10 initial seed electrons with energies of 1 MeV, and accelerate them in constant fields between $0.4E_k$ to $10E_k$. The maximum field is a bit above the maximum field expected in streamers and leader tips, which is of the order of 5 E_k (Liu et al. 2006, Celestin and Pasko, 2010) or even up to 10 E_k at lightning stepped leaders (Moss et al., 2006). However, this field is not well characterized. We first study the shape of the electron energy distribution and bremsstrahlung photon spectrum. We run the simulations for a fixed time of 49 ns or for a time that gives approximately the same number of photons emitted (10000-12000). The results are shown in Figures 5.21 to 5.24.

We conclude from these runs that only the high-energy tail is affected, as expected from the approximate formula of a previous section. This implies, that from a satellite perspective, only the highest energy photons carry information on the electric field. However, even this conclusion must be taken with some caution, as the highest energies reflect the integrated effect of the field in the discharge region, i.e., the electric potential drop that an electron has traversed. As we do not simulate electron energies below 1 keV, we omit some runaway electrons in the electric fields 5-10 E_k. We can see effect of these omitted runaway electron in Figure 5.21 as change in electron spectral hardness with the field goes down and up.

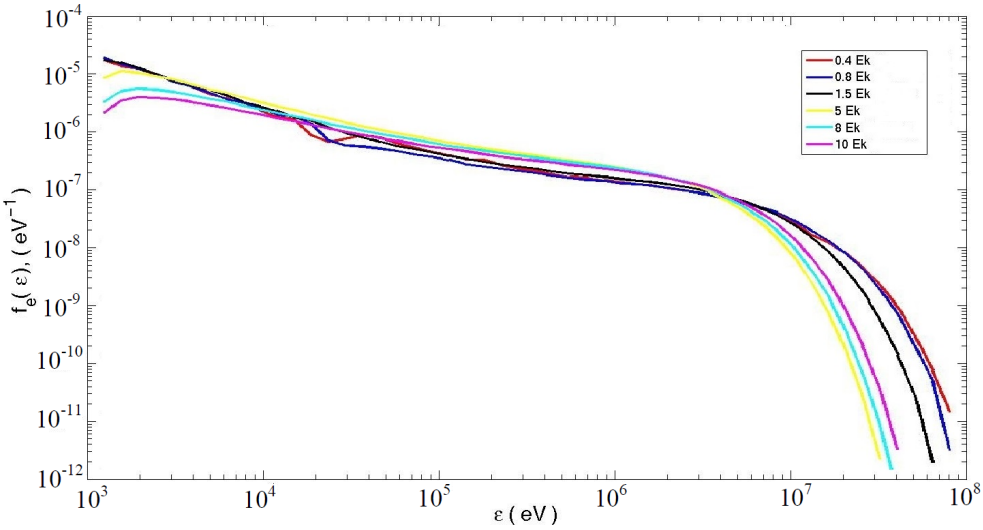

Figure 5.21: $f_e(\varepsilon)$ for different electric fields. 10 seed electrons at 1 MeV are drifted for a time that allows for approx. 10000 photons to be generated.

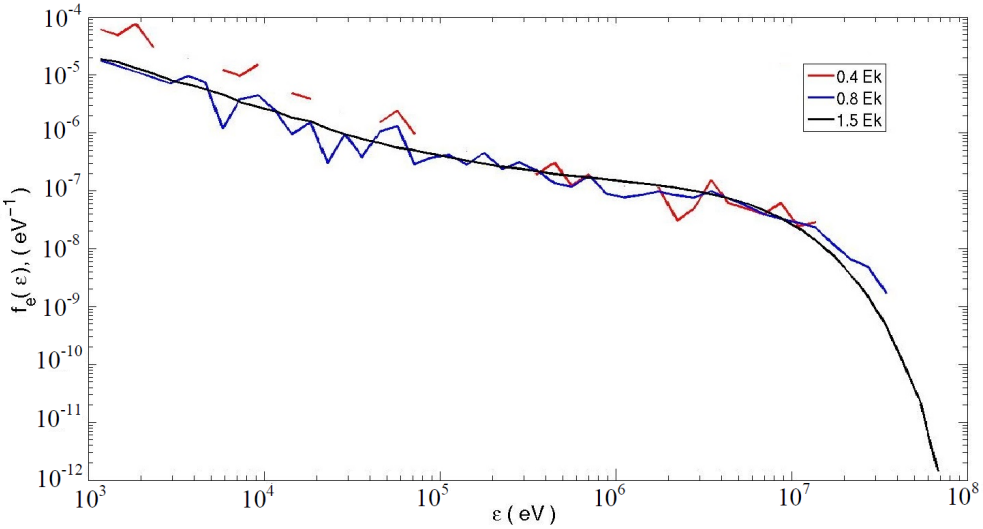

Figure 5.22: $f_e(\varepsilon)$ for different electric fields. 10 seed electrons at 1 MeV are drifted for 49 ns.

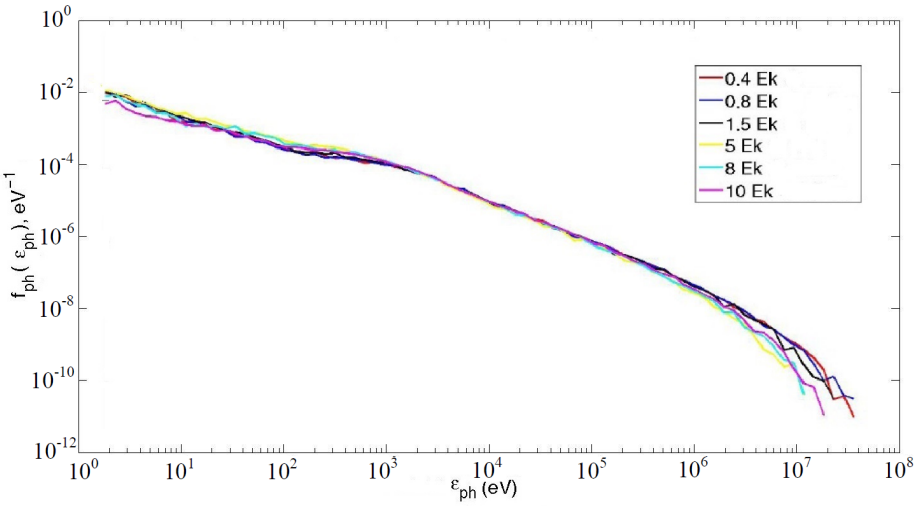

Figure 5.23: $f_{ph}(\varepsilon_{ph})$ for different electric fields. 10 seed electrons at 1 MeV are drifted for a time that allows for approx. 10000 photons to be generated.

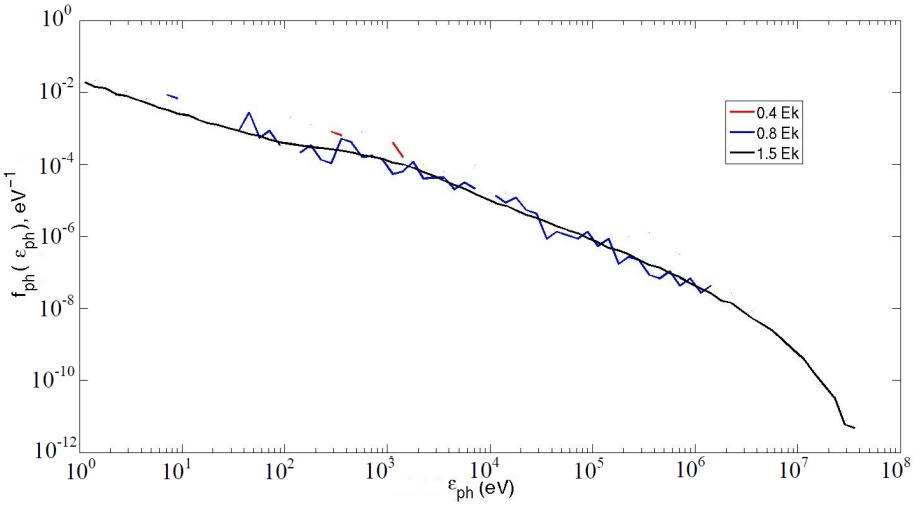

Figure 5.24: $f_{ph}(\varepsilon_{ph})$ for different electric fields. 10 seed electrons at 1 MeV are drifted for 49 ns.

5.4 The bremsstrahlung emission angles

In the previous section we could not see any significant effects of the initial seed electron energy, initial number of seed electrons or background electric field on photon spectrum, except possibly at the highest energies. However, the radiation pattern of bremsstrahlung, discussed earlier, depends on the electron energy and direction of velocity. In the rest frame of the electron, the emissions are approximately omni-directional, while in the reference frame of the atmosphere (or a detector) the radiation is in the forward direction of the electron. The photon radiation pattern then becomes progressively more forward-directed when the electron energy is large and the avalanche becomes beamed, as in the case of high electric fields.

In Figures 5.25 - 5.30 we look at the photon distribution functions in energy and emission angle, θ, relative to the direction of the negative electric field vector. The functions are shown for six electric fields between, E = 0.4 - 10 E_k. On the left is shown the distributions on a rectangular grid and on the right, the same functions in polar coordinates with the photon energy as the radius. The simulations have been run for sufficient time to give good statistics. Each run reached approximately the same number of photons from which the plots are constructed.

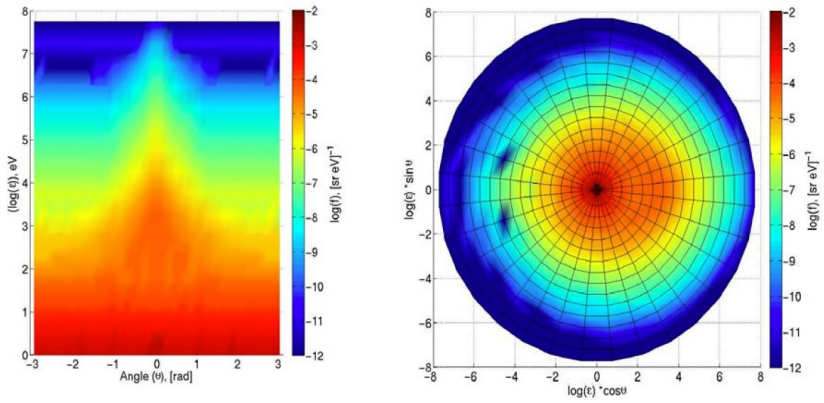

Figure 5.25: $f_{ph}(\varepsilon_{ph}, \theta)$ for $E = 0.4\ E_k$.

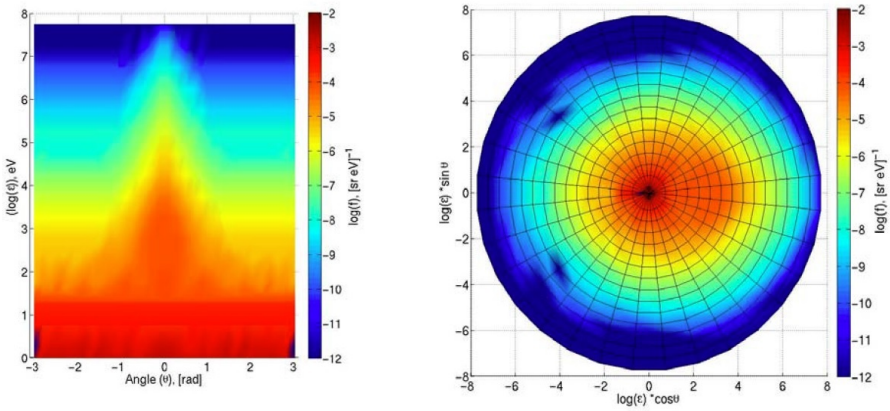

Figure 5.26: $f_{ph}(\varepsilon_{ph}, \theta)$ for $E = 0.8\ E_k$.

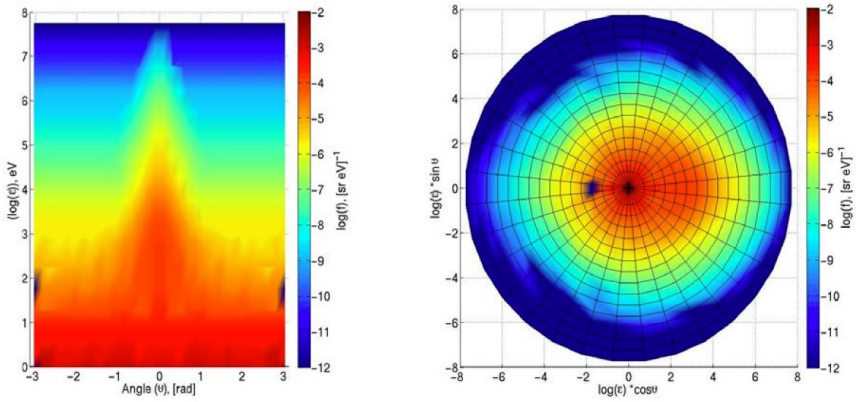

Figure 5.27: $f_{ph}(\varepsilon_{ph}, \theta)$ for $E = 1.5\ E_k$.

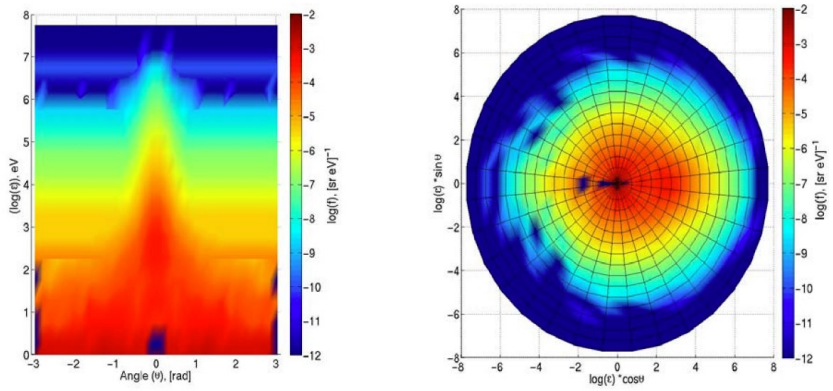

Figure 5.28: $f_{ph}(\varepsilon_{ph}, \theta)$ for $E = 5\ E_k$.

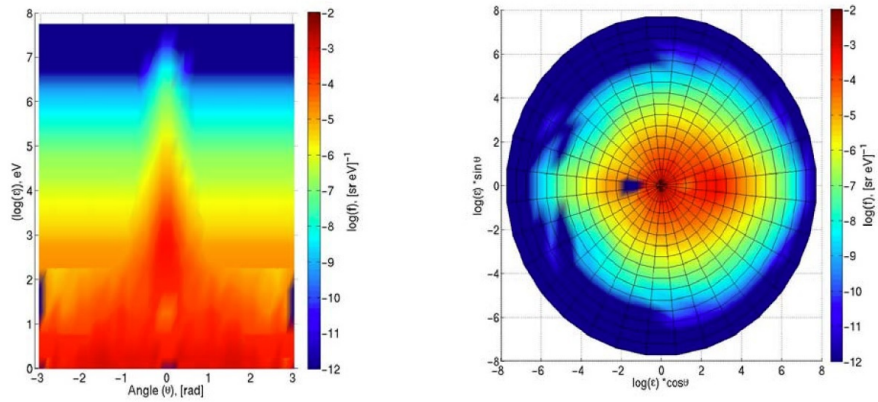

Figure 5.29: $f_{ph}(\varepsilon_{ph}, \theta)$ for $E = 8\ E_k$.

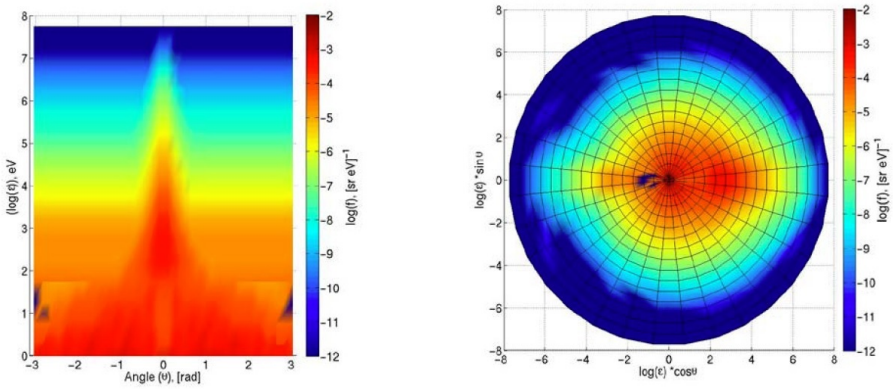

Figure 5.30: $f_{ph}(\varepsilon_{ph}, \theta)$ for $E = 10\ E_k$.

The photon distributions appear to have an omni-directional component and a more energetic, forward-directed component which becomes more beamed as the electric field is increased. At small angles within the beam region, the beamed and the omni-directional distributions combine, with the omni-directional distribution dominating at energies below ≈ 1 keV and the beamed at higher energies. Comparing with the previous figures of the energy distribution function (integrated over emission angle), we see this transition in the spectral shape around 1 keV. X- and Gamma-ray detectors are sensitive to energies above ≈ 1 keV, which suggest that they primarily are sensitive to the beamed component. It means that there are orders of magnitude difference in the photon flux to detectors inside and outside the beam. We further see that the beam width depends on the photon energy. At the lower energies, where the omni-directional flux dominates, the beam is wide, and at the higher energies, where the beamed distribution dominates, the beam narrows.

5.5 Applications to thunderstorms

The photon energy distributions observed by satellite are different from the source distributions because the photons on their path to the satellite detector undergo absorption, or Compton scattering in energy and angle with electrons in the shells of the neutral atmospheric molecules and atoms. As we are not simulating the propagation effects of photons from the source to the satellites, we estimate instead the conditions required at the source to reach a level of $\approx 10^{17}$, proposed as a condition to account for observed TGF intensities if the

source region is at 15 - 21 km (Dwyer and Smith, 2005). In the following we discuss the required avalanche time and length $\tau_{17}(E), \lambda_{17}(E)$, to reach this value, for fields from 0.4 - 10 E_k.

The required avalanche time to reach 10^{17} electrons from a few seed electrons is $\tau_{17} \approx 40\tau_r$. We estimate τ_{17} directly from the data for $\tau_r(E)$ that was derived in a previous section. The avalanche length can be estimated in several ways. We can use the values derived in the previous section (example: 8 m at 0.4 E_k at sea level), the analytical estimate of Dwyer (2003): $\lambda_r = 7.2 \times 10^3 (E - 275)^{-1}$, with λ_r in meters and E in keV, (7 m at 0.4 E_k), or the estimate in Coleman and Dwyer (2006): $\lambda_r = 0.89 c\tau_r$, (10 m at 0.4 E_k). We have adopted the more conservative approach of Coleman and Dwyer that gives the largest interaction length. Like for the avalanche time, 40 λ_r are required, or 400 m at 0.4 E_k with our choice of λ_r. At 0.4 E_k, τ_r = 36.7 ns and τ_{17} =1.47 μs. The functions $\tau_{17}(E), \lambda_{17}(E)$ are shown in figure 5.31.

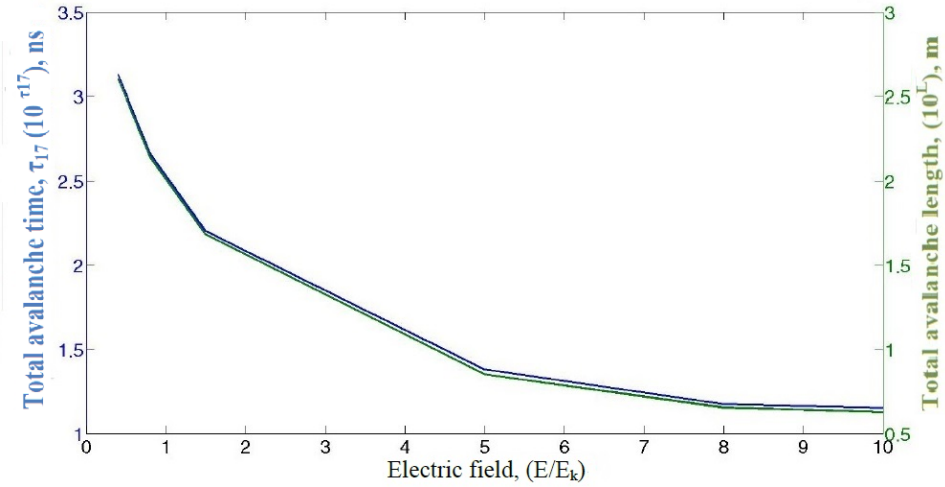

Figure 5.31: $\tau_{17}(E), \lambda_{17}(E)$ at sea level pressure as functions of the electric field.

The potential drop, U, needed to generate the required electrons is $U(E) = E\lambda_{17}$. Figure 5.32 shows U as a function of the electric field at sea level pressures. There is a dramatic decrease in the required potential with electric field magnitude until $\approx 5E_k$. If we consider the conditions in a cloud at 15 km altitude, and assume a scale height of the atmospheric density, n_n, of 7 km, we find that the neutral density is $\sim$ around 10 times smaller and that λ_{17}; τ_{17} therefore are $\sim$ around 10 times larger than shown in Figure 5.32.

The potential drop, on the other hand, remains unchanged since E varies as $\sim 1/n_n$. It means that at 0.4 E_k , $\tau_{17} \sim 14.7\mu$s and $\lambda_{17} \sim 1600$ m, with U $\sim$ 500 MeV. This potential appears to be close to the maximum one can expect in a cloud (Rakov and Uman, 2003), and the avalanche time is relatively long compared to the stepped leader process, where 1 μs is a typical value.

The constraints can be reduced if avalanches begin with a higher number of seed electrons. For instance, if 5 x 10^8 electrons are present initially, the avalanche time and distance are reduced to half. We could also consider $E = 5E_k$ where we, at 15 km altitude, find $\tau_{17} \sim 0.1$ μs and $\lambda_{17} \sim 30$ m, with U $\sim$ 100 MV. These numbers, on the other hand, appear more in line with expectations from the stepped leader process (Rakov and Uman, 2003) and of the modelling results of Carlson et al. (2010).

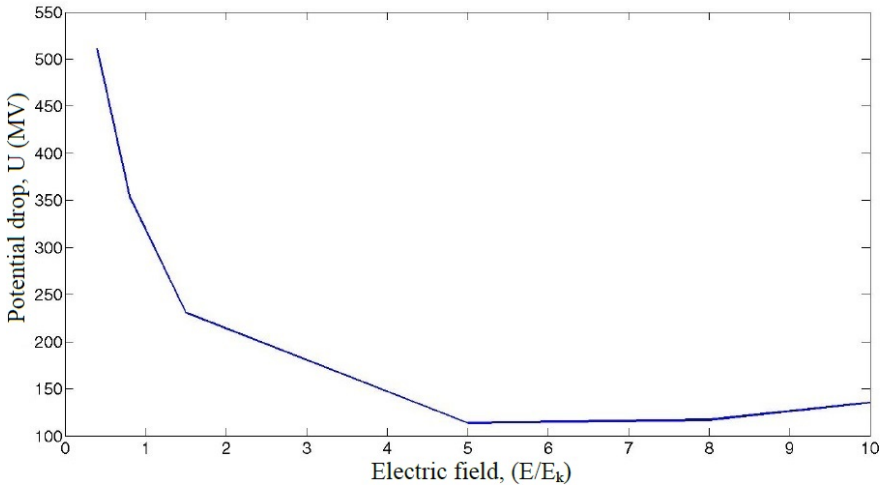

Figure 5.32: The potential U(E) required to generate 10^{17} electrons from 10 seed electrons at sea level pressure.

However, it is a question if a field of this magnitude can be maintained over 30 m for 100 ns. It has been proposed that the maximum time a field of this magnitude can be maintained at a given location is determined by the time it takes the "Maxwell time", $\epsilon_o\sigma$, where σ is the electric conductivity, to grow to the the magnitude of the time constant associated with ionization (Celestin and Pasko, 2011). The reason is that the conductivity is increased by the high number of low-energy electrons created in a discharge (below the 1 keV, which we do not follow in our Monte Carlo code). At cloud levels, the maximum time the electric field at this value can be maintained before it is shorted out is of the

order of a few ns, which is significantly smaller than required for the avalanche to develop.

The solution to this dilemma may be that the high-field region is propagating with a stepped leader tip at velocities approaching close to the speed of light ($0.89c$), either in a single electric potential wave or in a multitude of streamer tip as proposed by Celestin and Pasko (2011) thereby exposing a local volume of the atmosphere for a shorter time than the time of the avalanche.

Chapter 6

Terrestrial gamma-ray flashes at satellite altitudes

6.1 Photon transport through the atmosphere

We next look at how a TGF source photon distribution may look at satellite altitude after the photons have traversed the atmosphere. We have already seen that the source distribution is insensitive to the initial conditions of seed electrons and of the magnitude of the electric field, except for the photon emission angle, which is more beamed for higher electric fields. The question we explore is to what extent the beaming is maintained and observable. A further question discussed by Østgaard et al. (2008) is how the propagation in the atmosphere affect the photon energy spectrum and how one can deduce information on the probable source altitude in the atmosphere from spectra observed from satellites.

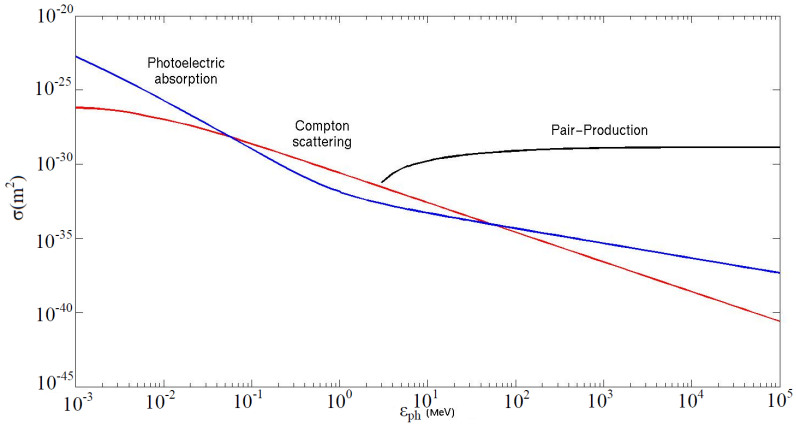

Figure 6.1: Photon propagation cross sections (NIST XCOM photon cross sections database).

The photon propagation model we use has been developed by a team at University of Bergen. It considers three main interactions with air molecules and atoms: Compton scattering, photo-electric absorption and pair production, with cross sections taken from Storm and Israel (1967). We show the cross sections of these interactions in Figure 6.1.

Compton scattering is inelastic scattering of a photon in a charged particle field. In the case of the atmosphere, it is scattering with electrons in the shells of the molecules and atoms. Compton scattering dominates the broad energy range from 30 keV up to a few MeV. In the interaction, photons loose energy and change direction of propagation. In the photon propagation simulation code of the Bergen group, scattering is implemented using the empirical formula of the cross section by Storm and Israel (1967) (Østgaard et al., 2008),

$$\frac{d\sigma_C}{d\theta_C} = \frac{\pi r_o^2 Z \sin\theta_C}{(1+\alpha_n(1-\cos\theta_C))^2}[1+\cos^2\theta_C + \frac{\alpha_n^2(1-\cos\theta_C)^2}{1+\alpha_n(1-\cos\theta_C)}] \qquad (6.1)$$

where r_o is the electron radius, Z is average atomic number for air (7.35), $\alpha_n = \varepsilon_{ph}/511$ keV and θ_C the scattering angle. Once the scattering angle is determined, the photon energy is found from:

$$\varepsilon_{new} = \frac{\varepsilon_{ph}}{1 + \alpha_n(1 - cos\theta_C)} \tag{6.2}$$

The radiation from Compton accelerated electrons are not included in the model (Østgaard et al., 2008).

When the photon energy is above twice the rest mass of an electron, it may interact with the nucleus of atoms and molecules to decay into an electron and its anti-matter equivalent, the positron. The positron and its eventual annihilation is not treated further. The electron is assumed to have an energy according to (Østgaard et al., 2008):

$$\varepsilon_e = \frac{\varepsilon_{ph} - 2 \times 511keV}{2} \tag{6.3}$$

We note that our work does not include the feed-back from positrons although it has been considered important by others, e.g. Dwyer (2003).

We have looked to the effects of the atmosphere of photon propagation from a source altitudes at 13 km to the top of the atmosphere. In the model we consider only photons with energies above 100 keV as photons below are absorbed. The first results are $f_{ph}(\varepsilon_{ph})$ of all photons reaching the top of the atmosphere, i.e. not at a specific point like a satellite location. The spectra are, as shown earlier insensitive to the electric field magnitude. A typical spectrum is shown in Figure 6.2 for $E = 0.4E_k$. The red curve is the normalized source spectrum and the blue curve the normalized spectrum (blue) after reaching the top of the atmosphere.

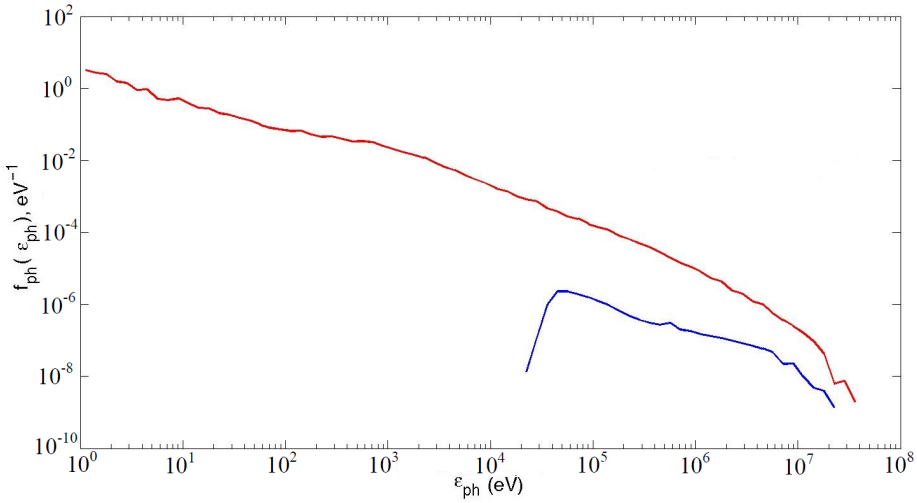

Figure 6.2: Normalized source photon energy distributions for 0.4 E_k from 13 km source region (red) and the distribution after passage of the atmosphere (blue).

6.2 Dependence on altitude

When TGFs were first discovered it was thought that they were associated with sprites (Fishman et al., 1994). Since then, the estimate of the source altitude by various authors continued to decrease with time, as more data became available, e.g., a recent case study shows that IC-lightning generate TGFs (Østgaard et al., 2013).

One could in principle have different types of TGFs and some TLEs could in principle generate X- and Gamma-rays. It is hoped that ASIM will answer this question, carrying instruments for simultaneous observations of TGFs and TLEs. We have therefore studied 3 different source altitudes as 13, 21,and 30 km, by propagating a normalized photon spectrum from the source altitude to the top of the atmosphere. This time, the distributions at the top of the atmosphere are re-normalized. The result is shown in Figure 6.3.

We see that the hardness of the energy spectrum decreases as we go up in the atmosphere, caused primarily by decrease in the attenuation of low energy photons. The spectra have been fitted by a power law $f_{ph} \sim \varepsilon_{ph}^{k}$. At 30 km

altitude, k=-1.2, which is the same as the source spectrum. At 13 km altitude $k = -0.85$.

We note here that a proper simulation must take into account the Earth's magnetic field when studying a source at 30 km altitude. However, this is beyond the scope of the project.

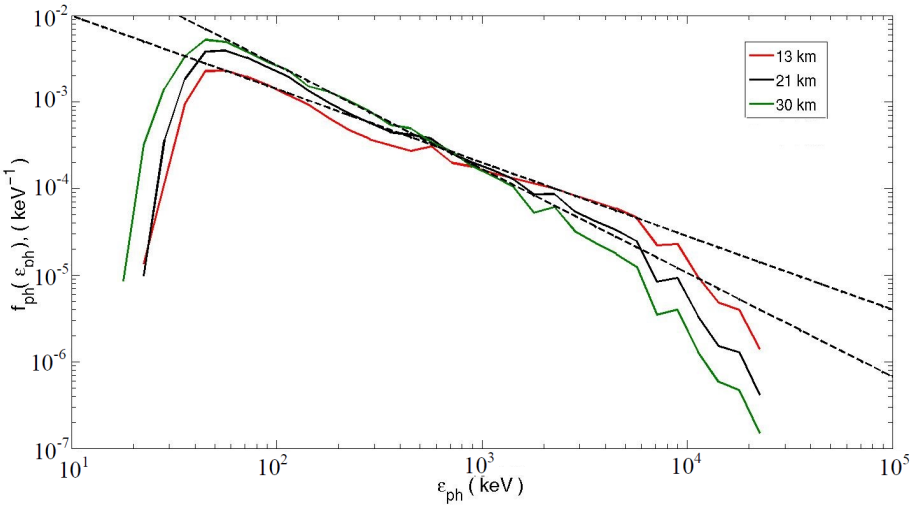

Figure 6.3: $f_{ph}(\varepsilon_{ph})$ at the top of the atmosphere after propagation from a source at 13, 21, and 30 km altitude. The dashed lines are fits to the function at 13 and 30 km altitude.

6.3 The photon emission angle

In the previous chapter we saw the effect of the electric field on the photon angular distribution. Here, we explore the angular distribution after propagation through the atmosphere at satellite altitude. We plot energy and angular distribution functions after passage of the atmosphere from source altitudes at 13 and 30 km (no magnetic field). The results are shown in Figures 6.4 - 6.7 for $E = 0.4$ and 5 E_k.

We see that the effect of the electric field on the photon angular distribution is disappeared because of the interaction with air dominates. In addition, that the distribution for the source at 30 km altitude maintains a more beamed

component around 50-100 keV (left panels). However, at 30 km source altitude, where there is hardly no atmosphere to traverse there is no significant variation of the angular distributions with the magnitude of the electric field. This is contrary to expectation.

However, to properly simulate satellite observations, the total spectral distribution at satellite altitude is not representative. One needs to identify the distribution at a the specific location of a satellite, relative to the source location as studied in Østgaard et al (2008). This is out of scope of the project.

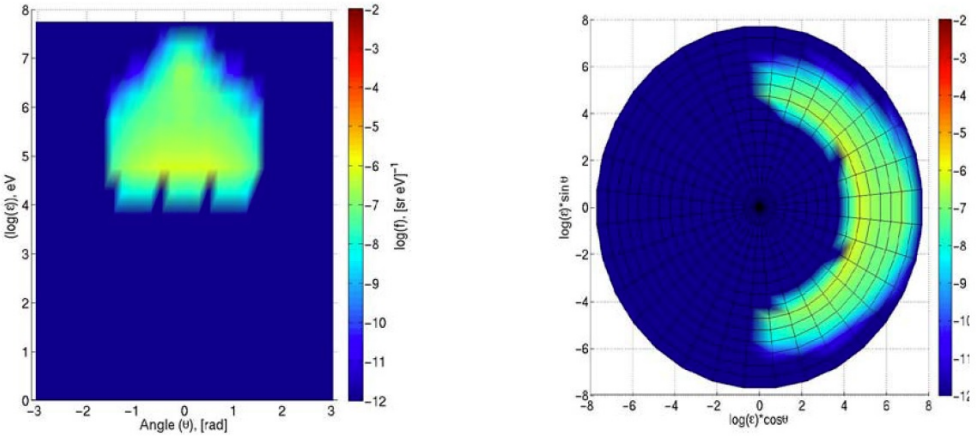

Figure 6.4: Bremsstrahlung photon distributions as functions of energy and emission angle relative to the negative direction of the electric field for 0.4 E_k at 13 km source altitude.

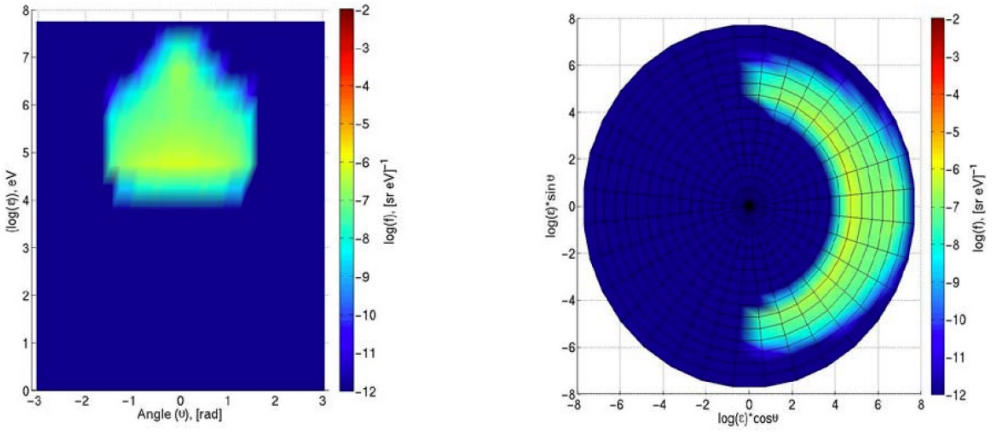

Figure 6.5: Bremsstrahlung photon distributions as functions of energy and emission angle relative to the negative direction of the electric field for 5 E_k at 13 km source altitude.

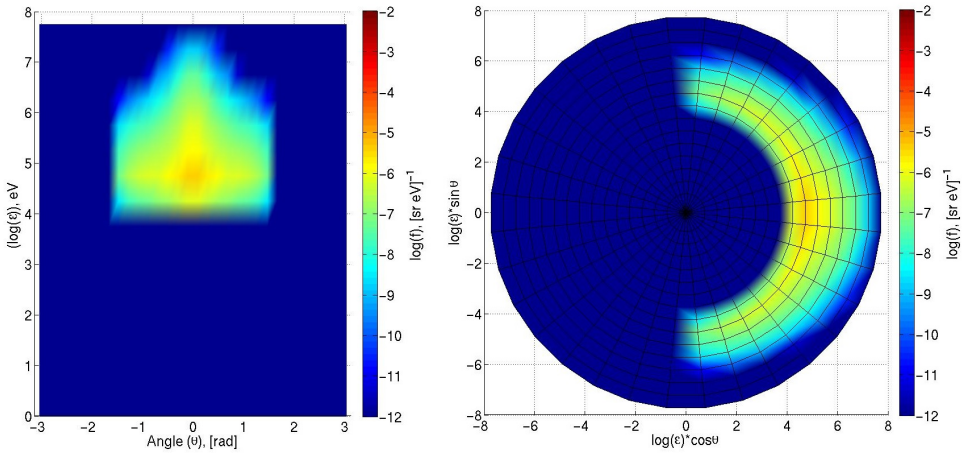

Figure 6.6: Bremsstrahlung photon distributions as functions of energy and emission angle relative to the negative direction of the electric field for 0.4 E_k at 30 km source altitude.

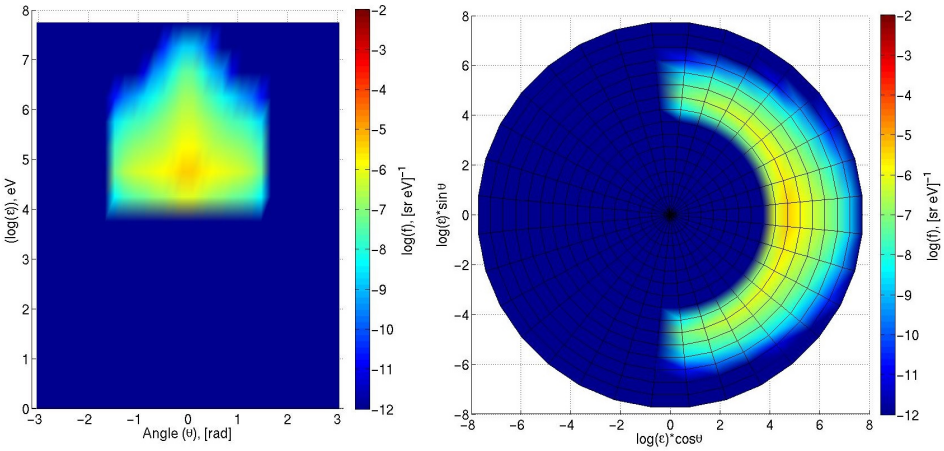

Figure 6.7: Bremsstrahlung photon distributions as functions of energy and emission angle relative to the negative direction of the electric field for 5 E_k at 30 km source altitude.

Chapter 7

Concluding remarks

7.1 Conclusions

We have developed a model to study electron acceleration in an electric field in the atmosphere, including collisional processes such as elastic scattering, ionization and bremsstrahlung emissions. The code is a relativistic extension of the Monte Carlo module of the code by Chanrion and Neubert (2008, 2010). The code has been validated extensively by comparisons with analytical estimates and simulations of others.

We found that the energy spectrum of electrons and photons are insensitive to the initial conditions of seed particles and even the electric field magnitude. The only parameter significantly affected is the photon emission angle of the bremsstrahlung, which is more beamed with high fields.

We applied the model to bremsstrahlung radiation in thunderclouds from electrons accelerated into the runaway regime by electric fields in the clouds. We found that an impulsive electric field of $E \sim 4 - 5E_k$ minimizes the interaction length and avalanche time and brings the electric potential within probable range in a thundercloud. However, it is still open if such magnitude field can be maintained for the required time. The answer to this question awaits a fully self-consistent simulation.

The photon spectrum above the atmosphere was studied assuming the source altitudes located between 13 and 30 km. We found that Compton scattering of photons smooths out the beaming of the photons, washing out any dependence of the electric field. It means that there appears to be no information on the source region field and seeding mechanism. However, we only studied the complete spectrum of all escaping photons and not the photons reaching a specific location relative to the source and the direction of the electric field, such as would be the case of a satellite. It was further found that the hardness of the spectrum decreases with increasing altitude, approaching the source spectrum hardness at high altitudes. This is explained in terms of decrease in the photon attenuation at high altitudes.

7.2 Suggestions for future work

The model does not include the magnetic field. The Earth's magnetic field becomes important at high altitudes, i.e. above 35 km, where the upward direction of electron avalanches changes direction and instead follow magnetic field lines. Studies of sources at high altitudes should then include magnetic field effects. This could be relevant in studies of the effectiveness of TLEs in generating high-energy radiation.

We note that a runaway avalanche creates a large amount of low energy secondary electrons which have not been considered in the present work. These low energy electrons change the conductivity of the avalanche region which will feed back on the distribution of the electric field. It would be interesting for further studies to consider this space charge in combination with an inhomogeneous field.

A final note concerns the feedback mechanism, which we have not evaluated here. It could be important to implement in the code. However, it requires also to include bremsstrahlung photon transport.

We expect future space observations of TGFs, like those expected on TARANIS and ASIM in 2016, where instruments are designed to study TGFs with high time resolution, to be able to give us clues as to altitude of the source region and the temporal and spatial configuration of the TGF.

Bibliography

[1] Acosta, E., Llovet, X., Salvat, F., (2002). Monte Carlo simulation of bremsstrahlung emission by electrons. Appl. Phys. Lett. 80, 3228-3230.

[2] Babich, L. P.,(1995), Teplofiz. Vys. Temp. 33, 659.

[3] Babich, L. P., Donskoy, E. N., Kutsyk, I. M., Kudryavtsev, A. Y., Rousse-Dupre, R. A., Shamraev, B. N., Symbalisty, E. M. (2001). Comparison of relativistic runaway electron avalanche rates obtained from Monte Carlo simulations and kinetic equation solution. Plasma Science, IEEE Transactions on, 29(3), 430-438.

[4] Babich, L. P., Donskoi, E. N., Kutsyk, I. M., Roussel-Dupré, R. A. (2004). Runaway relativistic electron avalanche bremsstrahlung in the atmosphere. GEOMAGNETISM AND AERONOMY C/C OF GEOMAGNETIZM I AERONOMIIA, 44, 645-651.

[5] Banks, P. M., G. Kockarts, Aeronomy, Academic, New York, 1973.

[6] Bazelyan, E.M., Raizer, Yu. P. Spark Discharge, CRC Press, Boca Raton (1998) 294 pp.

[7] Berdeklis, P., List, R. The Ice CrystalGraupel Collision Charging Mechanism of Thunderstorm Electrification. 2001, J. Atmos. Sci. 2751-2770p.

[8] Berestetskii, V. B., E. M. Lifshitz, and L. P. Pitaevskii (1982), Quantum Electrodynamics, Pergamon, Oxford, U. K.

[9] Bethe, H.A., Ann. Phys. 5, 325 (1930).

[10] Bethe, H. and Heitler, W., Proc. Roy. Sot. (London) A 146 (1934) 83.

[11] Betz, H.D. (2004). Lightning detection with 3-D discrimination of intra-cloud and cloud-to-ground discharges. Geophysical Research Letters 31.

[12] Betz, H. D., Schumann, U., Laroche, P. (Eds.). (2009). Lightning: principles, instruments and applications: review of modern lightning research. Springer.

[13] Briggs, M. S., et al. (2010), First results on terrestrial gamma ray flashes from the Fermi Gamma-ray Burst Monitor, J. Geophys. Res., 115, A07323.

[14] Carlson, B. E., Lehtinen, N. G., and Inan, U. S. (2007). Constraints on terrestrial gamma ray flash production from satellite observation. Geophysical Research Letters 34.

[15] Carlson, B. E., N. G. Lehtinen, and U. S. Inan (2009), Terrestrial gamma ray flash production by lightning current pulses, J. Geophys. Res., 114, A00E08.

[16] Carlson, B. E. (2009). Terrestrial Gamma-Ray Flash Production by Lightning. PhD Dissertation. Available at: http://vlf.stanford.edu/pubs/terrestrial-gamma-ray-flash-production-lightning.

[17] Celestin, S., and Pasko, V. P. (2010). Soft collisions in relativistic runaway electron avalanches. Journal of Physics D: Applied Physics 43, 315206.

[18] Celestin, S., and Pasko, V. P. (2011). Energy and fluxes of thermal runaway electrons produced by exponential growth of streamers during the stepping of lightning leaders and in transient luminous events. Journal of Geophysical Research 116.

[19] Celestin, S., Xu, W., and Pasko, V. P. (2012). Terrestrial gamma ray flashes with energies up to 100 MeV produced by nonequilibrium acceleration of electrons in lightning. Journal of Geophysical Research 117.

[20] Chanrion, O., and T. Neubert (2008), A pic-mcc code for simulation of streamer propagation in air, J. Comput. Phys., 227(15), 7222-7245, doi:10.1016/j.jcp.2008.04.016.

[21] Chanrion, O., and T. Neubert (2010), Production of runaway electrons by negative streamer discharges, J. Geophys. Res., 115, A00E32.

[22] Christian, H. J., et al., (2003). Global frequency and distribution of lightning as observed from space by the Optical Transient Detector, J. Geophys. Res., 108(D1), 4005.

[23] Coleman, L. M., and Dwyer, J. R. (2006). Propagation speed of runaway electron avalanches. Geophysical Research Letters 33.

[24] Cooray, V. (Ed.). (2003). The lightning flash (Vol. 34).

[25] Cummer, S. A., Y. Zhai, W. Hu, D. M. Smith, L. I. Lopez, and M. A. Stanley (2005). Measurements and implications of the relationship between lightning and terrestrial gamma ray flashes, Geophysical Research Letters, 32(8).

[26] Dujko, S., Markosyan, A. H., White, R. D., and Ebert, U. (2013). High-order fluid model for streamer discharges: I. Derivation of model and transport data. Journal of Physics D: Applied Physics 46, 475202.

[27] Davies, H., Bethe, H.A., Maximon, L.C., 1954. Theory of bremsstrahlung and pair production. II. Integral cross section for pair production. Phys. Rev. 93, 788-795.

[28] Dwyer, J. R. (2003), A fundamental limit on electric fields in air, Geophys. Res. Lett., 30(20), 2055.

[29] Dwyer, J. R., and D. M. Smith (2005). A comparison between Monte Carlo simulations of runaway breakdown and terrestrial gamma-ray flash observations, Geophys. Res. Lett., L22804.

[30] Dwyer, J. R., et al. (2005). X-ray bursts associated with leader steps in cloud-to-ground lightning, Geophys. Res. Lett., 32.

[31] Dwyer, J. R., B. W. Grefenstette, and D. M. Smith (2008). High-energy electron beams launched into space by thunderstorms, Geophys. Res. Lett., 35, L02815, doi:10.1029/2007GL032430.

[32] Dwyer, J. R., and Babich, L. P. (2011). Low-energy electron production by relativistic runaway electron avalanches in air. Journal of Geophysical Research 116, 1-14.

[33] Dwyer, J. R., Smith, D. M., Cummer, S. A. (2012). High-energy atmospheric physics: terrestrial gamma-ray flashes and related phenomena. Space Science Reviews, 173(1-4), 133-196.

[34] Eack, K., W. Beasley, W. Rust, T. Marshall, and M. Stolzenburg (1996a), Initial results from simultaneous observation of X rays and electric fields in a thunderstorm, J. Geophys. Res., 101(29), 637-640.

[35] Eack, K., W. Beasley, W. Rust, T. Marshall, and M. Stolzenburg (1996b), X-ray pulses observed above a mesoscale convective system, Geophys. Res. Lett., 23(21), 2915-2918.

[36] Eack, K., D. Suszcynsky, W. Beasley, R. Roussel-Dupre, and E. Symbalisty (2000), Gamma-ray emissions observed in a thunderstorm anvil, Geophys. Res. Lett., 27(2), 185-188.

[37] Franz, R. C., Nemzek, R. J. and Winckler, J. R. (1990), Television image of a large upward electric discharge above a thunderstorm system Science 249 48

[38] Fishman, G. J., Bhat, P. N., Mallozzi, R., Horack, J. M., Koshut, T., Kouveliotou, C., Pendleton, G. N., et al. (1994). Discovery of intense gamma-ray flashes of atmospheric origin. Science (New York, N.Y.), 264(5163), 1313-1316

[39] Fukunishi, H., Takahashi, Y., Kubota, M., Sakanoi, K., Inan, U. S., and Lyons, W. A. (1996). Elves: Lightning-induced transient luminous events in the lower ionosphere. Geophysical Research Letters 23, 2157.

[40] Gerken, E. A., Inan, U. S., and Barrington-Leigh, C. P. (2000), Telescopic imaging of sprites. Geophysical Research Letters 27, 2637.

[41] Gjesteland, T., N. Østgaard, P. H. Connell, J. Stadsnes, and G. J. Fishman (2010), Effects of dead time losses on terrestrial gamma ray flash measurements with the Burst and Transient Source Experiment, J. Geophys. Res., 115, A00E21.

[42] Gjesteland, T., Østgaard, N., Collier, A. B., Carlson, B. E., Cohen, M. B., and Lehtinen, N. G. (2011). Confining the angular distribution of terrestrial gamma ray flash emission. Journal of Geophysical Research 116.

[43] Gjesteland, T., Østgaard, N., Collier, A. B., Carlson, B. E., Eyles, C., and Smith, D. M. (2012). A new method reveals more TGFs in the RHESSI data. Geophysical Research Letters 39.

[44] Gurevich, A. V., G. M. Milikh, and R. A. Roussel-Dupre (1992), Runaway electron mechanism of air breakdown and preconditioning during a thunderstorm, Phys. Lett. A., 165(5 - 6), 463 - 468.

[45] Gurevich, A. V., and K. P. Zybin (2001), Runaway breakdown and electric discharges in thunderstorms, Physics-Uspekhi, 44(11), 1119-1140.

[46] Gurevich, A. V., L. M. Duncan, A. N. Karashtin, and K. P. Zybin (2003), Radio emission of lightning initiation, Phys. Lett. A, 312, 228-237.

[47] Gurevich, A. V., Y. V. Medvedev, and K. P. Zybin (2004), New type discharge generated in thunderclouds by joint action of runaway breakdown and extensive atmospheric shower, Phys. Lett. A, 329, 348-361.

[48] Gurevich, A. V., Mitko, G. G., Antonova, V. P., Chubenko, A. P., Karashtin, A. N., Kryukov, S. V., Naumov, A. S., Pavljuchenko, L. V., Ptitsyn, M. O., Ryabov, V. A., et al. (2009). An intracloud discharge caused by extensive atmospheric shower. Physics Letters A 373, 3550-3553.

[49] Gurevich, A. V., and Karashtin, A. N. (2013). Runaway Breakdown and Hydrometeors in Lightning Initiation. Physical Review Letters 110, 185005.

[50] Hagelaar, G. J. M., and Pitchford, L. C. (2005). Solving the Boltzmann equation to obtain electron transport coefficients and rate coefficients for fluid models. Plasma Sources Science and Technology 14, 722-733.

[51] Haldoupis, C., Neubert, T., Inan, U. S., Mika, A., Allin, T. H., Marshall, R. A. (2004). Subionospheric early VLF signal perturbations observed in one-to-one association with sprites. Journal of Geophysical Research, 109(A10), A10303.

[52] Haug, E., (1975). Bremsstrahlung and pair production in the field of free electrons. Z. Naturforsch. 30a, 1099-1113.

[53] Heitler, W., 1954. The Quantum Theory of Radiation. Oxford University Press, London.

[54] Inan, U. S., Reising, S. C., Fishman, G. J., and Horack, J. M. (1996). On the association of terrestrial gamma-ray bursts with lightning and implications for sprites. Geophysical Research Letters 23, 1017.

[55] Jackson, J.D., 1975. Classical Electrodynamics. Wiley, New York.

[56] Jungwirth, P., Rosenfeld, D., and Buch, V. (2005). A possible new molecular mechanism of thundercloud electrification. Atmospheric Research 76, 190-205.

[57] Kim, Y.-K., and Rudd, M. (1994). Binary-encounter-dipole model for electron-impact ionization. Physical Review A 50, 3954-3967.

[58] Kim, Y.-K., Santos, J., and Parente, F. (2000). Extension of the binary-encounter-dipole model to relativistic incident electrons. Physical Review A 62.

[59] Kirkpatrick, P., Wiedmann, L., (1945). Theoretical continuous X-ray energy and polarization. Phys. Rev. 67, 321-339.

[60] Kissel, L., Quarles, C.A., Pratt, R.H., (1983). Shape functions for atomic-field bremsstrahlung from electrons of kinetic energy 1-500 keV on selected neutral atoms 1pZp92. At. Data Nucl. Data Tables 28, 381-460.

[61] Koch, H.W., Motz, J.W., (1959). Bremsstrahlung cross-section formulas and related data. Rev. Mod. Phys. 31, 920-955.

[62] Lang, T. J., and Rutledge, S. A. (2002). Relationships between Convective Storm Kinematics, Precipitation, and Lightning. Monthly Weather Review 130, 2492-2506.

[63] Lehtinen, N. G., Bell, T. F., and Inan, U. S. (1999). Monte Carlo simulation of runaway MeV electron breakdown with application to red sprites and terrestrial gamma ray flashes. Journal of Geophysical Research 104, 24699.

[64] Lin, S. L., and Bardsley, J. N. (1977). J. Chem. Phys. 66, 435.

[65] Longmire, C. L. and Longley, H. J., (1973). Improvements in the Treatment of Compton Current and Air Conductivity in EMP Problems.

[66] MacGorman, D. R., and Rust, W. D. (1998), The Electrical Nature of Storms. Oxford University Press, New York, USA.

[67] Marisaldi, M., Fuschino, F., Labanti, C., Galli, M., Longo, F., Del Monte, E., Barbiellini, G., Tavani, M., Giuliani, A., Moretti, E., et al. (2010). Detection of terrestrial gamma ray flashes up to 40 MeV by the AGILE satellite. Journal of Geophysical Research 115.

[68] Marshall, T. C. (2005). Observed electric fields associated with lightning initiation. Geophysical Research Letters 32.

[69] McCarthy, M., and Parks, G. (1985), Further observations of X-rays inside thunderstorms, Geophys. Res. Lett., 12, 393-396.

[70] McHarg, M. G., Stenbaek-Nielsen, H. C., and Kammae, T. (2007). Observations of streamer formation in sprites. Geophysical Research Letters 34.

[71] McIntosh, A. I. (1974). Aust. J. Phys. 27, 59.

[72] Moore, C., Eack, K., Aulich, G. and Rison, W. (2001), Energetic radiation associated with lightning stepped-leaders, Geophys. Res. Lett., 28(11), 2141-2144.

[73] Moss, G., V. P. Pasko, N. Liu, and G. Veronis (2006), Monte Carlo model for analysis of thermal runaway electrons in streamer tips in transient luminous events and streamer zones of lightning leaders, J. Geophys. Res., 111, A02307.

[74] Murphy, T. (1988), Total and differential electron collision cross sections for O2 and N2, Rep. LA-11288-MS, Los Alamos Natl. Lab., Los Alamos, N. M.

[75] Nanbu, K. (1994). Simple Method to Determine Collisional Event in Monte Carlo Simulation of Electron-Molecule Collision. Japanese Journal of Applied Physics 33, 4752-4753.

[76] Nemiroff, R. J., J. T. Bonnell, and J. P. Norris (1997), Temporal and spectral characteristics of terrestrial gamma flashes, J. Geophys. Res., 102, 9659-9666.

[77] Neubert, T., Chanrion, O. (2013). On the electric breakdown field of the mesosphere and the influence of electron detachment. Geophysical Research Letters.

[78] Nguyen, C. V., Deursen, A. P. J. van, Heesch, E. J. M. van, Winands, G. J. J., and Pemen, A. J. M. (2009). X-ray emission in streamer-corona plasma. Journal of Physics D: Applied Physics 43, 025202.

[79] Okhrimovskyy, A., Bogaerts, A., and Gijbels, R. (2002), Electron anisotropic scattering in gases: a formula for Monte Carlo simulations. Physical review. E, Statistical, nonlinear, and soft matter physics 65, 037402.

[80] Opal, C. B., W. K. Peterson, and E. C. Beaty (1971), Measurements of secondary-electron spectra produced by electron impact ionization of a number of simple gases, J. Chem. Phys., 55(8), 4100- 4106.

[81] Parks, G. K., Mauk, B. H., Spiger, R., and Chin, J. (1981). X-ray enhancements detected during thunderstorm and lightning activities. Geophysical Research Letters 8, 1176.

[82] Pasko, V. P., M. A. Stanley, J. D. Mathews, U. S. Inan, and T. G. Wood, Electrical discharge from a thundercloud top to the lower ionosphere, Nature, vol. 416, pp. 152-154, 2002

[83] Phelps, A. V. 1985. JILA Information Center Report No. 28, University of Colorado.

[84] Phelps, A.V., Pitchford, L.C. (1985), Anisotropic scattering of electrons by n2 and its effect on electron transport, Phys. Rev. A 31 (5) 2932-2949.

[85] Pratt, R.H., Tseng, H.K., Lee, C.M., Kissel, L., MacCallum, C., Riley, M., 1977. Bremsstrahlung energy spectra from electrons of kinetic energy 1 keV pT1p2000 keV incident on neutral atoms 2pZp92. At. Data Nucl. Data Tables 20, 175-209 Erratum: At. Data Nucl. Data Tables 26 (1981) 477-481.

[86] Raizer, Y. P. (1991), Gas Discharge Physics, Springer, New York.

[87] Rakov, V. V. A., Uman, M. A. (2003). Lightning: physics and effects. Cambridge University Press.

[88] Ramos, D.; Patrick, E.; Abner, D.; Andrews, M., Garscadden, A. Gallagher, J.; Hudson, D.; Kunhardt, E., Brunt, R. (1990), A Monte Carlo Simulation Of Electron Drift Limited By Collisions In Gas Mixtures Using The Null Collision Method Nonequilibrium Effects in Ion and Electron Transport, Springer US, 337-338.

[89] Rees, M. H., (1964) Ionization in the Earth's atmosphere by aurorally associated Bremsstrahlung X-rays, Planetary and Space Science 12, 11, 1093-1108.

[90] Reid, I. D. (1979). An investigation of the accuracy of numerical solutions of Boltzmann's equation for electron swarms in gases with large inelastic cross sections. Australian Journal of Physics, 32(3), 231-254.

[91] Roussel-Dupré, R., Gurevich, A., Tunnell, T., and Milikh, G. (1994). Kinetic theory of runaway air breakdown. Physical Review E 49, 2257-2271.

[92] Roussel-Dupré, R., Colman, J. J., Symbalisty, E., Sentman, D., and Pasko, V. P. (2008). Physical Processes Related to Discharges in Planetary Atmospheres. Space Science Reviews 137, 51-82.

[93] Salvat, F., Fernández-Varea, J. M., Sempau, J., and Llovet, X. (2006). Monte Carlo simulation of bremsstrahlung emission by electrons. Radiation Physics and Chemistry 75, 1201-1219.

[94] Saunders, C. P. R., W. D. Keith, and R. P. Mitzeva, (1991), The effect of liquid water on thunderstorm charging, J. Geophys. Res., 96, 11007-11017.

[95] Saunders, C. P. R. and Brooks, I. M., (1992), The Effects of High Liquid Water Content on Thunderstorm Charging, Journal of Geophysical Research 97, NO. D13, p. 14,671-14,676.

[96] Seltzer, S.M., Berger, M.J., 1985. Bremsstrahlung spectra from electron interactions with screened atomic nuclei and orbital electrons. Nucl. Instrum. Meth. B 12, 95-134.

[97] Seltzer, S.M., Berger, M.J., 1986. Bremsstrahlung energy spectra from electrons with kinetic energy 1 keV-10GeV incident on screened nuclei and orbital electrons of neutral atoms with Z $\frac{1}{4}$ 1-100. At. Data Nucl. Data Tables 35, 345-418.

[98] Sentman, D. D., E. M. Wescott, D. L. Osborne, D. L. Hampton, and M. J. Heavner (1995), Preliminary results from Sprites94 campaign: Red sprites, Geophys. Res. Lett., 22(10), 1205-1208.

[99] SkuIlerud, H. R. (1968). J. Phys. D 1, 1567.

[100] Smith, D. M., Lopez, L. I., Lin, R. P., and Barrington-Leigh, C. P. (2005). Terrestrial gamma-ray flashes observed up to 20 MeV. Science (New York, N.Y.) 307, 1085-1088.

[101] Sommerfeld, A., 1931. Diffraction and scattering of electrons. Ann. Physik 11, 257-330.

[102] Soula, S., (2012), Electrical Environment in a Storm Cloud. Aerospace Lab Issue 5.

[103] Stolzenburg, M., Rust, W. D., and Marshall, T. C. (1998a). Electrical structure in thunderstorm convective regions: 1. Mesoscale convective systems. Journal of Geophysical Research 103, 14059.

[104] Stolzenburg, M., Rust, W. D., and Marshall, T. C. (1998b). Electrical structure in thunderstorm convective regions: 2. Isolated storms. Journal of Geophysical Research 103, 14079.

[105] Stolzenburg, M., Marshall, T. C., Rust, W. D., Bruning, E., MacGorman, D. R., and Hamlin, T. (2007). Electric field values observed near lightning flash initiations. Geophysical Research Letters 34.

[106] Stolzenburg, M., Marshall, T. C. (2009). Electric field and charge structure in lightning-producing clouds. In Lightning: Principles, Instruments and Applications (pp. 57-82). Springer Netherlands.

[107] Storm, E., Israel, H. I. (1967). Photon cross section from 0.001 to 100 MeV for elements 1 through 100. Los Alamos Scientific Laboratory, New Mexico.

[108] Su, H. T., R. R. Hsu, A. B. Chen, Y. C. Wang, W. S. Hsiao, W. C. Lai, L. C. Lee, M. Sato, and H. Fukunishi (2003), Gigantic jets between a thundercloud and the ionosphere, Nature, 423(6943), 974-976.

[109] Takahashi, T., (1978), Riming electrification as a charge generation mechanism in thunderstorms, J. Atmos. Sci., 35, 1536-1548.

[110] Tavani, M., Marisaldi, M., Labanti, C., Fuschino, F., Argan, A., Trois, A., Giommi, P., Colafrancesco, S., Pittori, C., Palma, F., et al. (2011). Terrestrial gamma-ray flashes as powerful particle accelerators. Physical review letters 106, 018501.

[111] Tseng, H.K., Pratt, R.H., 1971. Exact screened calculations of atomic-field bremsstrahlung. Phys. Rev. A 3, 100-115.

[112] Uman, M. A. (2001), The Lightning Discharge, Dover, Mineola, N. Y.

[113] Wescott, E. M., D. D. Sentman, D. L. Osborne, D. L. Hampton, and M. J. Heavner, Preliminary results from the sprites 94 aircraft campaign: 2. Blue jets, Geophys. Res. Lett., vol. 22, pp. 1209-1213, 1995.

[114] Wilson, C. T. R. (1925). The Acceleration of β particles in Strong Electric Fields such as those of Thunderclouds. Mathematical Proceedings of the Cambridge Philosophical Society 22, 534.

[115] Østgaard, N., T. Gjesteland, J. Stadsnes, P. Connell, and B. Carlson (2008), Production altitude and time delays of the terrestrial gamma flashes: Revisiting the burst and transient source experiment spectra., J. Geophys. Res., 113, A02307.

[116] Østgaard, N., Gjesteland, T., Carlson, B. E., Collier, A. B., Cummer, S. A., Lu, G., and Christian, H. J. (2013). Simultaneous observations of optical lightning and terrestrial gamma ray flash from space. Geophysical Research Letters 40, 2423-2426.

Appendix

7.3 Characterization of Terrestrial Gamma-ray Flashes at Their Source

The submitted paper has been enclosed.

DTU Space – National Space Institute
Technical University of Denmark

Elektrovej Buildings 327 + 328
DK - 2800 Kgs. Lyngby
Tlf: +45 4525 9500
Fax: +45 4525 9575

www.space.dtu.dk